

12-15-2014

# On the Development of High Strain Rate Experiments for the Characterization of Engineering Materials

Silas P. Mallon

*University of South Carolina - Columbia*

Follow this and additional works at: <http://scholarcommons.sc.edu/etd>

---

## Recommended Citation

Mallon, S. P.(2014). *On the Development of High Strain Rate Experiments for the Characterization of Engineering Materials*. (Master's thesis). Retrieved from <http://scholarcommons.sc.edu/etd/2935>

This Open Access Thesis is brought to you for free and open access by Scholar Commons. It has been accepted for inclusion in Theses and Dissertations by an authorized administrator of Scholar Commons. For more information, please contact [SCHOLARC@mailbox.sc.edu](mailto:SCHOLARC@mailbox.sc.edu).

ON THE DEVELOPMENT OF HIGH STRAIN RATE EXPERIMENTS FOR THE  
CHARACTERIZATION OF ENGINEERING MATERIALS

by

Silas P. Mallon

Bachelor of Science  
University of South Carolina, 2012

---

Submitted in Partial Fulfillment of the Requirements

For the Degree of Master of Science in

Mechanical Engineering

College of Engineering and Computing

University of South Carolina

2014

Accepted by:

Addis Kidane, Director of Thesis

Michael Sutton, Reader

Lacy Ford, Vice Provost and Dean of Graduate Studies

© Copyright by Silas P. Mallon, 2014  
All Rights Reserved.

## ACKNOWLEDGEMENTS

I would like to acknowledge Dr. Addis Kidane for his continued support throughout the duration of graduate career. As a result of his encouragement and advice, I have become a more competent and patient engineer.

Dr. Michael Sutton is acknowledged here for his many contributions during the course of my graduate studies and research. His consistently positive mindset, vast knowledge of science and engineering, and rational approach to solving problems have contributed to my character as an engineer and as a person. I gratefully acknowledge Dr. David Rocheleau the encouragement and inspiration he has provided as an exceptional engineer and individual. I would like to especially acknowledge Behrad Koohbor, an individual I hold in the highest esteem whose knowledge and intellect have proven invaluable throughout the course of my studies and research.

Finally, this page would be incomplete without the mention of Mr. William Bradley and Mr. Dan Wilhelm for the tremendous amount of knowledge they have instilled in me regarding machining and fabrication.

## ABSTRACT

In order to predict the damage accumulation and failure processes associated with highly dynamic events such as blast loading, shock wave loading, and ballistic impact loading, a commensurate understanding of the fundamental constitutive and fracture behavior of materials subjected to such high rate loading conditions is necessary. In this effort, high strain rate experimental facilities consisting of a shock tube apparatus and a torsional split Hopkinson bar apparatus have been designed, constructed, and subsequently used to investigate the mechanical properties of an array of engineering materials subjected to a variety of dynamic loading conditions.

Designs for the experimental equipment utilized are based mostly on modified versions of established equipment already in use elsewhere; however improvements have been implemented wherever possible with an emphasis on reliability, robust design, and versatility. Fabrication of all equipment was performed by the author.

Three experimental works conducted using these experimental apparatuses are presented, each considering a unique engineering material and dynamic stress state. 1) Pre-stressed orthogonally woven composites were subjected to shock loading, and the effect of loading rate and fiber orientation on both fracture toughness and crack growth direction is presented. 2) Rigid closed cell foams were subjected to compressive shock loading and the effect of foam density and strain rate on the compressive properties of the foam is presented. 3) Finally, a high strength aluminum alloy is subjected to high strain rate torsional loading, in as-received and friction stir welded states, and the effects of

microstructure and strain rate on the shear properties of the alloy are presented. The wide variety of materials tested and the diverse array of dynamic stress states achieved serve to illustrate the versatility and effectiveness of the experimental equipment constructed and utilized in this work.

## PREFACE

The present work addresses the establishment and use of experimental equipment for the use of characterizing the behavior of engineering materials at elevated, or dynamic, strain rates. The selection of experimental research presented herein encompasses a broad range of material types and stress states, demonstrating conclusively both the utility and versatility of the apparatuses that have been employed in these studies.

Chapter 1 provides a condensed background pertaining to the importance of dynamic strain rates. The evolution and development of the two experimental apparatuses used in this work, the shock tube and the torsional split Hopkinson bar, are also discussed in a concise manner.

Chapter 2 presents the design and fabrication of the experimental equipment and associated fixtures. Basic design criteria followed are observed from the literature and analytical formulations. Useful details regarding fabrication of the equipment are also presented. Modifications deviating from the established literature, resulting from the pursuit of convenience and functionality, are documented here as well.

Chapter 3 presents experimental work examining the effects of preload and loading rate on the fracture behavior of a woven composite. The shock tube apparatus, in conjunction with a pre-loading fixture, is utilized to impose a mode-I loading condition on preloaded single edge notched tension (SENT) specimens. High speed, full-field digital image correlation is coupled with an over-deterministic numerical analysis to extract stress intensity factors in an orthogonally woven composite subjected to pre-load followed by

dynamic loading. For the dynamic loading cases, the critical stress intensity factors and crack velocities are shown to be dependent on the amount of applied preload. Furthermore, the critical stress intensity factors obtained from the dynamic experiments with initial preload are larger than those observed in corresponding quasi-static tests. Finally, the effect of fiber orientation angle is also observed for both the preloaded dynamic experiments and the quasi-static experiments.

Chapter 4 exhibits another application of the shock tube apparatus, wherein the shock tube is paired with a projectile to examine the effects of foam density and loading rate on the mechanical behavior and failure mechanisms of a rigid closed cell foam. High speed 3D digital image correlation is used to acquire strain and displacement fields while observing failure mechanisms, while a special fixture containing piezoelectric load cells is used simultaneously to acquire specimen load data. Quasi-static testing is again performed for reference, utilizing 3D digital image correlation to acquire full field displacements and strains. Results for both the quasi-static and dynamic experiments indicate that substantially higher ultimate stresses are observed during dynamic testing, suggesting substantial strain rate dependence in the material. Failure mechanisms are also seen to differ for the quasi-static and dynamic experiments, again indicating the presence of appreciable rate dependence.

Finally, chapter 5 displays the use of the torsional split Hopkinson bar apparatus to examine the effect of strain rate on the mechanical behavior of aluminum alloy 7050 in as-received and friction stir welded states. Tubular specimens fashioned from the base metal and weld material are tested at effective strain rates in the range of  $326 \text{ s}^{-1}$  to  $841 \text{ s}^{-1}$ . Quasi-static tensile tests are also performed on both the base metal and friction stir weld materials.



Microstructural observations indicate vast differences in grain size and structure between the two material states. Irrespective of strain rate, the friction stir weld material is found to exhibit a lower yield and flow stress when compared to the base metal, while simultaneously demonstrating a substantially greater tendency for work hardening. Strain rate dependence is recognizable in both material states. However, the data indicates that rate dependence it is far more appreciable in the friction stir weld material.

## TABLE OF CONTENTS

ACKNOWLEDGEMENTS.....	iii
ABSTRACT .....	iv
PREFACE .....	vi
LIST OF TABLES .....	xii
LIST OF FIGURES .....	xiii
LIST OF SYMBOLS .....	xvi
LIST OF ABBREVIATIONS.....	xvii
CHAPTER 1: INTRODUCTION .....	1
1.1 DYNAMIC MATERIAL BEHAVIOR.....	1
1.2 BACKGROUND ON EXPERIMENTAL APPARATUSES.....	1
1.3 OBJECTIVE.....	7
LIST OF REFERENCES.....	8
CHAPTER 2: DESIGN AND FABRICATION .....	10
2.1 SHOCK TUBE APPARATUS .....	10
2.2 TORSIONAL SPLIT HOPKINSON BAR .....	19
LIST OF REFERENCES.....	30
CHAPTER 3: DYNAMIC FRACTURE OF PRE-STRESSED COMPOSITES .....	31
3.1 ABSTRACT .....	49
3.2 INTRODUCTION .....	31
3.3 MATERIAL AND SPECIMEN GEOMETRY .....	35

3.4 EXPERIMENTAL METHODS.....	37
3.5 RESULTS AND DISCUSSION .....	47
3.6 CONCLUSIONS .....	61
LIST OF REFERENCES.....	63
CHAPTER 4: OBSERVATION OF PMDI FOAM SUBJECTED TO SHOCK LOADING .....	66
4.1 ABSTRACT .....	66
4.2 INTRODUCTION .....	66
4.3 MATERIAL AND SPECIMEN GEOMETRY .....	68
4.4 EXPERIMENTAL .....	69
4.5 RESULTS AND DISCUSSIONS .....	72
4.6 CONCLUSIONS .....	76
LIST OF REFERENCES.....	78
CHAPTER 5: DYNAMIC TORSIONAL EXPERIMENTS ON AA7050T-6571 .....	79
5.1 ABSTRACT .....	79
5.2 INTRODUCTION .....	79
5.3 THEORY .....	81
5.4 MATERIAL AND SPECIMEN GEOMETRY .....	85
5.5 EXPERIMENTAL APPARATUS AND PROCEDURE.....	89
5.6 RESULTS AND DISCUSSION .....	90
5.7 CONCLUSIONS .....	101
LIST OF REFERENCES.....	103
CHAPTER 6: SUMMARY AND RECOMMENDATIONS .....	105
6.1 SUMMARY .....	105

6.2 RECOMMENDATIONS .....	105
BIBLIOGRAPHY .....	111

## LIST OF TABLES

Table 3.1 Mechanical properties of composite material examined .....	35
Table 3.2 Quasi-static stress intensity factors as a function of fiber angle .....	49
Table 3.3 Pre-loaded stress intensity factors as a function of fiber angle .....	50
Table 3.4 Maximum out-of-plane displacement before crack initiation .....	57
Table 3.5 Effective dynamic stress intensity factor, $K_{ID}^{eff}$ , for different specimens .....	59

## LIST OF FIGURES

Figure 2.1 Schematic of compression driven shock tube .....	12
Figure 2.2 Threading fixture .....	13
Figure 2.3 O-ring seals at juncture of driver and driven sections .....	14
Figure 2.4 Completed shock tube and support frame .....	15
Figure 2.5 Manufacturing drawing of nozzle .....	16
Figure 2.6 Selected images from nozzle manufacturing processes .....	18
Figure 2.7 Finished nozzle and reduced diameter muzzle section.....	18
Figure 2.8 Completed blast cabinet .....	19
Figure 2.9 Schematic of TSHB apparatus.....	20
Figure 2.10 Rotary actuator, degree wheel, and valve assembly .....	21
Figure 2.11 Assembled TSHB apparatus.....	22
Figure 2.12 Established clamping mechanism designs.....	23
Figure 2.13 Current clamping mechanism design .....	42
Figure 2.14 Stress contours from FEA on clamping jaw .....	24
Figure 2.15 Manufacturing drawing of clamping jaw .....	26
Figure 2.16 Completed clamping mechanism .....	26
Figure 2.17 Manufacturing drawing of notched bolt .....	27
Figure 3.1 Schematic of fracture specimens .....	36
Figure 3.2 Shock tube apparatus.....	39
Figure 3.3 Typical pressure profiles .....	40

Figure 3.4 Pre-stress mechanism .....	41
Figure 3.5 Quasi-static and dynamic camera arrangements .....	42
Figure 3.6 Quasi-static evolution of $K_I$ .....	48
Figure 3.7 Quasi-static crack bridging .....	49
Figure 3.8 Full field displacement contours .....	50
Figure 3.9 Crack extension and velocity as a function of fiber angle.....	51
Figure 3.10 Images captured during crack propagation.....	52
Figure 3.11 Crack propagation paths for all fiber angles considered .....	55
Figure 3.12 Comparison of vertical displacement and strain histories .....	54
Figure 3.13 3D contours of out-of-plane displacement .....	56
Figure 3.14 Vertical displacement and strain fields at the instance of fracture .....	57
Figure 3.15 Evolution of dynamic $K_I$ .....	58
Figure 3.16 Critical values of $K_{ID}$ as a function of preload and fiber angle .....	59
Figure 3.17 Evolution of time rate of change in $K_I$ .....	61
Figure 4.1 Foam billets and typical specimen with speckle pattern .....	68
Figure 4.2 Quasi-static experimental setup.....	70
Figure 4.3 Dynamic experimental setup .....	71
Figure 4.4 Projectile used in conjunction with the shock tube .....	71
Figure 4.5 Quasi-static stress-strain curves .....	73
Figure 4.6 Evolution of specimen stress in dynamic experiments.....	74
Figure 4.7 Images of specimen deformation and failure in dynamic experiments .....	75
Figure 4.8 Axial strain contours from dynamic experiments obtained using DIC .....	75
Figure 4.9 Evolution of axial strain in dynamic experiments .....	76

Figure 5.1 Schematic of specimen affixed to incident and transmitter bar .....	82
Figure 5.2 Typical thin wall specimen and associated dimensions .....	86
Figure 5.3 Gage blocks used to precisely measure gage outer diameter .....	87
Figure 5.4 Orientation of specimens extracted from FSW and base metal .....	88
Figure 5.5 Optical micrograph of FSW and base metal.....	91
Figure 5.6 Typical strain histories from incident and transmitter bars .....	92
Figure 5.7 Incident, transmitted, and reflected strain pulses .....	93
Figure 5.8 Typical evolution of specimen strain rate .....	94
Figure 5.9 Typical evolution of torque ratio .....	94
Figure 5.10 Quasi-static stress-strain curves .....	96
Figure 5.11 Dynamic stress-strain curves .....	97
Figure 5.12 Fitted dynamic stress-strain curves .....	98
Figure 5.13 Work hardening rates extracted from fitted curves .....	99
Figure 5.14 SEM images of fracture surfaces.....	101
Figure 6.1 Suggested quick release coupling for shock tube.....	106
Figure 6.2 Suggested TSHB Specimen design .....	108
Figure 6.3 Diagram describing issues with clamping mechanism.....	109
Figure 6.4 Diagram of insert suggested for clamping mechanism .....	110



## LIST OF SYMBOLS

$\beta$	Reinforcing fibers orientation.
$\nu$	Poisson's ratio.
$\rho$	Material density.
$\theta$	Angular position of a point in the polar coordinate system.
$\varepsilon_{ij}$	Components of the strain tensor.
$\sigma_{ij}$	Components of the stress tensor
$B$	Specimen thickness.
$c$	Crack tip velocity.
$c_l$	Longitudinal wave speed in the material.
$c_s$	Shear wave speed in the material.
$E$	Elastic modulus of the material.
$G$	Shear modulus of the material.
$K_I$	Stress intensity factor for mode-I fracture.
$M$	Mach number.
$r$	Radial position of a point in the polar coordinate system.
$s_{ij}$	Components of the compliance matrix.
$u$	Horizontal displacement component.
$v$	Vertical displacement component.
$w$	Out-of-plane displacement component.

## LIST OF ABBREVIATIONS

SPHB.....	Split Pressure Hopkinson Bar
TSHB .....	Torsional Split Hopkinson Bar
SEM .....	Scanning Electron Microscope
CNC .....	Computer Numerical Control
FEA.....	Finite Element Analysis
SCC.....	Stress Corrosion Cracking

# CHAPTER 1

## INTRODUCTION

### 1.1 DYNAMIC MATERIAL BEHAVIOR

For some time now, the engineering community has sought to characterize the behavior and failure mechanisms of materials at elevated strain rates. The degree to which these behaviors and failure mechanisms may change, if at all, when compared to similar quasi-static cases has become increasingly important in recent years. Changes in material behavior become extremely important when attempting to correctly engineer a structure or vehicle to that will be exposed to projectile or blast weapons, potential high speed impacts, or any other even that may rapidly impose high stresses on the structure [1]. This information is valuable to engineering design, and is also of great interest to those developing constitutive models for engineering materials. When the mechanical properties of a material are observed to be sensitive to the applied strain rate, the material is said to be strain rate dependent. This sensitivity may in fact be complex, as some materials, such as copper, are known to exhibit strain rate dependence having thresholds in regard to stress level, strain level or both [2]. Detailed information regarding the high strain rate properties of metals and alloys can be found in the review article by Armstrong and Walley [3].

### 1.2 BACKGROUND ON EXPERIMENTAL APPARATUSES

The importance of material behavior under dynamic loading conditions has prompted the devotion of considerable effort to the development of experimental equipment capable of deforming a vast array of engineering materials at elevated strain

rates. The evolution of two of the oldest and best established dynamic experiments, the shock tube and split Hopkinson bar, are briefly described below.

### 1.2.1 SHOCK TUBE

A shock tube is a simple device capable of producing a compressive loading pulse with a very short rise time, which is typically used to simulate blast waves. This compressive loading pulse is delivered in the form of a shock wave, which is a highly compressed volume of gas travelling with great speed. Shock tubes appear in both compression driven and blast driven varieties, producing shock waves by way of either a pressure differential or the detonation of a small explosive charge, respectively. A shock tube consists of a tube that is sealed at one end and separated into two sections by a thin layer of material. The sealed section is filled with pressurized air in the case of the pressure driven device, or some combustible gas in the case of the blast driven shock tube. Historically, these devices have seen great versatility in terms of use, having been used in the study of diverse areas including combustion, aerodynamic properties at high velocities, shock wave characteristics, and the response of structures and materials to blast loading.

The shock tube has been present in the scientific community for over a century. French scientist Paul Vielle is credited with the first use of a shock tube in 1899 while studying combustion and detonation in tubes [4, 5]. This early shock tube utilized a small tube, approximately 22 mm in diameter, which held explosive gases in a short chamber separated from the remainder of the 6 m long tube by a thin layer of cellophane. The Cranz-Schardin camera, invented in 1929 [6], was used by Schardin in further experiments with blast driven shock tubes in 1932 [7], utilizing the high speed camera with imaging techniques to observe shock waves.

Shortly after World War II, Payman and Shepherd [8] developed the compression driven shock tube in response to concerns regarding land mines in the UK. This apparatus required that one segment of the tube, sealed from the remainder with a thin sheet of copper, be pressurized until the copper ruptured. The pressure differential existing between the pressurized section and the remainder of the tube, which existed at atmospheric pressure, would then compress the inert gases into a shock wave while driving them out of the tube. The compression driven shock tube offers obvious benefits in terms of safety and ease of use, and produce pressure pulses with much longer durations than those typically produced by actual explosions [9]. As a result, shock tubes utilized for the purpose of material characterization are very often of the compression driven type. The term “shock tube” also became prevalent in the years following WWII. With the first symposium on shock tubes, held in 1957 by the U.S. Navy and Air Force, the development of shock tubes had begun to mature [10]. By 1958, comprehensive works fully detailing shock tube theory and experimental technique, such as the work of Henshall [11], had begun to appear.

Due to the increasing prevalence of blast related damage and injuries in recent years, the shock tube apparatus has seen substantial escalation in popularity as a means of investigating these phenomenon [9, 12]. Contemporary work exemplifies the capabilities of the shock tube as a preferable apparatus for examining the behavior of a wide variety of materials subjected to a number of dynamic loading stress states. This work ranges from metals subjected to bi-axial tension [13] to high pressure blast testing of armor and combat material [14]. This versatility and capability in regards to material testing, combined with the inherent safety of the device when compared to the blast driven counterpart, makes the compression driven shock tube ideal for a research environment. As such, this device was

selected as an essential item for the dynamic material behavior research facility. Further details regarding the design and construction of the apparatus, in addition to experimental use of the device, are seen in the following chapters.

### 1.2.2 TORSIONAL SPLIT HOPKINSON BAR

The Torsional Split Hopkinson Bar (TSHB) offers a reliable means for characterizing a vast array of materials at strain rates in the range of  $10^2 \text{ s}^{-1}$  to  $10^4 \text{ s}^{-1}$ . The TSHB is actually a derivative of the split Hopkinson pressure bar (SHPB) that is also known as the Kolsky bar. The SHPB or Kolsky bar was one of the first experiments established to conduct high strain rate testing, and has since become one of the most widely used experimental methods for observing dynamic material behavior. As such, to understand and appreciate the TSHB one must first have an adequate understanding of its parent, the SHPB technique.

The development of the Split Hopkinson Pressure Bar (SHPB) apparatus began unknowingly with numerous experiments performed by John Hopkinson in the early 1870's, in which he examined stress waves in iron wires [15, 16]. Bertram Hopkinson, son of John Hopkinson, would continue this research, and by 1914 the Hopkinson pressure bar technique was born [17]. This technique was devised as a means of measuring the pressure produced at the end of a cylindrical bar, typically imposed by the impact of a bullet or the detonation of gun cotton [18]. Many years later, in 1949, H. Kolsky would devise an experiment capable of extracting the stresses and strains present in a thin specimen placed between two long cylindrical bars. This would mark the first appearance of the split Hopkinson bar as we know it today, also referred to interchangeably as the Kolsky bar [19]. Specimen loading was accomplished by the introduction of a compressive wave at the end of one bar, referred to as the incident bar, typically by detonation of a small explosive

charge. This compressive wave propagates toward the specimen, where some portion is conducted through the specimen and into the second bar, known as the transmitter bar, while the remainder is reflected away from the specimen and back into the incident bar in the form of a tensile wave

Kolsky was able to show that the portion of the compressive strain wave passing through the specimen and into the transmitter bar, identified as the transmitted wave, is proportional to the stress in the specimen. Similarly, Kolsky found that strain in the specimen was proportional to the portion of the compressive strain wave that is reflected, aptly referred to as the reflected wave. Typically, these waves are observed by way of strain gages placed on the incident and transmitter bars. The bars on either side of the specimen therefore not only act to load the specimen, but in fact become transducers for the stress and strain in the specimen. The power of the theory behind the SHPB or Kolsky bar can be adapted to both tensile and torsional variants that exist today. The first TSHB appeared in the work of Baker and Yew [20], who were able to produce shear strain waves with the sudden release of an elastically torqued section of the incident bar. This method would become known as the “stored torque” type of TSHB, while others such as Duffy [21] would use small explosive charges to introduce shear strain pulses in their experiments.

Torsion testing is shown to have some advantages when compared to the now ubiquitous compression testing. Most notably, the many frequency components of a compressive wave have varying velocities. This results in geometric dispersion, or a change in the shape of the strain pulse, as the strain wave propagates along a medium such as a bar. This may be mitigated through careful selection of bar and specimen geometries, but never totally eliminated. The frequency components of a torsional wave, however, all

travel with an identical velocity. Therefore, all frequency components are preserved and there is no geometric dispersion of a propagating shear wave [22]. This is of great consequence when extracting specimen stresses and strains, as it is vital to the underlying theory that the strain pulses observed at the strain gages on the bars, which are placed some distance from the specimen, accurately depict the pulses present at the specimen-bar interfaces. Further difficulties in SPHB testing arise as a result of radial inertia effects in the specimen. Due to the Poisson effect, the specimen will tend to expand radially. This expansion is opposed by the inertia of the specimen and also by the friction present at the interfaces between the specimen and the bars. Although these effects can again be minimized by lubricating the specimen-bar interface and carefully selecting bar and specimen geometry, a purely compressive stress state is impossible to achieve. Neither friction nor inertia are of concern with use of the TSHB, however, as the Poisson effect and interfacial friction are absent [22].

As described above, the TSHB apparatus presents some distinct advantages over both the compression and tension variants of the SHPB. Although one may argue that compression testing is technically easier in comparison, the TSHB is undoubtedly preferable in terms of versatility and limitations. Furthermore, there are some material parameters, such as the inter-laminar shear properties of composites, which require the exclusive use of the TSHB apparatus to be examined at high strain rates. For these reasons, this apparatus was chosen as one of the core pieces of equipment to be established in the dynamic behavior of materials laboratory in the department of mechanical engineering. Further detail regarding the apparatus and the theory upon which it operates are given in proceeding chapters.



### 1.3 OBJECTIVE

The objective of the work presented here is to establish a research facility that contains suitable equipment for testing a wide variety of engineering materials at strain rates in the dynamic regime, and to utilize this facility to expand the understanding of dynamic behavior in engineering materials through experimental observations. In order to achieve these goals, a TSHB apparatus and a shock tube apparatus were designed and fabricated based on conventional knowledge of such equipment, with modifications made where the author saw them appropriate. An array of test fixtures and specialized components to accompany the experimental equipment were also assembled to expand the versatility of these experimental setups. Experiments were carried out on composite, closed cell foam, and aluminum specimens exposed to tensile, compressive, and torsional dynamic loading, respectively. Experimental data and observations are compiled and presented in the form of three journal articles, presented here in forthcoming chapters.

## LIST OF REFERENCES

- [1] Meyers M. Dynamic behavior of materials 1<sup>st</sup> ed. Wiley-interscience, New York, 1994. 1-4.
- [2] Weerasooriya, T. The MTL torsional split-Hopkinson bar. MTL-TR-90-27, U.S. Army Materials Technology Laboratory, Watertown, MA, 1990.
- [3] Armstrong RW, Walley SM. High strain rate properties of metals and alloys, Int Mater Rev 2008; 53: 105-128.
- [4] Reneer DV, Hisel RD, Hoffman JM, Kryscio RJ, Lusk BT, Geddes JW. A Multi-Mode Shock Tube for Investigation of Blast-Induced Traumatic Brain Injury. J Neurotraum 2011; 28: 95-104.
- [5] Cernak I, Wang Z, Jiang J, Bian X, Savic J. Ultrastructural and functional characteristics of blast injury-induced neurotrauma. J Trauma 2001; 50: 695-706.
- [6] Vieille P. Sur les discontinuités produites par la détente brusque de gaz comprimés. Comptes Rendus de l'Académie des Sciences de Paris, 1899; 129: 1228-30.
- [7] Vieille P. Etude sur les rôles des discontinuités dans les phénomènes de propagation. Mémoire des Poudres et Salpêtres 1900; 10: 117-260.
- [8] Cranz C, Schardin H. Kinematographie auf ruhendem Film und mit extrem hoher Bildfrequenz. Z Phys 1929; 56: 147-83.
- [9] Schardin, H. Bemerkungen zum Druckausgleichsvorgang in einer Rohrleitung. Phys Zeits 1932; 4: 33-60.
- [10] Payman, W. Shepherd, WCF. Explosion waves and shock waves. Part VI: The disturbance produced by bursting diaphragms with compressed air., Proc R Soc A 1946; 186: 243-321.
- [11] Fomin, NA. 110 years of experiments on shock tubes. J Eng Thermophys 2010; 83: 1118-35.
- [12] Henshall, BD. On some aspects of the use of shock tubes in aerodynamic research. UK: H.M. Stationery Office, 1957.

- [13] Justusson B, Pankow M, Heinrich C, Rudolph M, Waas AM. Use of a shock tube to determine the bi-axial yield of an aluminum alloy under high strain rates. *Int J Impact Eng* 2013; 58: 55-65.
- [14] Courtney E, Courtney A, Courtney M. Shock tube design for high intensity blast waves for laboratory testing of armor and combat materiel. *Defense Tech* 2014; 10: 245-50.
- [15] Hopkinson J. On the rupture of iron wire by a blow. In: Hopkinson B (Editor), *Original Papers-by the late John Hopkinson, Scientific Papers*, Cambridge Univ Press, 1901.
- [16] Hopkinson J. Further experiments on the rupture of iron wire. In: Hopkinson B (Editor), *Original Papers-by the late John Hopkinson, Scientific Papers*, Cambridge Univ Press, 1901.
- [17] Hopkinson B. A method of measuring the pressure produced in the detonation of high explosives or by the impact of bullets. *Philos Trans R Soc London A* 1914; 213: 437–56.
- [18] Gama BA, Lopatnikov SL, Gillespie JW. Hopkinson bar experimental technique: a critical review. *Appl Mech Rev* 2004; 57: 223-50.
- [19] Kolsky H ~1949!, An investigation of the mechanical properties of materials at very high rates of loading. *Proc Phys Soc London B* 1949; 62: 676–700.
- [20] Baker WW, Yew CH. Strain Rate Effects in the Propagation of Torsional Plastic Waves, *J Appl Mech* 1966; 33: 917–23.
- [21] Duffy J, Campbell JD, Hawley RH. On the Use of a torsional split Hopkinson bar to study rate effects in 1100-O aluminum. *J Appl Mech* 1971; 38: 83–91.
- [22] Gilat A. Torsional Kolsky Bar Testing. In: Kuhn H, Medlin D, editors. *ASM Handbook Volume 8: Mechanical Testing and Evaluation*, Ohio: ASM; 2000, p. 505-15.

## CHAPTER 2

### DESIGN AND FABRICATION

The design and fabrication of the shock tube apparatus and torsional split Hopkinson bar apparatus are discussed herein. In most cases, the structural and mechanical design of components has been based on established equipment that is documented in the literature and/or currently in use at other research facilities. A number of improvements and modifications have been implemented in both pieces of equipment. As a result, excellent experimental data is consistently produced by both, exemplified in later chapters. All fabrication has been performed by the author at the University of South Carolina's fabrication shop, which is overseen by the Department of Mechanical Engineering.

#### 2.1 SHOCK TUBE APPARATUS

The shock tube is an apparatus that is inherently rudimentary. Although the construction of the shock tube itself is relatively simple, it does take place on a relatively large scale. The apparatus is comprised of the shock tube itself, the associated support frame, and finally a blast cabinet that serves to protect the surrounding environment.

##### 2.1.1 SHOCK TUBE

As discussed in the previous chapter, the shock tube constructed here is of the compression driven type. A compression driven shock tube is comprised of a duct, open at one end, which is separated into two sections by a thin layer of material referred to as a diaphragm. The section open to the atmosphere is referred to as the driven section, while the sealed section, almost always the smaller of the two, is referred to as the driver section.

A high pressure source of inert gas is introduced to the driver section, inducing a substantial pressure differential across the diaphragm. Pressure is increased until the diaphragm ruptures, which effectively triggers the experiment. As the expanding gas propagates through the driven section, a front of highly compressed gas moving at great velocity is formed, known as a shock wave. This shock wave exits the open end of the tube, typically exposing a specimen to some sort of simulated blast loading.

In general, the apparatus constructed here is a scaled down version of the one found at the University of Rhode Island [1]. It is, however, worthwhile to make note of several key design criteria that must be met to produce a useful piece of equipment.

1. The walls of the tube must be sufficiently rigid, as to avoid vibration under transient loading, and also to be able to withstand the applied shock pressures [2].
2. The interior surfaces of the tube should be smooth, and free of discontinuities; particularly at joints existing between segments. Both surface roughness and discontinuities are observed to increase shock attenuation [2, 3].
3. Initial conditions dictate an ideal position for the working section of the tube in relation to the test section or specimen. Therefore, one would find it advantageous to construct the tube in a modular fashion; such that the position and length of the working section can be manipulated appropriately [2, 3].

Although these aspects of design may be seen as intuitive, they are critically important and have been regarded carefully in the construction of the shock tube here. The driver and driven sections of the shock tube are comprised of 1 m segments of 6061-T6 aluminum extruded tubes of 75 mm inside diameter, 125 mm outside diameter. Two segments form the driver section, while up to six segments are constructed for the driven section. As

mentioned, these segments are modular and can be removed to adjust the position of the specimen in accordance with desired shock velocity and strength. The basic structure and orientation is depicted in Figure 2.1.

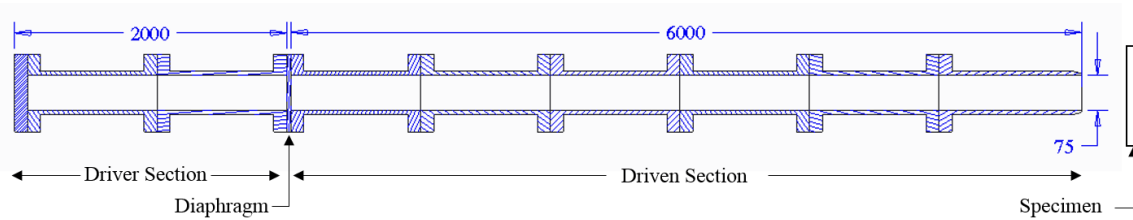


Figure 2.1 Basic structure of compression driven shock tube, with critical dimensions expressed in mm.

Segments are fastened together by way of flanged connections. The flanges are threaded onto the ends of each segment, as to avoid difficulty of welding thick sections of aluminum while maintaining structural integrity. A circular pattern of six  $\frac{3}{4}$ "-10 bolts was employed to join the abutting flanges. The sections are threaded externally, requiring the use of a lathe to perform the threading operation as the use of a die is impractical for a large diameter such as this. The process of threading each end of the tubular segment is made difficult by the substantial length of the tube, and also by the hollow center. The length of the tubular segment necessitates the use of a live center to minimize run-out at the end opposite the chuck, where threading takes place. To facilitate the use of a live center, a clever device was made to fit snugly inside the segment, providing a place to engage the live center. This device, as depicted in Figure 2.2, is constructed of a rod with a plastic cylinder fastened to each end, spanning the length of the segment and contacting the chuck, such that the live center can be firmly engaged into the conical hole drilled into the center of one of the plastic cylinders. The plastic cylinders fit snugly inside the diameter of the tubular segments, such the fixture could support the segments during machining. Flanges

were turned to appropriate inner and outer dimensions using the lathe, and then threaded internally to accept the male threads cut on the outer surfaces at the ends of the tube segments.

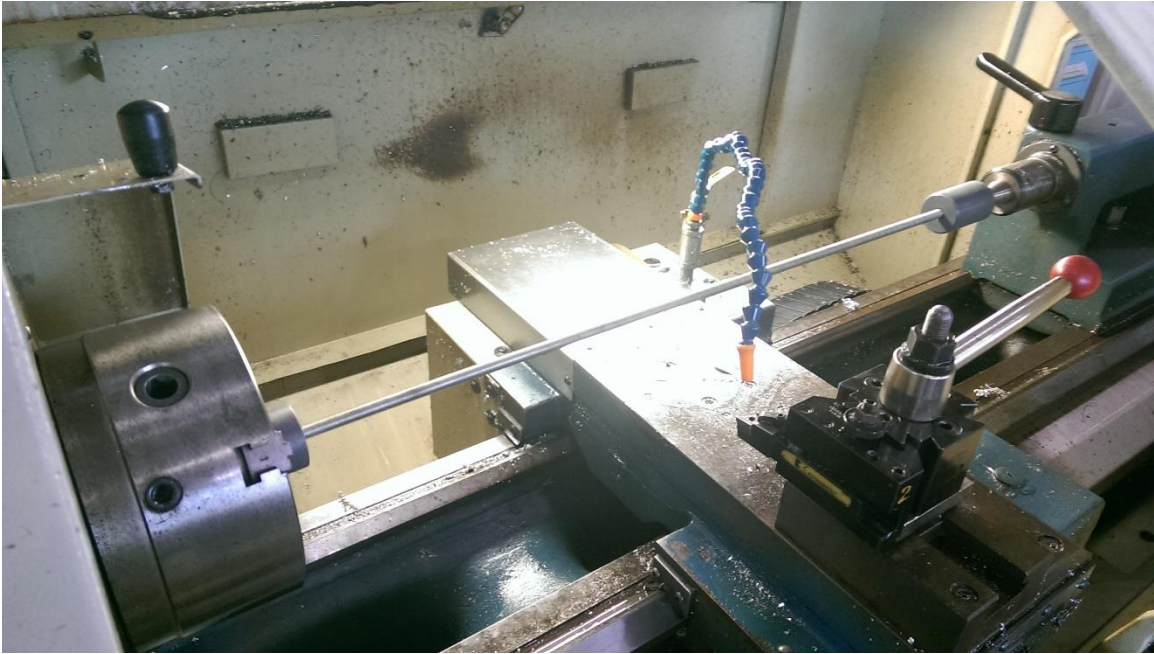


Figure 2.2 Fixture used to engage live center to support tubular segments while threading.

The driver section is sealed from the driven section with a diaphragm comprised of one or more layers of Mylar, a stretched plastic material, placed between adjacent segments of the tube. This thin sheet of material requires that an O-ring type seal be present on either side of the sheet in order to make hermetic seal with the abutting ends of the driver and driven sections. This was accomplished by re-using the device aforementioned to engage the live center, and machining two concentric grooves into the faces of the adjoining sections. These O-ring seals can be seen in Figure 2.3.

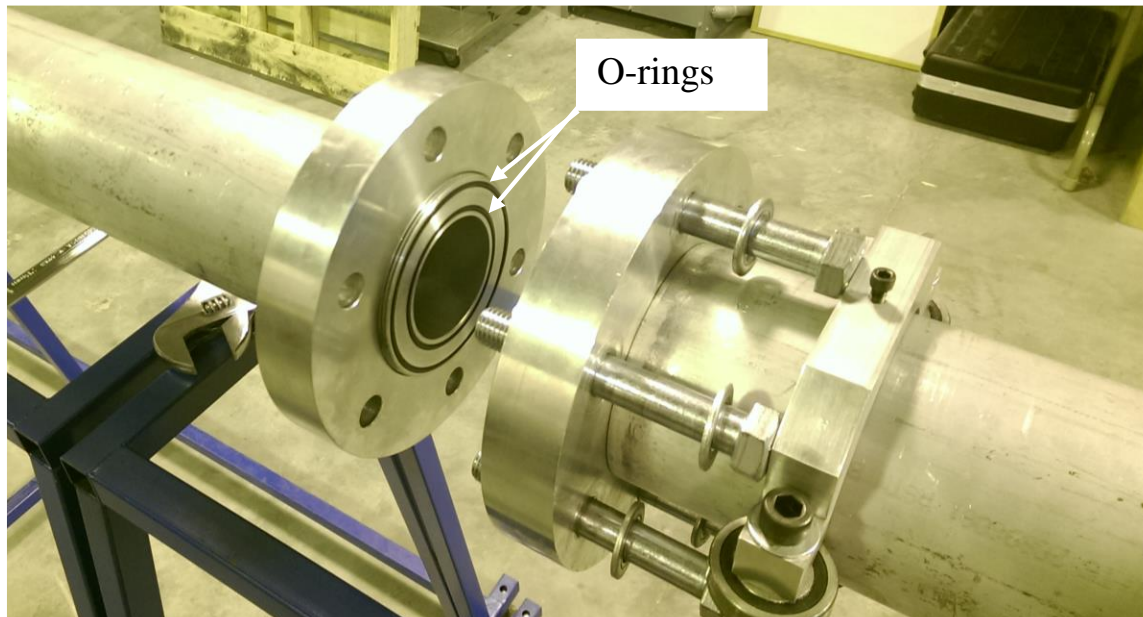


Figure 2.3 O-ring seals for Mylar diaphragm at juncture of driver and driven section.

A simple frame constructed of 1.5 mm wall thickness 25 mm square tubing was fashioned to support the shock tube. The tube is suspended upon the supporting frame by roller bearings, allowing the tube to be moved relative to the specimen, and also allowing for the working section of the shock tube to be moved based on initial conditions. The fully assembled tube and support frame can be seen in Figure 2.4.





Figure 2.4 Fully-assembled shock tube and supporting frame with roller bearings.

To facilitate higher working pressures and velocities in the shock waves produced, a short, internally tapered segment, serving as a nozzle, and a final 1 m long muzzle section were constructed. The nozzle and muzzle are designed to be interchangeable with the final segment of the shock tube, providing the option to reduce the inside diameter of the final 1 m of the shock tube from 75 mm to 50 mm. This nozzle was machined from a solid piece of 6061-T6 aluminum, 125 mm in diameter and 300 mm in length. The nozzle and its dimensions are given schematically in Figure 2.5. Again, flanges were affixed to the nozzle by way of threading.

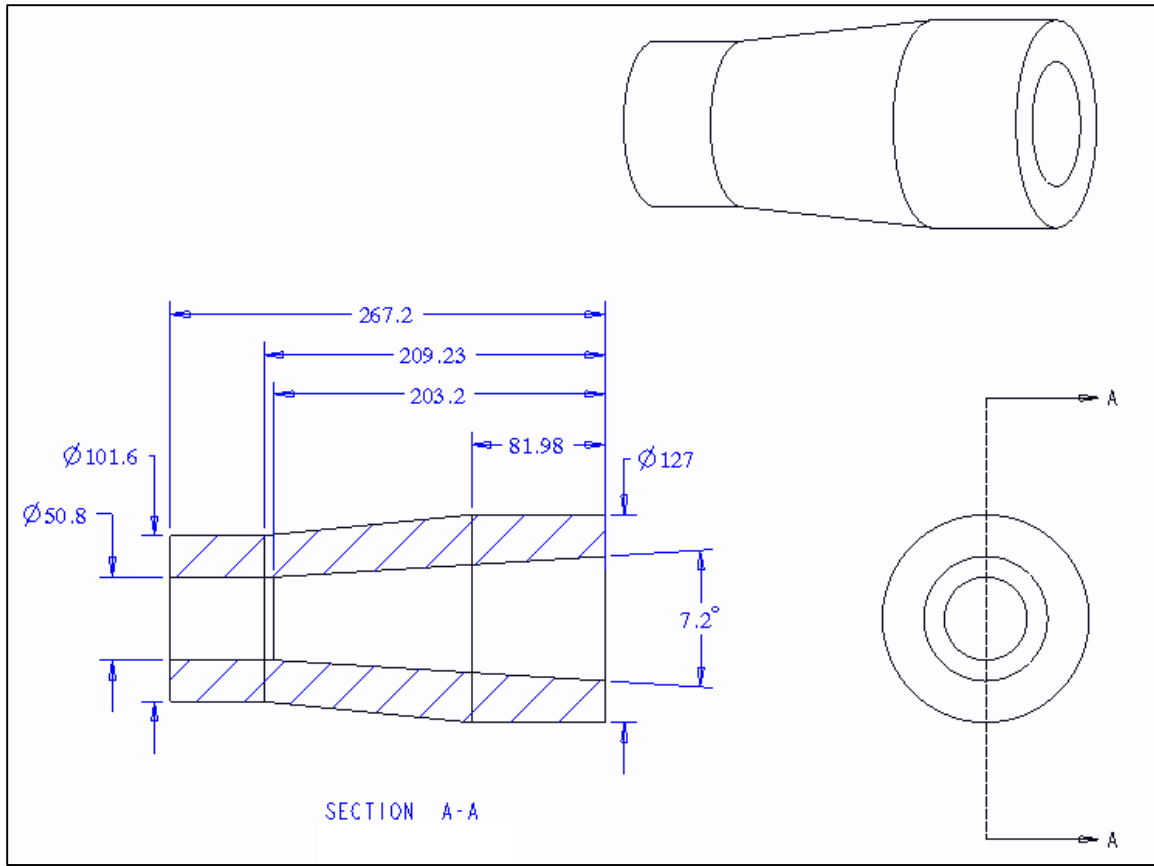


Figure 2.5 Schematic of nozzle, with all dimensions given in mm.

Machining of the nozzle was difficult because of the relatively large size and multiple operations that were required to fashion the component from a solid billet of aluminum. The large diameter allowed for only a small length to be grasped in the chuck of the lathe, due to limitations regarding the types of jaws available. As such, the order in which machining operations were carried out was carefully planned in advance. The billet of aluminum was first mounted in the lathe, with the end opposite the chuck engaged by a live center, and the outer profile of the part was turned. External threads were then machined onto the small end. While still held with the smaller end exposed, a hole was drilled and then bored to the depth which the straight portion on the smaller end extended.

Great care was taken during the drilling and boring of the small end, as only a small length of the nozzle could be held in the chuck when grasped at the large end.

With all features complete on the smaller end, the nozzle was then flipped to expose the larger end. The jaws of the chuck were able to securely grasp several inches of the length of the nozzle when held by the small end. Again employing a live center, male threads were then machined onto the large end. Finally, the remainder of the inner profile was shaped by drilling and boring the nozzle. Once again, great care was necessary due to the length by which the nozzle extended from the chuck and the length of the boring bar that was necessary to shape the taper. This combination of the component extending far past the chuck and a tool extending far from the tool post resulted in a tremendous amount of compliance when shaping the larger end of the nozzle. Large amounts of compliance in the component being machined and the tool being used make the machining operation susceptible to chatter, which yields extremely irregular surface finishes that are undesirable. In order to avoid chatter, cutting speeds were slowed far below what conventional surface velocities for machining aluminum would suggest appropriate. All processes were carried out under computer numerical control (CNC). Selected images taken during the manufacture of the nozzle are presented in Figure 2.6. Figure 2.7 shows the nozzle and muzzle assembled onto the shock tube.

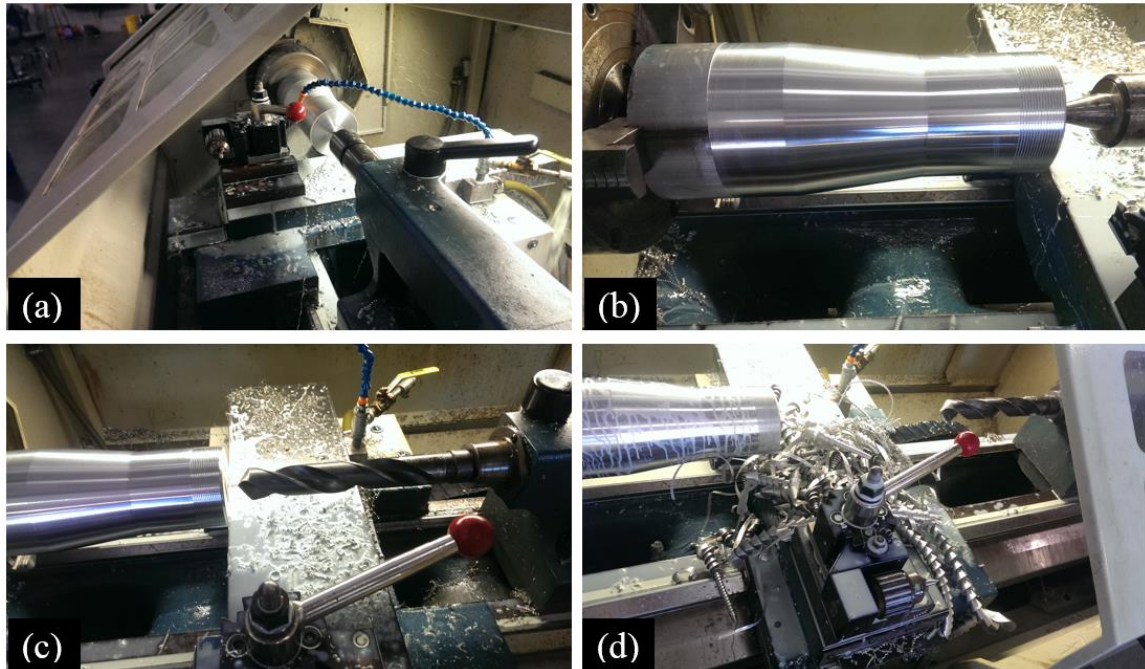


Figure 2.6 Selected images of CNC machining processes including turning (a), threading (b), and drilling (c and d).

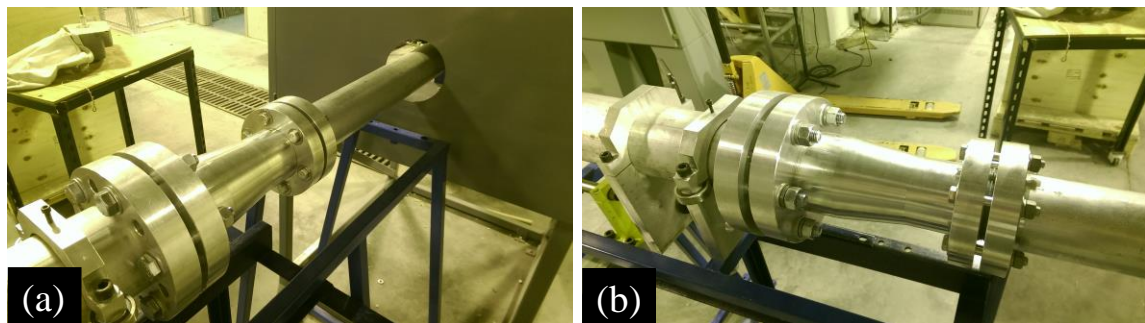


Figure 2.7 Installed nozzle as viewed from the rear (a) and from the front (b).

### 2.1.2 BLAST CABINET

A structure was assembled to isolate the surroundings from any shock waves and associated specimen debris that may be produced during an experiment, referred to as a blast cabinet. Again, this structure was predominantly modelled after the arrangement used at the University of Rhode Island [1]. Safety was held in the highest regard in designing the structure and sizing its base materials; as a result, the finished cabinet is very



robust and most likely overbuilt for any application it may see. In order to facilitate optical measurements and observations, windows were incorporated on the back and side of the cabinet. These windows were made using 12.7 mm thick sheets of polycarbonate, commercially known as Lexan, which is an optically clear material that is capable of protecting against flying debris, as it is able to undergo large plastic deformations rather than shattering in the event of an impact. Construction of this component was largely an exercise in metal fabrication skills including welding, cutting, and basic machining operations such as drilling holes. The cabinet is constructed mostly of  $\frac{1}{4}$ " steel plate, with a  $\frac{1}{2}$ " steel plate forming the floor of the enclosure as to provide a suitable surface upon which to anchor all experimental fixtures. The completed blast cabinet is shown in Figure 2.8.



Figure 2.8 Blast cabinet.

## 2.2 TORSIONAL SPLIT HOPKINSON BAR

The stored torque split Hopkinson bar or TSHB is an experimental apparatus that relies on a multitude of assumptions being valid to produce good results. Therefore, the

design and construction of such a device must be handled with care and precision. The TSHB consists of the cylindrical rods that comprise the incident and transmitter bars, a quick-release clamping mechanism, and a rotary actuator. The orientation of a typical TSHB apparatus, and the dimensions associated with the current design, can be seen in Figure 2.9. The selection and assembly of these components is detailed in the following subchapters.

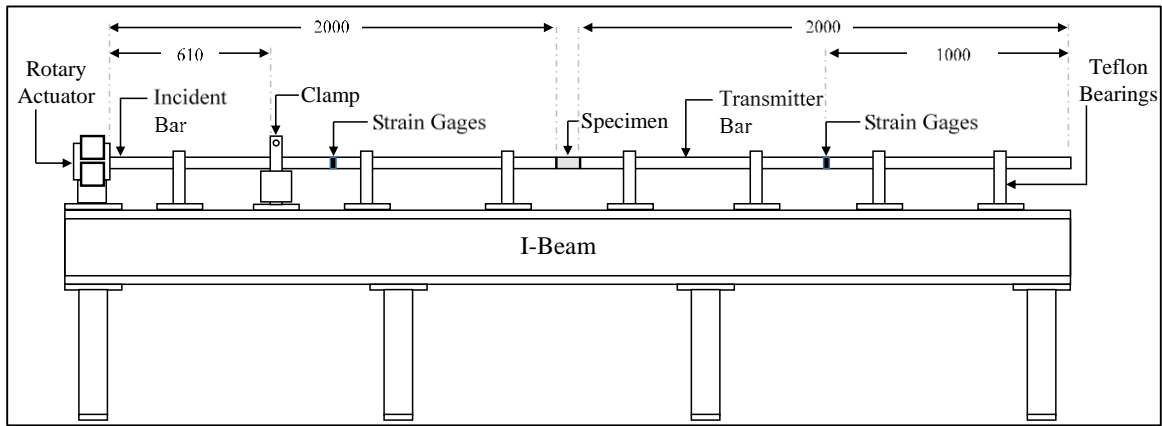


Figure 2.9 Schematic of TSHB main components.

### 2.2.1 BASIC STRUCTURE

The most prominent component of the TSHB experiment is, of course, the bars themselves. The bar material chosen was aluminum alloy 7075-T651. Aluminum was chosen in order to facilitate the widest variety of testing possible, although with some modifications bars of any material or size could be accommodated. The bar diameter utilized in this case is 25.4 mm, as is most common in TSHB apparatuses [4].

The rotary actuator chosen is a four piston hydraulic rack and pinion type. This was found to be suitable for the application because a large hydraulic pump had been sourced for the clamping mechanism, detailed later in this chapter. The rotary actuator was coupled to the incident bar with a collar and a rectangular key. To control the rotary actuator and

linear actuators from the same hydraulic pressure source, a tandem center two valve assembly was used. The tandem center valve allows for the asynchronous use of the valves controlling the linear and rotary actuators, while allowing for fluid to circulate freely when both valves are in the neutral position.

Since the predetermined angle of rotation applied to the incident bar must be measured with an acceptable level of precision, a method of observing this rotation had to be devised. The solution was to attach a degree wheel to the shaft of the rotary actuator, and fashion a pointer to indicate angular position of the shaft. By clamping the incident bar with the degree wheel indicating  $0^{\circ}$ , and then observing the reading as the shaft was rotated by the rotary actuator, a measurement of  $\pm 1^{\circ}$  was seen to be feasible. The rotary actuator, the coupling to the incident bar, the degree wheel, and the tandem center valve assembly are all seen in Figure 2.10.

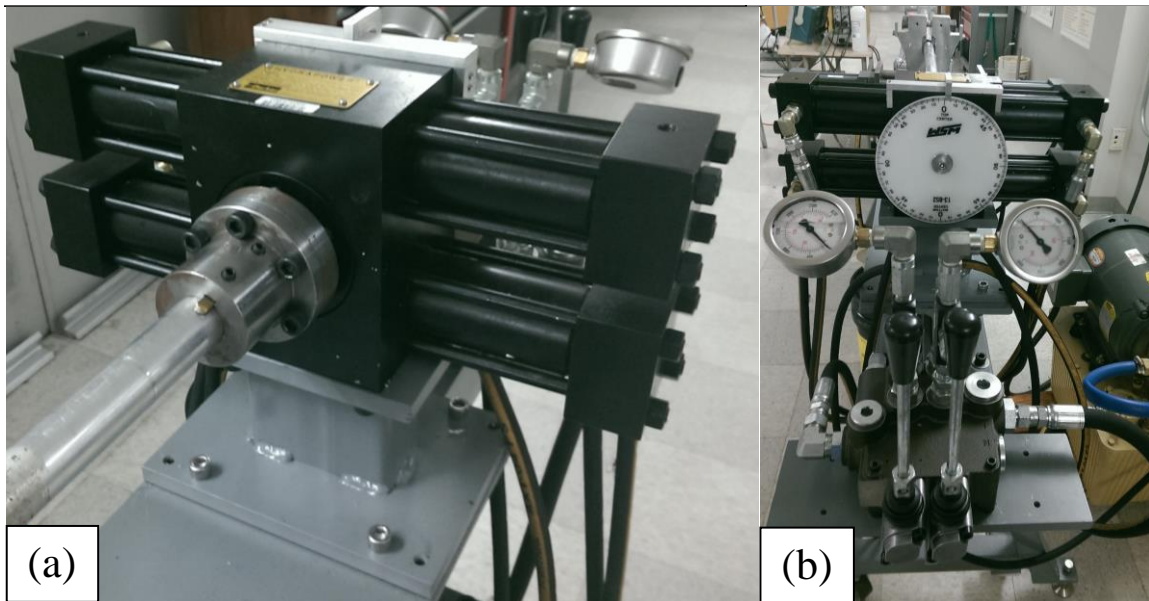


Figure 2.10 Rotary actuator and coupling (a), and degree wheel with valve assembly (b).

An I-beam was used as the platform upon which the TSHB was constructed. A total of four stands were fabricated to support the I-beam, with leveling mounts on each. With

convenience in mind, wheels were mounted on the stands at either end of the beam so that the apparatus could be easily moved with the leveling feet raised. Finally, stanchions containing Teflon bearings were used to suspend the incident and transmitter bars atop the beam. The TSHB with all components assembled is pictured in Figure 2.11.



Figure 2.11 Assembled TSHB apparatus. 2.2.2 CLAMPING MECHANISM

The clamping mechanism is the key component of a torsional Hopkinson bar that operates on a stored torque. The clamp is responsible for holding a portion of the incident bar stationary while an external torque is applied to one end, and also for instantaneously releasing the incident bar after this torque is applied. Since the notched bolt serves to facilitate this instantaneous release of the incident bar, the following sub-chapter has been devoted entirely to the design of the notched bolt. The present sub-chapter will describe



the remaining components of the clamping mechanism including the hydraulic actuators and clamping jaws.

The clamping mechanism employed here is based on earlier designs by Hartley [5] and Gilat [4], which are given in Figure 2.12. Both designs are based on a floating vise, comprised of two jaws held together by a notched pin serving as a fulcrum. Clamping pressure is applied by a hydraulic actuator in both cases. The notched pin is also fastened to the clamping jaws by way of a smaller pin in both designs.

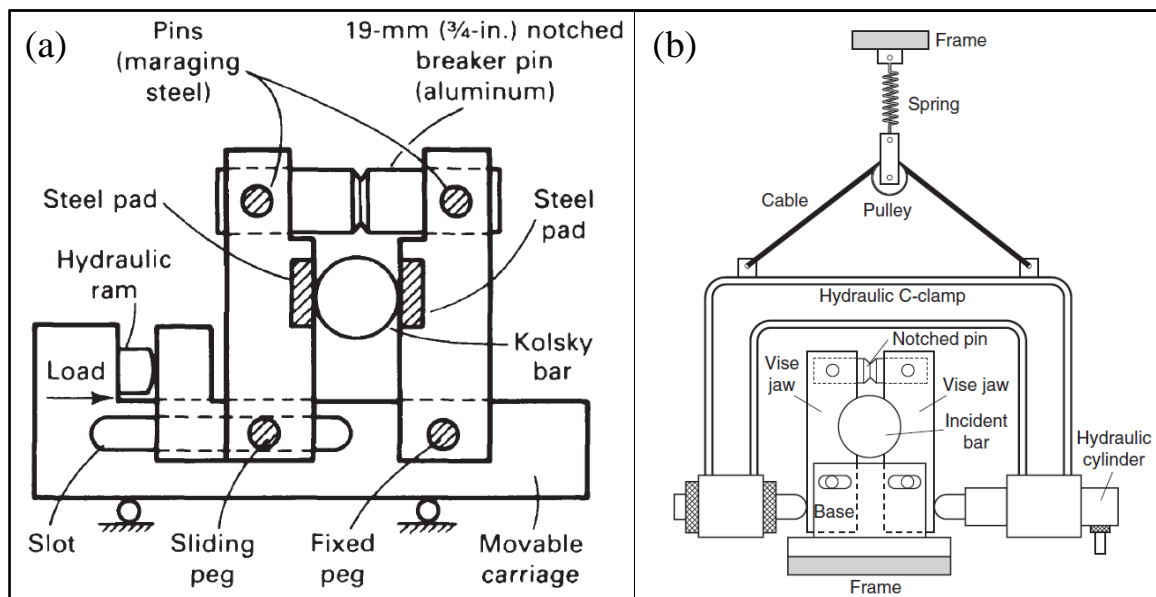


Figure 2.12 TSHB clamping mechanisms designed by Hartley [5] (a) and Gilat [4] (b).

The nature of the task necessitates that the vise float, or remain free to translate in the direction of the applied linear force, such that equal clamping force is applied to either jaw and no bending stresses are applied to the bar. The presence of bending stresses while elastically torqueing the incident bar is highly undesirable, as these result in the application of a combined stress state to the specimen. The designs of Duffy and Gilat each offer uniquely different approaches to producing a floating clamp. The clamp devised by Duffy requires that the moving carriage bear the reaction forces from the clamping jaws, while

the clamp proposed by Gilat transmits the forces bourn by the clamping jaws directly to the frame of the apparatus. The hanging C-clamp proposed by Gilat, however, is inherently compliant as a structure and may exhibit large displacements when substantial clamping forces are applied. This, in addition to appearing cumbersome, makes this hanging C-clamp unattractive for the present work. The sliding carriage contrived by Hartley, on the other hand, presents an attractive design that is more rigidly constrained against unwanted rotations and translations than the hanging C-clamp.

In light of these observations on previous clamping mechanisms, the design used here combines some desirable elements of both. In addition, some alternative mechanical features are implemented in the clamping mechanism designed and constructed here. The design is presented schematically in Figure 2.13

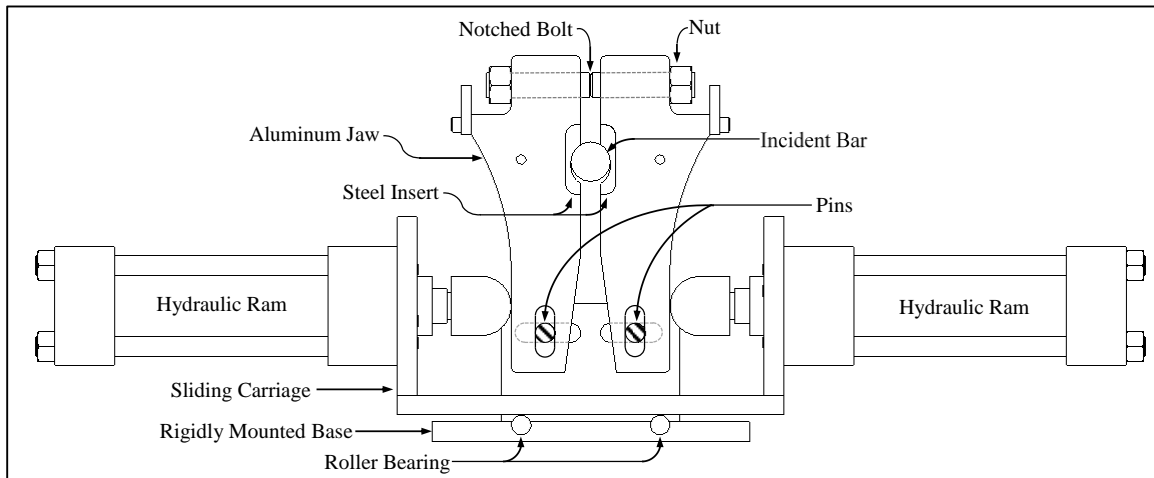


Figure 2.13 Schematic of clamping mechanism constructed in the present work.

Some key differences are evident between the design utilized in the current work and previous concepts. Most obviously, a pair of linear hydraulic actuators employed here, mounted on a sliding carriage. The use of two actuators rather than one, in conjunction with the sliding carriage, may seem redundant; however the availability of a pair of

identical actuators and the appeal of symmetry prevailed here. Another significant difference lies in the method used to fasten the notched pin to the clamping jaws. In an effort to increase simplicity of manufacture, threaded ends held in place by nuts were chosen as the preferred means of attachment. This eliminates the need to precisely locate the notch and two pin holes existing in past designs, which in practice is a nuisance as the holes and notch must be made using two different machines. Finally, the conspicuous tabs existing at either end of the notched bolt serve to capture the fragments of the bolt after it has fractured.

The shape of the clamp was designed to minimize stress concentrations around the steel insert, while accommodating features discussed above. High strength aluminum was chosen as the material of choice to minimize weight. As a result, steel inserts in the clamping jaws, as seen in the work of Duffy, were also desirable here to avoid galling of the aluminum incident bar. Using exaggerated estimates regarding clamping forces necessary in conjunction with appropriate displacement constraints, the jaw design was evaluated using finite element analysis (FEA). Effective (Von Mises) stress contours were obtained, and levels of stress near to but less than the yield stress were observed. Effective stress contours obtained from FEA are shown in Figure 2.14. After the mechanical feasibility of the clamping jaw was evaluated with FEA, jaws were machined from a 7050-T6571 aluminum plate. The associated manufacturing drawing used to produce CNC tool path is shown in Figure 2.15. The completed clamping mechanism is shown in Figure 2.16.

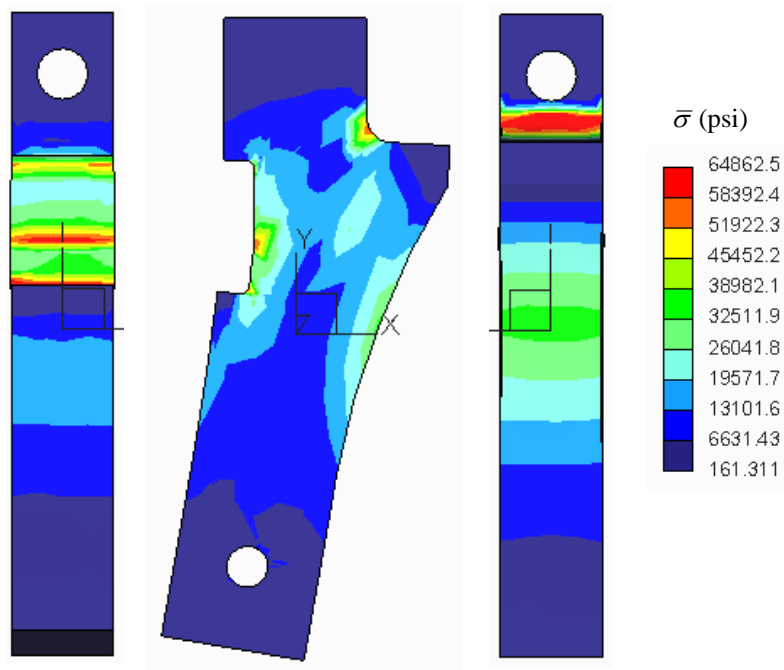


Figure 2.14 Effective stress contours obtained using FEA for the clamping jaw.

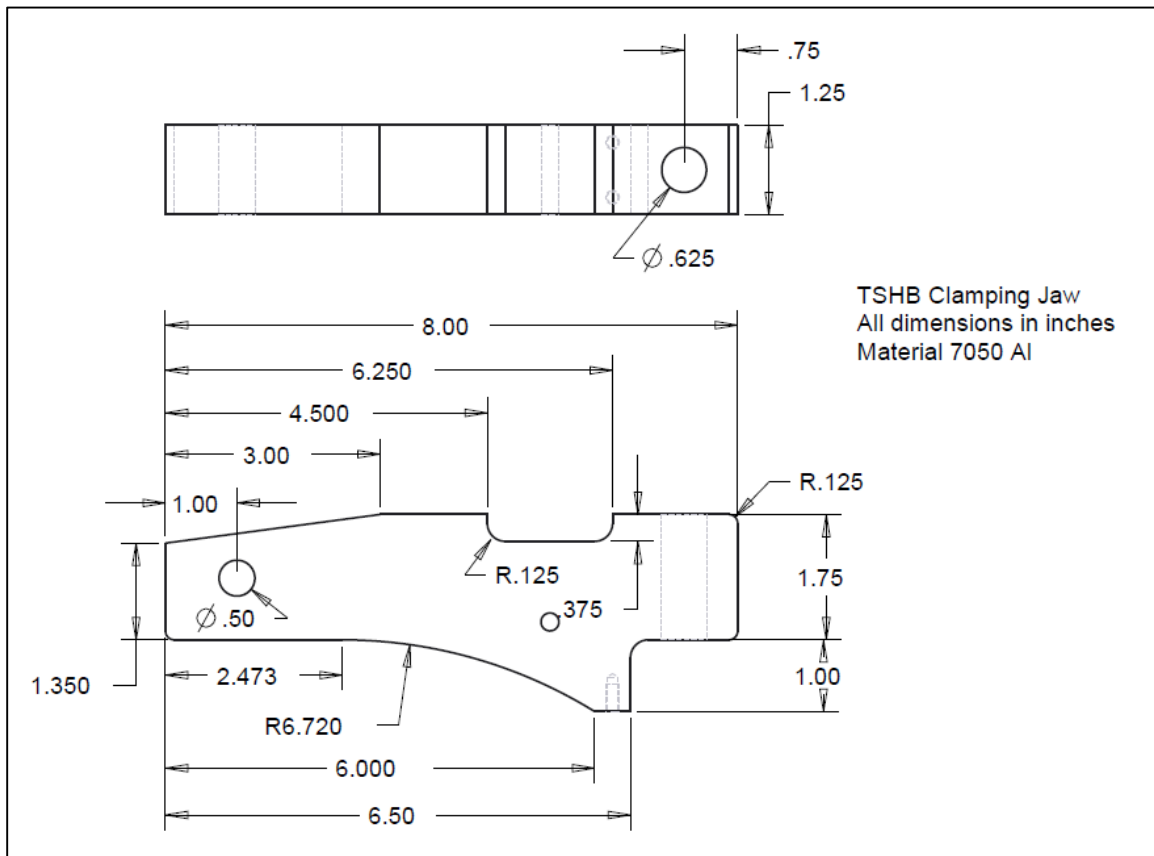


Figure 2.15 Manufacturing drawing of clamping jaw.

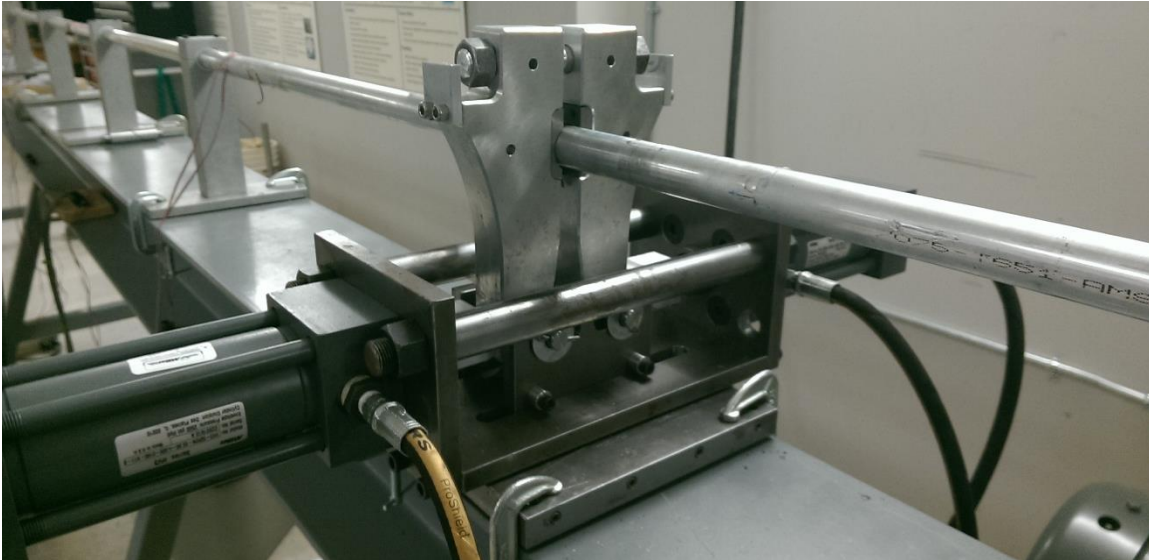


Figure 2.16 Completed clamping mechanism.

### 2.2.3 NOTCHED BOLT

The notched bolt is undoubtedly one of the most important components of the clamping mechanism. The deliberate fracture of this bolt produces the instantaneous release of the incident bar that is necessary to produce the incident strain wave. As a vital component of the experimental apparatus, several factors must be considered when designing the notched bolt. The material selected must be able to undergo a fast fracture in the presence of a sharp notch; this typically mandates harder, more brittle material. Also, a bolt is expended with every experiment done, and therefore fabrication of the bolt must be economical and timely. To facilitate economical and timely fabrication of the bolt, machining processes should be held to a minimum and a readily available, easy to machine material should be chosen. With these concerns in mind, a higher grade aluminum alloy would seem to lend itself to this application. Aluminum alloys are typically characterized by ease of machining and reasonable price. In the case of a high strength alloy such as 2024-T3, aluminum is also susceptible to fast fracture in the presence of a sharp notch. As

these criterion are all met by aluminum alloy 2024-T3, it was selected as the first choice for bolt material.

Another critical aspect of the notched bolt is the depth of the notch. The notch must be deep enough to initiate fast fracture at a load that is within the capabilities of the linear actuators used in the clamping mechanism. However, it must also be able to withstand enough stress to facilitate a firm grasp on the incident by the clamping mechanism, such that the incident bar will not slip within the clamping jaws while being torqued by the rotary actuator. As one would imagine, this aspect of the design is coupled with the material properties of both the bolt and the incident bar. The clamping pressure required is proportional to the shear modulus of the incident bar, and the clamping pressure required to break the bolt is proportional to the fracture toughness of the material comprising the bolt. It was decided to evaluate the notch depth empirically rather than analytically, as the actual force necessary to hold the incident bar stationary would require many assumptions to calculate. As such, a range of notch depths were examined before converging on a minor diameter of 0.495”.

A final aspect of the design was the selection of a suitable thread pitch for the ends of the notched bolt. It was observed that the minor diameter of a standard 5/8” coarse thread is actually smaller than the notch minor diameter of 0.495”. This results in fracture occurring in the threaded sections of the bolt at clamping loads that are smaller than those required to induce fracture at the notch. To remedy this issue, a standard 5/8” fine thread was adopted. This fine thread proved advantageous because of its larger minor diameter. The fine thread not only eliminates any possibility of fracture in the threaded connections, but also provides ease of machining by requiring removal of less material during the

threading process. The final design of the notched bolt is given in Figure 2.17 in the form of a manufacturing drawing.

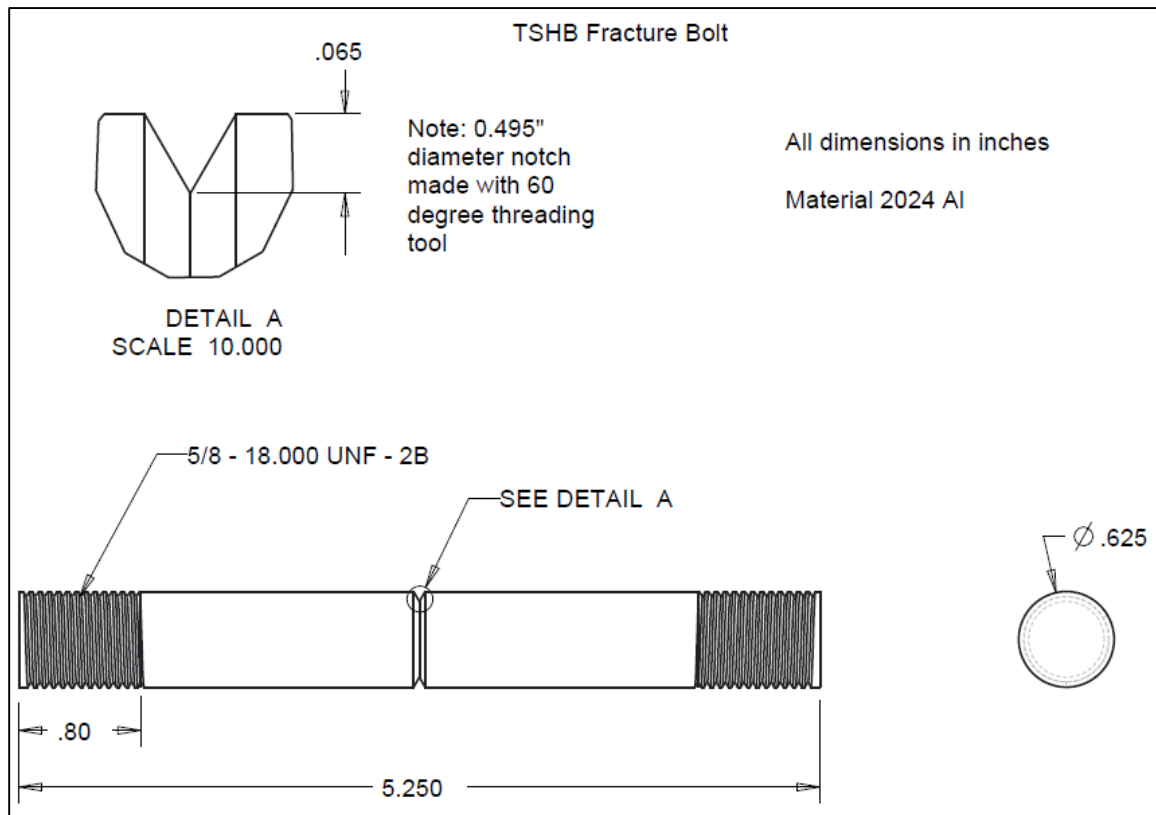


Figure 2.17 Manufacturing drawing of the TSHB fracture bolt.

## LIST OF REFERENCES

- [1] LeBlanc J, Shukla A, Rousseau C, Bogdanovich A. Shock loading of three dimensional woven composite materials. *Compos Struct* 2007; 79: 344-55.
- [2] Holder, DW. A note on shock tubes. Ministry of supply- aeronautical research council 1953; 110: 1-18 (technical note).
- [3] Henshall, BD. On some aspects of the use of shock tubes in aerodynamic research. UK: H.M. Stationery Office, 1957.
- [4] Gilat A. Torsional Kolsky Bar Testing. In: Kuhn H, Medlin D, editors. *ASM Handbook Volume 8: Mechanical Testing and Evaluation*, Ohio: ASM; 2000, p. 505-15.
- [5] Hartley KA, Duffy J, Hawley RH. The torsional Kolsky (Split-Hopkinson) bar. In: Kuhn H, Medlin D, editors. *ASM Handbook Volume 8: Mechanical Testing*, Ohio: ASM; 1980, p. 278-82.



## CHAPTER 3

### DYNAMIC FRACTURE OF PRE-STRESSED COMPOSITES

#### 3.1 ABSTRACT

The dynamic fracture behavior of a pre-stressed orthogonally woven glass fiber-reinforced composite material was experimentally investigated. A shock tube apparatus was used in conjunction with a tensile pre-loading device to apply nominally Mode-I dynamic loading to pre-tensioned, single-edge-notched specimens. The specimen response was observed with a stereo high speed camera arrangement, and the full-field displacement and strain fields near the crack tip were extracted using the 3D digital image correlation technique. Critical stress intensity factors for each specimen were determined from the displacement and strain fields using an over-deterministic approach. The magnitude of the pre-load applied to the specimens was shown to influence the crack tip velocity as well as the dynamic stress intensity factor up to the onset of crack propagation. The effect of fiber orientation on both the crack tip velocity and also the dynamic stress intensity factor was also observed.

#### 3.2 INTRODUCTION

The typical stress-strain response of fiber reinforced composite materials has been shown to exhibit an appreciable degree of strain rate dependence. Similar strain rate dependence has been observed in the fracture behavior of fiber reinforced composites, with interlaminar fracture mechanisms being the most studied phenomenon [1-5]. Interlaminar fracture is primarily a matrix property, the study of which typically has little dependence

or relevance to any reinforcing fiber property. Consequently, these results have little applicability in describing behavior relating to other fracture mechanisms. A far more limited volume of work exists in the study of fracture as a result of fiber failure, which arises in the form of fiber breakage and/or the physical release of the fiber from the matrix material, referred to as fiber bridging and eventually fiber pull-out [6]. Existing work is further limited regarding the investigation of dynamic loading combined with static tensile pre-load and the effect on the dynamic fracture of this material.

Among notable experimental studies of the quasi-static fracture of composite materials, Gouda et al. [7] utilized conventional compact tension specimen geometry and subjected the specimen to loading either along or across the fiber direction. The authors observed appreciably greater Mode-I fracture toughness for specimens loaded along the fiber direction. In their work, stress intensity factors were calculated using load data and specimen geometry [8, 9]. The effect of fiber orientation on the quasi-static fracture behavior of composites also has been documented [7, 10, 11]. Dyer et al. [10] observed particulate composite materials reinforced with various fibers embedded in different positions and orientations in three-point bend specimens. His studies showed that the position and orientation of the reinforcing fibers have a substantial effect on the load and deflection at fracture. The authors noted that fiber orientations resulting in fiber tension yielded the greatest increase in maximum load. Shukla et al. [12] experimentally determined the quasi-static Mode-I stress intensity factors present in orthotropic composite materials using strain gages. Khanna and Shukla [13, 14] later adapted this method for determining dynamic stress intensity factors, incorporating the use of multiple strain gages.

All of these techniques fail to yield any full-field data and are also typically difficult

or impossible to implement for composite materials subjected to dynamic loading. In this regard, the ability to obtain full-field data acquisition is particularly advantageous in the study of fracture mechanisms, as extraction of fracture parameters and crack tip location is better facilitated [6].

Attempts at using full-field optical measurements to evaluate stress intensity factors during dynamic loading are exemplified in interferometry based studies [1, 15]. Lambros and Rosakis [1] observed dynamic crack propagation in unidirectional graphite fiber reinforced epoxy composites. Using interferometry in conjunction with high speed photography, they were able to obtain stress intensity factors using the out-of-plane displacement component. Substantial strain rate dependence in the elastic modulus of the material and stress intensity factors largely consistent with reported values were observed. Crack initiation was shown to occur consistently in the matrix material, along the reinforcing fiber direction. Such methods are able to offer full-field observations; however, extraction of desired measurements may be tedious or impossible in some cases.

The development of digital image correlation (DIC) has facilitated more detailed optical measurement based experimental studies, observed in the works of Sutton et al. [16-21], with the evaluation of stress intensity factors for quasi-static Mode-I loading conditions. Lee et al. [3] employed a 2D-DIC in a study using single-edge notched specimens constructed of unidirectional graphite epoxy composites with various fiber orientations. They were able to extract displacement fields surrounding the crack tip, subsequently using linear and nonlinear over-deterministic least squares methods to compute both Mode-I and Mode-II stress intensity factors for quasi-static and dynamic loading cases. Stress intensity factors present at fracture were found to be consistently

lower in quasi-static experiments, compared to similar dynamic loading cases. This may have been due to the reduction fiber bridging that was observed for specimens subjected to dynamic loading. It has been further shown that 3D DIC can be effectively used to extract material properties from orthogonally woven, transversely orthotropic fiber reinforced composite materials. Pollock et al. [22] used 3D DIC in conjunction with a mechanical extensometer to measure axial strains, further employing digital image correlation to obtain transverse normal and shear strain fields. Such measurements were then shown to be effective in extrapolating a complete set of mechanical properties for such material.

Robust methods of fracture parameter extraction are of particular value in the context of composite materials, especially in the case of dynamic loading [23-25]. The established work mentioned previously has demonstrated the applicability of digital image correlation as a viable means of acquiring material response data that is suitable for extracting fracture parameters. However, much of this established work utilizes quasi-static loading rates. Those studies that do examine dynamic loading conditions typically utilize a Hopkinson pressure bar apparatus in conjunction with 2D observations, assuming negligible out-of-plane displacements. Work of such nature is somewhat established in the examination of unidirectional fiber-reinforced composite behavior, but quite limited in the study of woven fiber-reinforced composites.

In the current work, stereo high speed photography is utilized in conjunction with 3D digital image correlation to examine the fracture behavior of an orthogonally woven composite material exposed to combined quasi-static and dynamic Mode-I loading. The effects of both fiber orientation and also magnitude of applied tensile pre-stress are studied. Appreciable out-of-plane displacements, in addition to in-plane displacement and strain

fields, are measured and stress intensity factors up to the onset of crack growth are extracted using an over-deterministic least squares method.

### 3.3 MATERIAL AND SPECIMEN GEOMETRY

The specimen material used in the present work is Norplex NP130 [26], a five-layer orthogonally woven glass fiber reinforced composite with material properties listed in Table 3.1. Rectangular specimens  $254 \text{ mm} \times 127 \text{ mm}$  were extracted from 1 mm thick sheets of the composite at fiber orientations of  $0^\circ$ ,  $15^\circ$ ,  $30^\circ$ ,  $45^\circ$  and  $90^\circ$  using a Flow<sup>TM</sup> water jet. The finished specimens were single-edge notched specimens with a 46 mm initial notched crack, as well as three 13 mm mounting holes on either end. The typical specimen geometry is shown in Figure 3.1. Before testing, each specimen notch was struck with a razor blade, effectively producing a sharp crack ahead of the original notch tip with an initial length of approximately 2 mm.

Table 3.1 Mechanical properties of composite materials examined [20, 24].

$\beta (^\circ)$	0	15	30	45	90
$E$ (GPa)	25.9	23.5	16.8	14.6	23.2
$\nu_{12}$	0.15				
$\rho$ (kg.m <sup>-3</sup> )	1800				

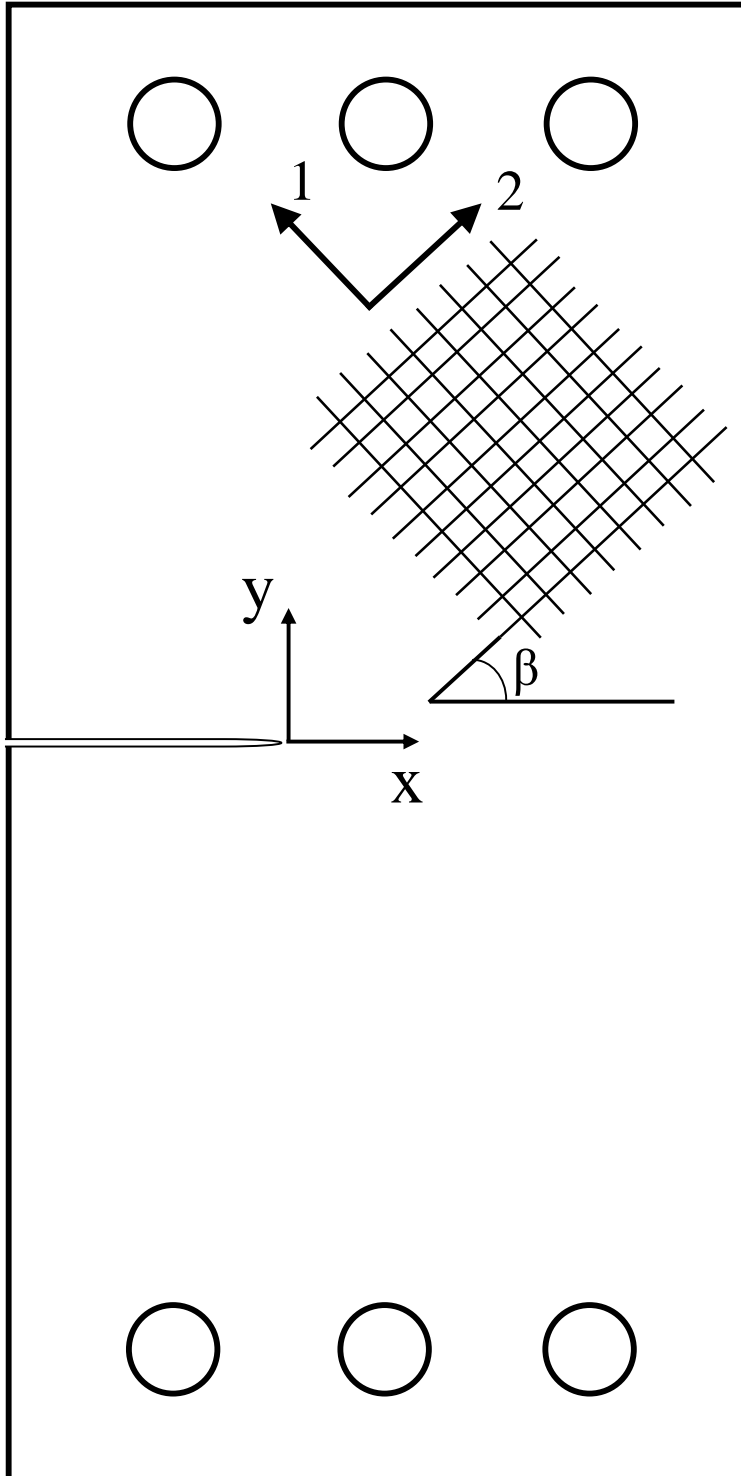


Figure 3.1 Schematic of fracture specimen.  $\beta$  denotes the fiber orientation with respect to the Cartesian coordinate system. Note, the initial notch for all specimens is parallel to the x axis

### 3.4 EXPERIMENTAL METHOD

In order to examine the effect of pre-loading on the fracture behavior of single-edge notched specimens, an initial tensile load was applied to each specimen using a specially built fixture described in Section 3.2. Fracture was then initiated with the application of controlled dynamic load using the shock tube apparatus described in Section 3.1. With the use of a stereo high speed camera arrangement, in conjunction with 3D digital image correlation, displacement and strain fields were measured and recorded during loading. Using these displacement and strain fields, an over-deterministic least squares method was implemented to extract fracture parameters. In addition, comparable quasi-static experiments were performed and observed for comparison and validation purposes.

#### 3.4.1 LOADING APPARATUS

A shock tube was used to subject the specimens to a well-controlled dynamic load. A detailed description of the shock tube and its calibration can be found in the literature [27]. A shock tube is a relatively simple instrument used to replicate blast waves. A typical shock tube consists of a circular tube, open on one end, separated into two sections by a diaphragm. The section open to atmospheric pressure is referred to as the driven section, while the sealed section, pressurized to some appreciably greater level, is referred to as the driver section. With the application of a pre-determined pressure, the diaphragm rapidly bursts, producing a series of waves that compress into a shock, which propagates down the shock tube before it exits the driven section and contacts the specimen. The shock tube used in the current work consisted of a driver section 1.8 m in length and a 5.5 m long driven section with a constant inside diameter of 76.2 mm over the length of the tube. Sheets of Mylar, a stretched polyester film, were utilized as the material of choice for the

diaphragm. Figure 3.2 shows the shock tube apparatus used in the current study. The velocity and magnitude of the pressure wave produced by the shock tube were varied by increasing or decreasing the number of Mylar sheets comprising the diaphragm. Piezo-electronic pressure sensors mounted in the muzzle of the shock tube, very near to the specimen, were used to observe incident and reflected pressures. These sensors were also utilized as a reliable means of triggering both the data acquisition and image acquisition processes. Typical pressure profiles obtained for different numbers of Mylar sheets are depicted in Figure 3. It must be noted here that, in the current study all shock tube experiments are conducted using 3 Mylar sheet diaphragms. Often the specimen can be held in a fixture, depending on the boundary conditions required. In the current study, the ends of each specimen were held in a fixture used to apply a constant pre-tension load. This fixture is described thoroughly in the next section.



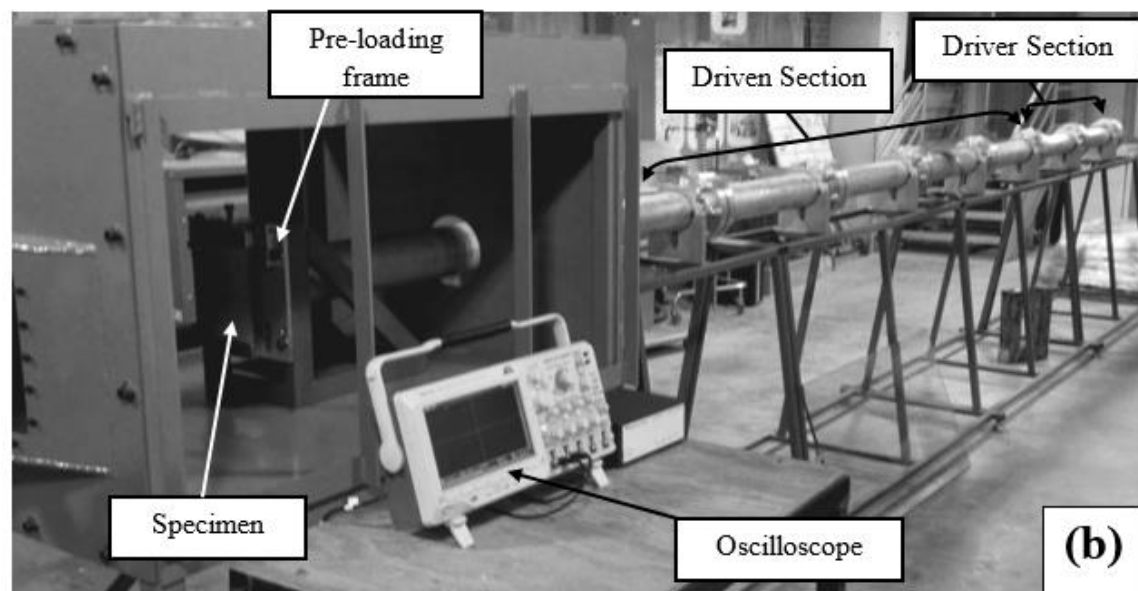
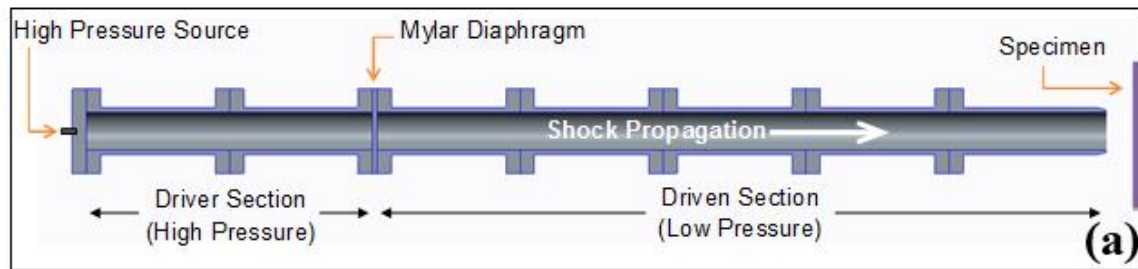


Figure 3.2 The shock tube apparatus used in this work (a) schematic drawing and (b) actual apparatus

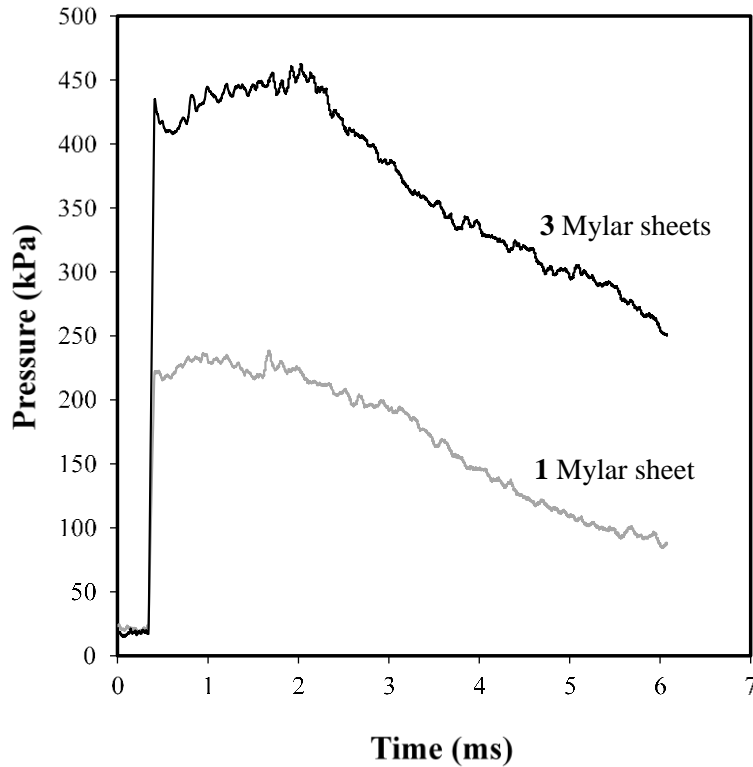


Figure 3.3 Typical pressure profiles as a function of the number of Mylar sheets

#### 3.4.2. PRESTRESS MECHANISM

The mechanism used to apply a pre-stress to the specimens is depicted in Figure 3.4. A configuration of steel die springs mounted on the fixture ensures that a consistent pre-load is applied to the specimen. Since the applied pre-stress is solely dependent on the displacement of the die springs, the configuration can be altered in a number of ways to achieve a range of possible pre-stress values. The inner (A) or outer pair (B) of springs can be added or removed from the apparatus entirely and the spring constant can be altered. Two values of pre-load have been examined; the first pre-load magnitude has been achieved by using only the inner pair of die springs, producing a pre-load of approximately 1750 N, and the second pre-load magnitude has been achieved by subsequently adding the outer pair, producing a pre-load of approximately 3500 N. The springs are compressed by

way of a  $\frac{1}{2}$ -20 bolt (C) that moves the upper specimen mount down to a position such that the specimen can be bolted into the fixture. When the specimen is fastened into the fixture, the  $\frac{1}{2}$ -20 bolt is retracted, thus applying spring tension to the specimen. Subsequently, a  $\frac{1}{4}$ -28 bolt (D) between each pair of springs that is threaded into the upper specimen mount is snugly tightened, thus locking the mechanism and allowing the specimen to be pre-loaded prior to initiating the shock loading process.

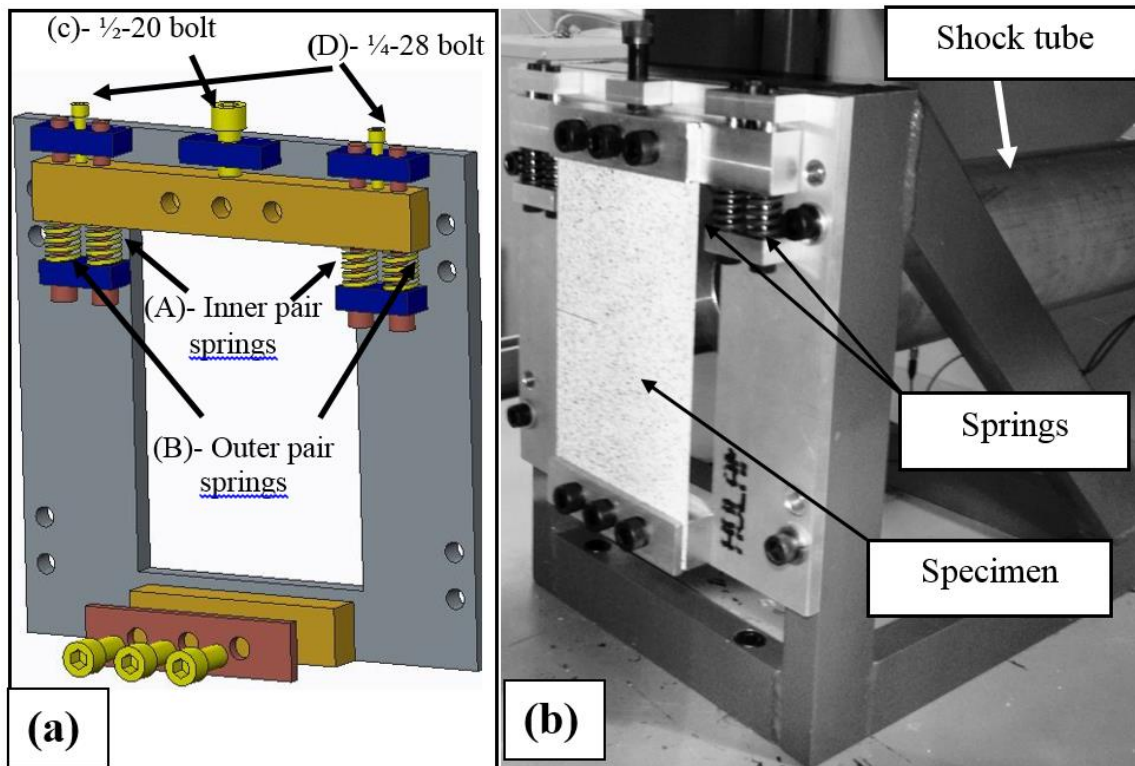


Figure 3.4 The mechanism utilized to apply the pre-tension to the specimen (a) schematic drawing and (b) actual frame with the mounted specimen

### 3.4.3 DIGITAL IMAGE CORRELATION SYSTEM

To facilitate image correlation, a fine speckle pattern was applied to the specimens prior to the experiments. To do so, white paint was applied to the specimen surface. Then, a black speckle pattern was applied on top of the white paint using an air gun, resulting in a rather uniform high contrast pattern. A Photron SA-X2 stereo high speed camera system

was used to capture the full-field three-dimensional specimen response in both quasi-static and dynamic loading conditions. In both loading conditions, camera resolution of  $384 \times 264$  was used. Images were captured at 60 fps in the quasi-static case, and 96,000 fps in the dynamic loading case. Piezoelectric pressure sensors mounted in the muzzle of the shock tube were employed to trigger image acquisition with the use of an oscilloscope, while image acquisition was manually triggered in the quasi-static case. The camera arrangements for both dynamic and quasi-static cases are shown in Figure 5. Images taken during the loading were then exported to the commercial software Vic-3D [28] for further analysis. In this software, subset and step sizes of 17 and 3 pixels, respectively, were used to calculate the displacement and strain components during the loading stage. Note that the resolution of the measurements in this work was 0.17 mm/pixel in all cases.

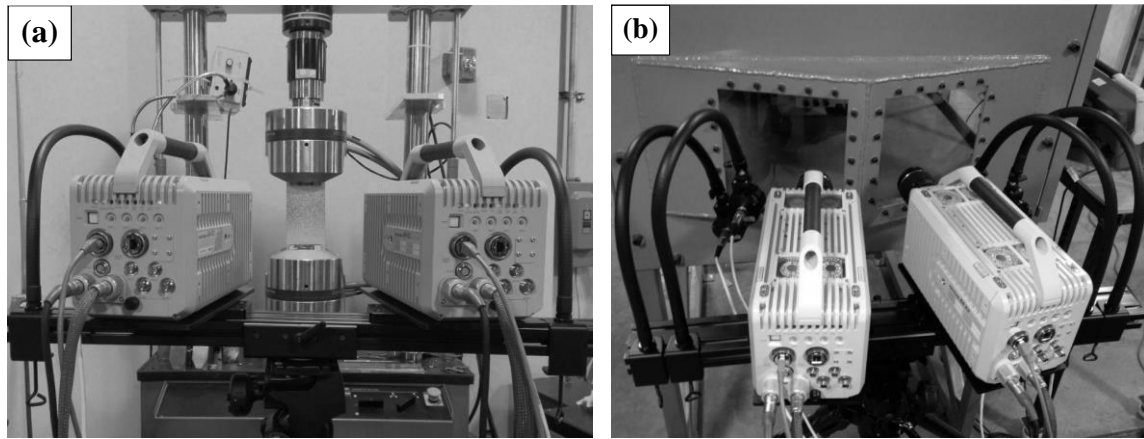


Figure 3.5 Camera arrangements for (a) quasi-static and (b) shock tube experiments

#### 3.4.4 QUASI-STATIC TESTING

As a benchmark, a quasi-static fracture study was conducted using similar specimen geometry. The stress intensity factors found in this quasi-static study were used as a point of reference for the evaluation of values obtained in the pre-stressed specimens exposed to dynamic loading. To facilitate the quasi-static loading, a 110 kN capacity MTS machine

was employed. Using 101.6 mm wide grips, the specimen was fastened into the MTS machine as similarly as possible to the pre-load fixture. Specimens were fastened into the tensile frame using 6 mm thick aluminum tabs placed on either side of the specimen thickness to minimize the damage from serrated, hardened steel grips. The quasi-static tests were conducted at room temperature, under displacement-control loading with a cross head speed of 0.0254 mm/s. An imaging procedure identical to that used in the dynamic experiments and 3D digital image correlation was utilized to measure full-field displacement and strain response. The stress intensity factors were extracted from the measured displacement fields using both an over-deterministic approach and also load data up to the onset of crack propagation, in conjunction with specimen geometry.

### 3.4.5 DATA ANALYSIS

The stress intensity factors for specimens having various fiber orientations loaded under quasi-static and dynamic conditions were calculated using an over-deterministic procedure based on a least-square optimization. The detailed procedure can be found elsewhere, [11, 29], and is presented briefly here. The in-plane displacement components,  $u$  and  $v$ , for an orthotropic composite material subjected to Mode I loading can be written as [3, 14]:

$$u = \frac{K_I}{\sqrt{\pi}} Ac_{66} \left[ - \left( \frac{l_1}{\alpha} s_{11} + p^2 l_3 s_{12} \right) \sqrt{\cos^2 \theta + \frac{1}{p^2} \sin^2 \theta + \cos \theta} + \left( \frac{pl_2 l_5}{\alpha q l_6} s_{11} + \frac{pq l_4 l_5}{l_6} s_{12} \right) \sqrt{\cos^2 \theta + \frac{1}{q^2} \sin^2 \theta + \cos \theta} \right] \sqrt{r} \quad (3.1a)$$

$$\begin{aligned}
v = & \frac{K_I}{\sqrt{\pi}} Ac_{66} \left[ -p \left( \frac{l_1}{\alpha} s_{12} + p^2 l_3 s_{22} \right) \sqrt{\cos^2 \theta + \frac{1}{p^2} \sin^2 \theta - \cos \theta} \right. \\
& \left. + q \left( \frac{pl_2 l_5}{\alpha q l_6} s_{12} + \frac{pq l_4 l_5}{l_6} s_{22} \right) \sqrt{\cos^2 \theta + \frac{1}{q^2} \sin^2 \theta - \cos \theta} \right] \sqrt{r}
\end{aligned} \tag{3.1b}$$

where  $K_I$  is the stress intensity factor for Mode-I fracture.  $s_{ij}(i, j = 1, 2, 6)$  in these equations represent the elements of the compliance matrix (Eq. 2), assumed to be strain rate-independent in this work.

$$\begin{bmatrix} \epsilon_{xx} \\ \epsilon_{yy} \\ \gamma_{xy} \end{bmatrix} = \begin{bmatrix} s_{11} & s_{12} & 0 \\ s_{21} & s_{22} & 0 \\ 0 & 0 & s_{66} \end{bmatrix} \begin{bmatrix} \sigma_{xx} \\ \sigma_{yy} \\ \tau_{xy} \end{bmatrix} \tag{3.2}$$

Subscripts 1 and 2 in Eq. (2) denote the axial and transverse fiber axes of the composite specimen, respectively, as shown schematically in Figure 3.1. Quantities  $r$  and  $\theta$  denote the radial and angular coordinates of an arbitrary point with respect to the original crack tip, respectively. Parameters  $p$  and  $q$  are defined as:

$$p = \sqrt{a_1 - \sqrt{a_1^2 - a_2}} \quad , \quad q = \sqrt{a_1 + \sqrt{a_1^2 - a_2}} \tag{3.3}$$

where  $a_1$  and  $a_2$  are functions of the components of the material's stiffness matrix,  $c_{ij}$ ,

and Mach numbers (relative crack tip velocities),  $M_1$  and  $M_2$ , defined as:

$$2a_1 = \alpha + \alpha_1 - 4\beta_1\beta_2 \quad , \quad a_2 = \alpha\alpha_1 \tag{3.4a}$$

$$\begin{aligned}
\alpha &= \frac{c_{66}}{c_{11}(1 - M_1^2)} & \alpha_1 &= \frac{c_{22}}{c_{66}(1 - M_2^2)} \\
2\beta_1 &= \frac{c_{12} + c_{66}}{c_{11}(1 - M_1^2)} & 2\beta_2 &= \frac{c_{12} + c_{66}}{c_{66}(1 - M_2^2)}
\end{aligned} \tag{3.4b}$$

$M_1$  and  $M_2$  are defined as the ratio of the crack tip velocity with respect to longitudinal wave velocity,  $c_l$ , and shear wave velocity,  $c_s$ , respectively, and can be expressed as,

$$M_1 = \frac{c}{c_l} \quad M_2 = \frac{c}{c_s} \quad \text{with} \quad c_l = \sqrt{\frac{c_{11}}{\rho}} \quad c_s = \sqrt{\frac{c_{66}}{\rho}} \quad (3.5)$$

where  $\rho$  represents the mass density of the composite.

The parameters  $l_i (i = 1 \dots 6)$  and  $Ac_{66}$  in Eq. (3.1) can be expressed as:

$$\begin{aligned} l_1 &= \frac{2\beta_1 p^2}{(\alpha - p^2)(1 - M_1^2)} + 2\beta - \alpha & l_2 &= \frac{2\beta_1 q^2}{(\alpha - q^2)(1 - M_1^2)} + 2\beta_1 - \alpha \\ l_3 &= 1 - M_2^2 - \frac{2\beta_1}{\alpha - p^3} & l_4 &= 1 - M_2^2 - \frac{2\beta_1}{\alpha - q^2} \\ l_5 &= -l_3 - M_2^2 & l_6 &= -l_4 - M_2^2 \\ Ac_{66} &= \frac{l_6}{pq l_4 l_5 - p^2 l_3 l_6} \end{aligned} \quad (3.6)$$

Eq. (3.1) has originally been proposed for the case of dynamic crack propagation [3, 14]. In the case of a stationary crack subjected to either dynamic or quasi-static loading, the above equation can be simplified by taking  $c$  to be zero.

The only unknown parameter in Eq. (3.1) is  $K_I$ , as  $u$  and  $v$  at any position  $r$  and  $\theta$  can be obtained from displacement fields obtained using DIC. The measured displacement components at arbitrary radial positions in the crack tip vicinity, obtained from DIC, were used as input to a computer code written on the MATLAB<sup>TM</sup> platform to calculate the stress intensity factor for the material based on the over-deterministic approach detailed in [29-32]. When using the over-deterministic least-square analysis, one should bear in mind that data points selected for the numerical approach should be sufficiently far from the crack tip area to avoid tri-axial conditions and the effects of local plasticity which are most

evident in a region near the crack tip. In this work, data points outside the circular region,  $r > 0.5B$  (with  $B$  being the specimen thickness) were taken for the analysis [3]. A large number of data points is required to extract the stress intensity factor with acceptable accuracy [29, 31]. Accordingly, a minimum number of 100 data points was considered as input for the analysis to assure the accuracy of the calculated  $K_I$ .

In attempting to identify the exact moment of crack initiation, exclusive use of displacement components may be insufficient. This is due to a continuous increase of displacement components, especially the opening component of displacement,  $v$ , even after crack initiation. Therefore, the sole use of displacement measurements may introduce substantial inaccuracy in the calculated values of  $K_I$ . The uncertainty can be lowered when the vertical strain component  $\varepsilon_{yy}$  is considered since  $\varepsilon_{yy}$  at a location behind but very near to the initial crack tip experiences a sudden drop at the instance of crack propagation [14]. As such, opening strain  $\varepsilon_{yy}$  was used to determine the crack initiation time in the case of dynamic loading. The stress intensity factor at the onset of crack growth was then calculated using both strain and displacement fields. The in-plane strain components  $\varepsilon_{xx}$  and  $\varepsilon_{yy}$  are related to the stress intensity factor as [14]:

$$\begin{aligned}\varepsilon_{xx} &= \frac{K_I}{\sqrt{2\pi r}} \cos\left(-\frac{\theta}{2}\right) Ac_{66} \left[ \left( -\frac{l_1}{\alpha} s_{11} - p^2 l_3 s_{12} \right) + \left( \frac{pl_2 l_5}{\alpha q l_6} s_{11} + \frac{pql_4 l_5}{l_6} s_{12} \right) \right] \\ \varepsilon_{yy} &= \frac{K_I}{\sqrt{2\pi r}} \cos\left(-\frac{\theta}{2}\right) Ac_{66} \left[ \left( -\frac{l_1}{\alpha} s_{12} - p^2 l_3 s_{22} \right) + \left( \frac{pl_2 l_5}{\alpha q l_6} s_{12} + \frac{pql_4 l_5}{l_6} s_{22} \right) \right]\end{aligned}\tag{3.7}$$

The additional parameters in Eq. (3.7) are identical those explained earlier for the displacement field, i.e. Eqs. (3.2) to (3.6).



## 3.5 RESULTS AND DISCUSSION

### 3.5.1 QUASI-STATIC TESTING

A typical evolution of the quasi-static stress intensity factor prior to crack initiation is shown in Figure 3.6. As can be seen in Figure 3.6, reasonable agreement between stress intensity factors extracted using DIC and load data has been observed up to the instant of crack initiation. The stress intensity factors for  $\beta = 0^\circ$ ,  $45^\circ$  and  $90^\circ$  specimens under quasi-static loading conditions obtained using both the recorded load data in conjunction with specimen geometry and the full-field DIC data are shown in Table 3.2. In all cases, it is observed that the value calculated based on the DIC data is slightly higher than that determined using the maximum recorded load. Such a level of discrepancy has also been reported previously in [31, 32], especially when single-term asymptotic displacement expressions have been utilized. In addition, it has recently been documented that, for the case of orthogonally woven composites, calculation of the stress intensity factor using only the far-field load introduces some level of uncertainty [11]. Such level of uncertainty is due to the difficulty in capturing the exact moment of crack initiation in these materials as a result of complicated fiber/matrix micromechanics. Thus, optical observations are required to capture the instant of crack initiation and the corresponding far-field load in order to better estimate the stress intensity factor at the onset of crack growth [11].

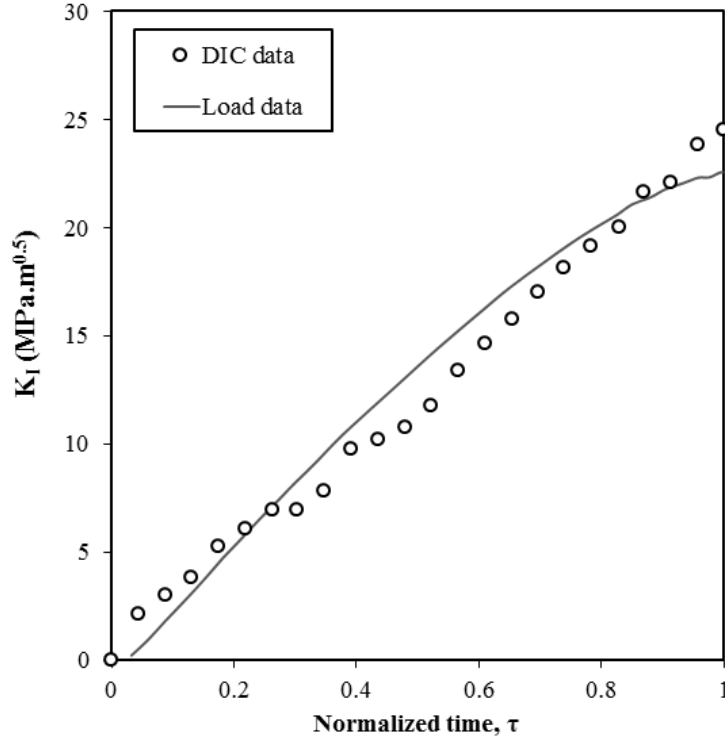


Figure 3.6 A comparison between the evolution of quasi-static  $K_I$  values determined from recorded load and DIC data prior to crack initiation for a  $\beta = 45^\circ$  specimen subjected to quasi-static loading. Note that the crack begins to grow at  $\tau = 1$ .

The stress intensity factors obtained in this work, given in Table 3.2, seem high for a composite material. When interpreting these elevated critical stress intensity factors, there are two key factors that must be understood. First, the samples are not thick enough to impose plane-strain conditions, thus resulting in a substantially increased stress intensity factor achieved at fracture. [33, 34]. Second, the material is a woven composite, and fracture occurs mainly by fiber breakage, referred to as bridging. Figure 3.7 shows the bridging effect during early stages of crack propagation for a  $\beta = 0^\circ$  specimen subjected to quasi-static loading. It has been observed that the fiber bridging is associated with a high stress intensity factor [34, 35].

Table 3.2- Quasi-static stress intensity factors as a function of fiber orientation angle.

Fiber orientation ( $\beta$ )	Stress intensity factor, $K_I$ (MPa.m <sup>0.5</sup> )		
	Recorded Load	DIC data	% difference
0°	36.05	38.26	5.7
45°	22.58	24.61	8.2
90°	28.62	30.54	6.2

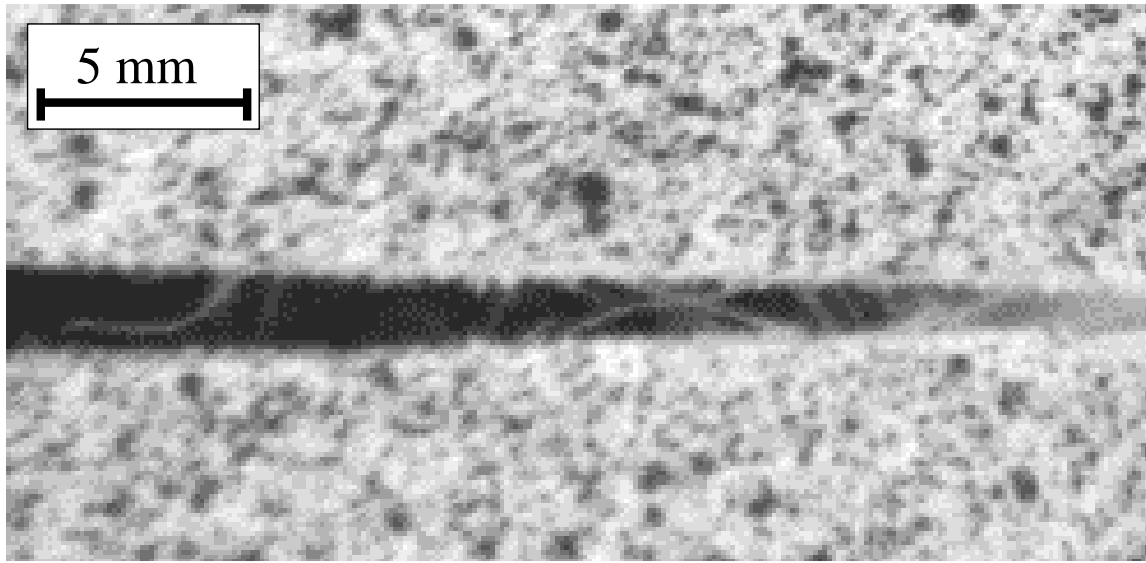


Figure 3.7 Crack bridging during early stages of crack propagation for the  $\beta = 0^\circ$  specimen subjected to quasi-static loading.

### 3.5.2. STRESS INTENSITY FACTOR ASSOCIATED WITH APPLIED PRE-STRESS

Full-field displacement distribution of specimens of each fiber orientation angle subjected to pre-load 1750 N and 3550 N are obtained using DIC. Typical displacement contours resulting from the pre-loaded  $\beta = 0^\circ$  specimen are shown in Figure 3.8. The displacement fields obtained for each specimen, along with the analysis detailed in Section 3.4.5, were used to extract the stress intensity factor of each specimen subjected to both pre-load values. The results are shown in Table 3.3. The  $K_I$  values obtained in this stage can be considered as stress intensity factors that already exist in the specimen prior to being subjected to shock loading. Using the property of superposition, this value can be added to

the values calculated from shock loading to yield an estimation of the total  $K_I$  value of each specimen.

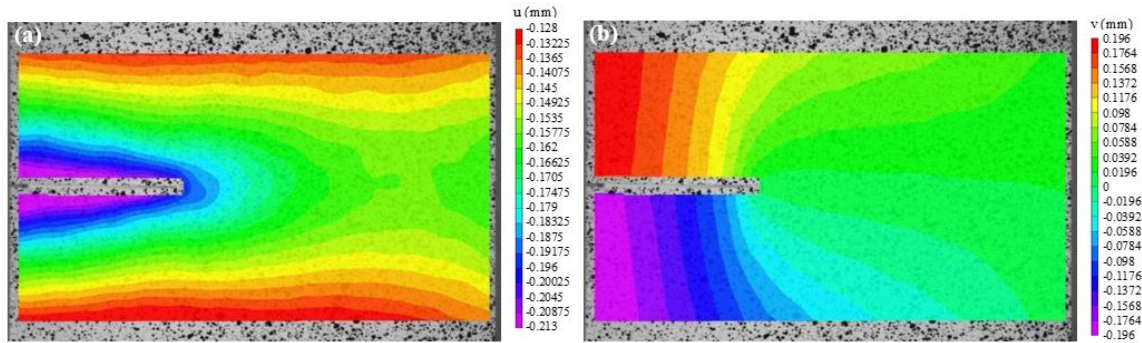


Figure 3.8 Full field displacement distributions obtained from DIC analysis for the pre-loaded  $\beta = 0^\circ$  specimen, (a) horizontal and (b) vertical displacement components.

Table 3.3- Pre-loaded stress intensity factors as function of fiber orientation angle.

Fiber orientation ( $\beta$ )	Stress intensity factor, $K_I$ (MPa.m <sup>0.5</sup> )	
	1750 N pre-load	3500 N pre-load
0°	10.03	20.03
45°	9.94	16.16

### 3.5.3 DYNAMIC STRESS INTENSITY FACTOR AND CRACK VELOCITY

The crack tip velocity during crack propagation was obtained by carefully tracking the crack tip position. This variation of crack tip location as a function of time for different specimens has been displayed in Figure 3.9(a). After extracting the positions of the moving crack tip, the changes in crack tip position as a function of time were used to estimate the crack tip velocity by differentiating the linear curve fitted into the crack tip displacement-time curve. The crack tip velocity as a function of fiber orientation angle for two different pre-loads is shown in Figure 3.9(b). It is clearly shown that, the crack tip velocity increases continuously as the fiber orientation angle increases from  $0^\circ$  to  $45^\circ$ . Selected images captured at different stages of crack propagation for  $\beta = 0^\circ$  and  $45^\circ$  specimens are also

shown in Figure 3.10. As shown in Figure 3.11, the crack follows the direction of fiber orientation as observed by Tippur [3] in the case of unidirectional fiber reinforced composites. Though the composite considered in this work is made of orthogonally woven reinforcing fibers, crack propagation always takes place in the direction parallel to the fiber orientation for all the fiber orientations investigated.

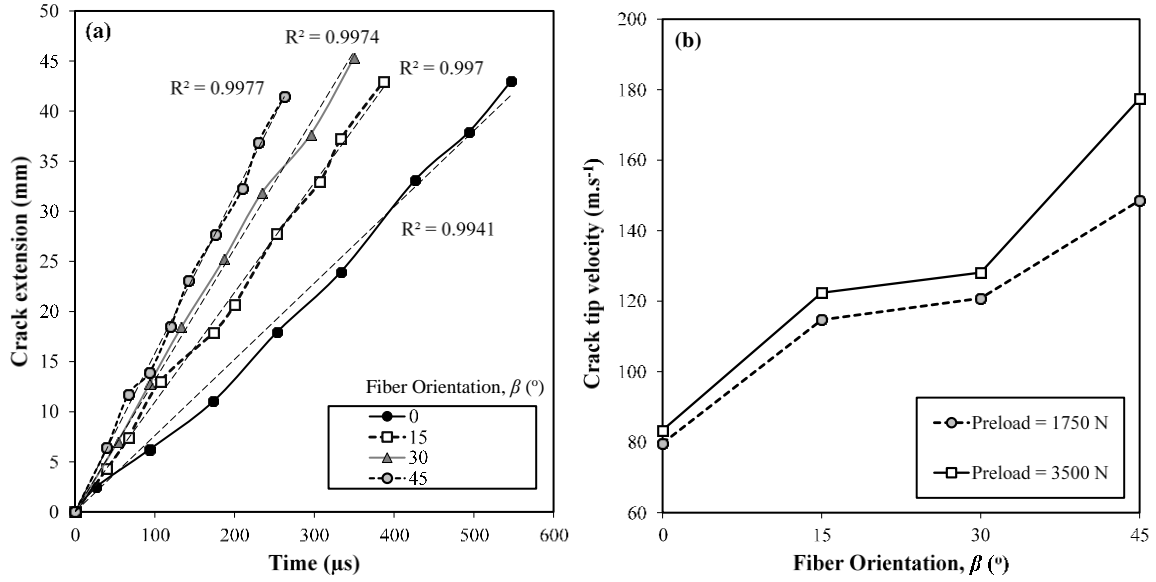


Figure 3.9(a) Crack extension-time plot for a crack subjected to dynamic loading. (Pre-load value is 1750 N and  $t = 0$  indicates the instant of crack initiation). The fitted dashed lines with their corresponding  $R^2$  values are also shown. (b) Crack tip velocity as a function of fiber orientations angle for the specimens subjected to different pre-load values.

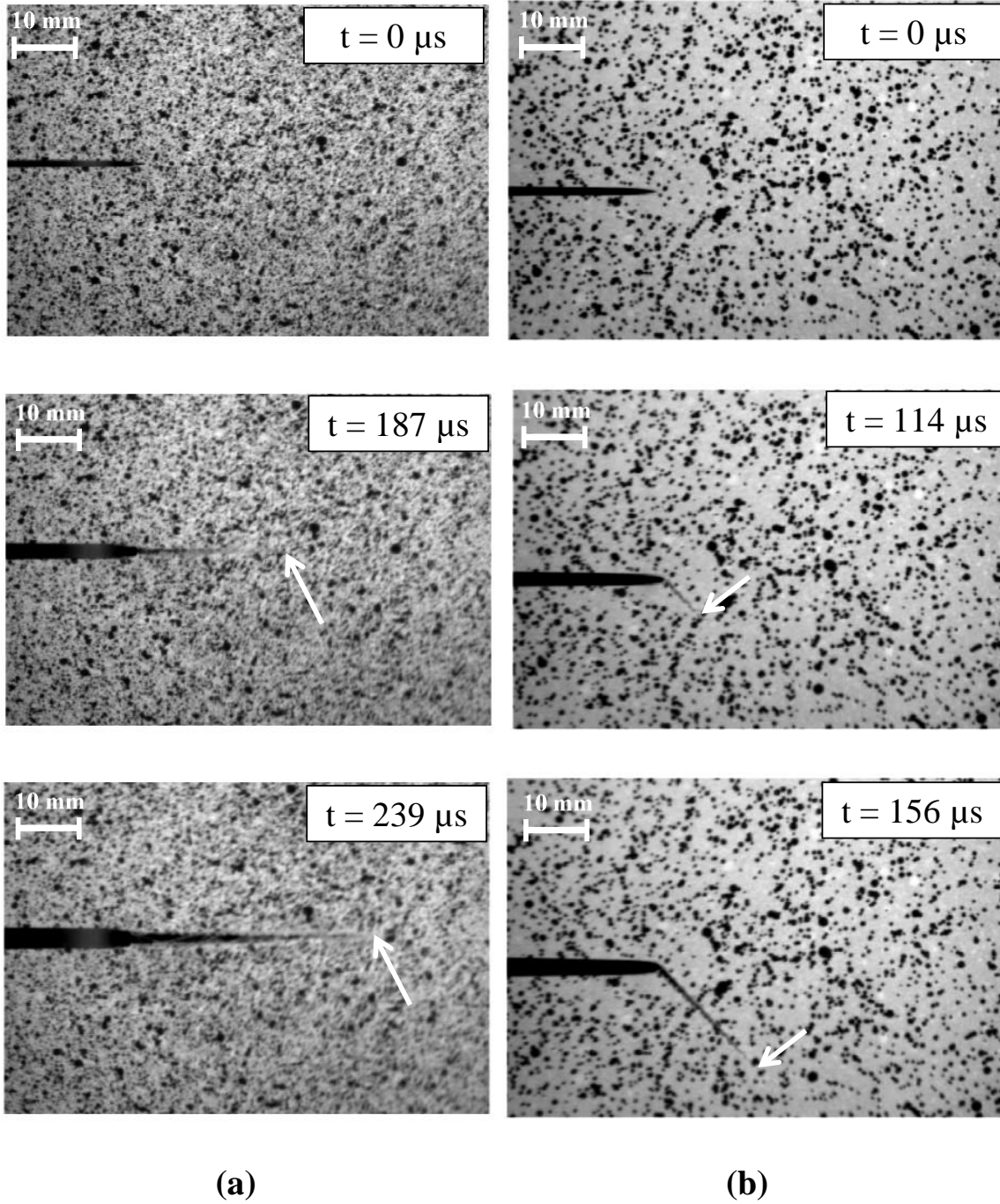


Figure 3.10 Selected DIC images captured at different stages of the crack propagation for (a)  $\beta = 0^\circ$  and (b)  $\beta = 45^\circ$  specimens. Crack tip location has been marked on each image.  $t = 0 \mu s$  indicates the instant of crack initiation.

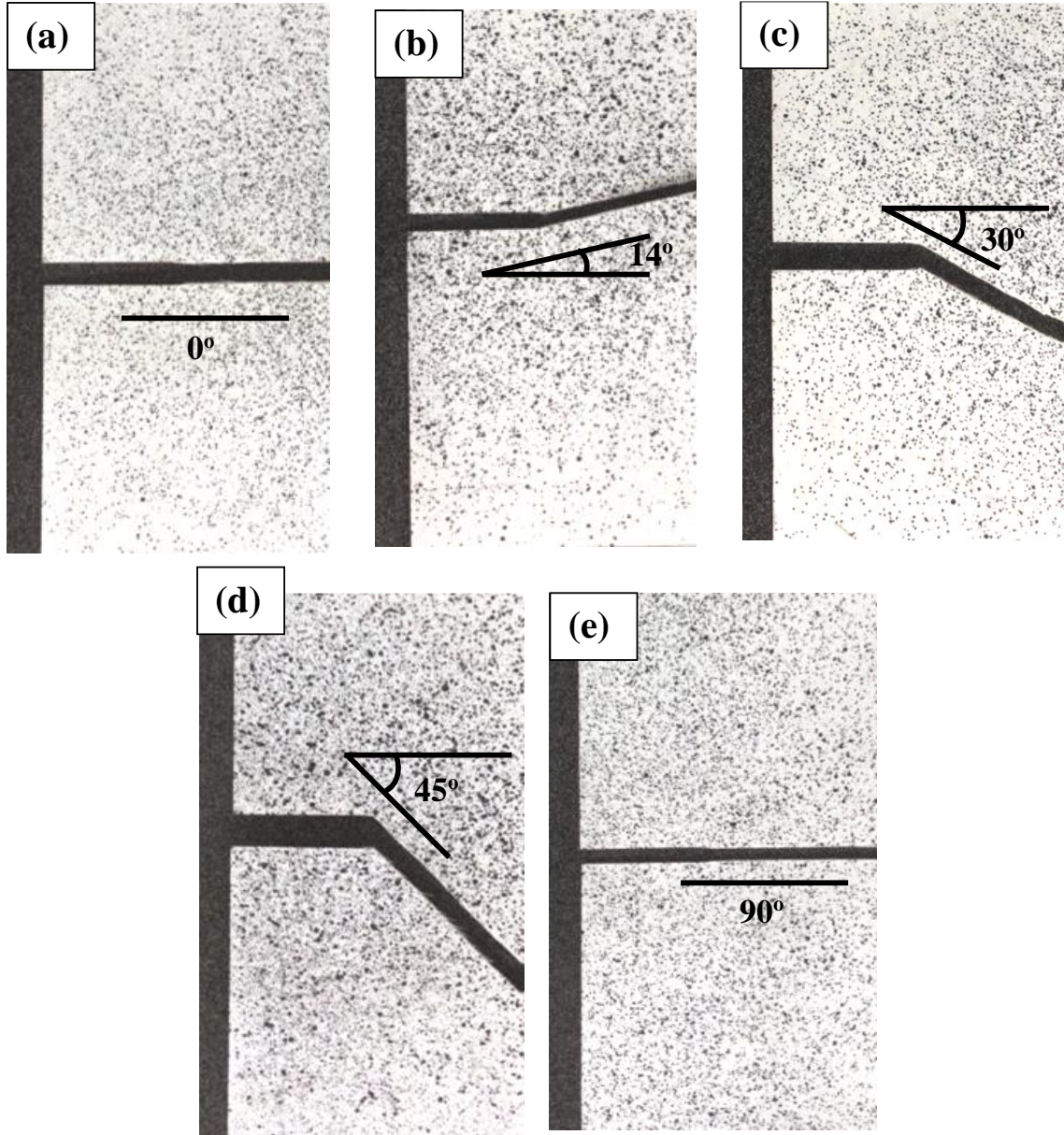


Figure 3.11 Crack direction for specimens with fiber orientation of (a)  $\beta = 0^\circ$  (b)  $\beta = 15^\circ$  (c)  $\beta = 30^\circ$  (d)  $\beta = 0^\circ$  and (e)  $\beta = 90^\circ$ , fractured under dynamic loading with the pre-load magnitude of 3500 N.

As noted previously, the history of vertical displacement and strain components used to detect the crack initiation time. A typical history is shown in Figure 3.12. The sudden drop in the vertical strain component during the loading stage can be used to



accurately determine the moment at which crack growth initiated. In the current work, the crack initiation time has been estimated with an error  $< 5 \mu\text{s}$ .

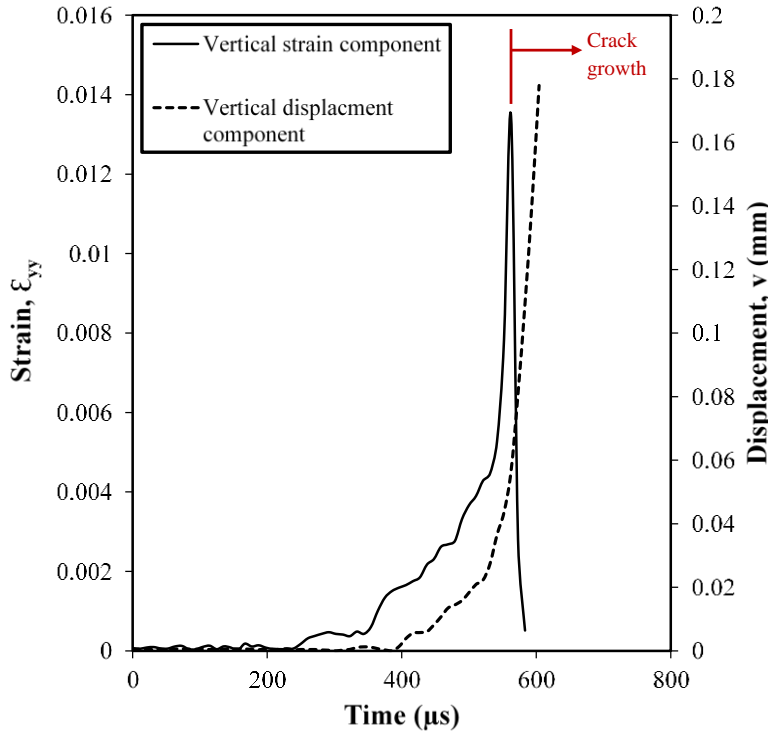


Figure 3.12 History of vertical displacement and strain components before and after crack initiation, for the  $\beta = 0^\circ$  specimen with a 3500 N pre-load magnitude.

Finally, the dynamic stress intensity factor up to the onset of crack growth is calculated using the displacement and strain fields obtained from DIC, following the procedure expressed in Section 3.5. To assure that the fracture mode in this work is indeed Mode-I, the out-of-plane displacement component of each sample was examined. Selected out-of-plane displacement contours both before and after crack initiation for a  $\beta = 45^\circ$  specimen are shown in Figure 3.13. It is observed that the out-of-plane displacement component in the vicinity of the crack tip is symmetric along the crack line, indicating that Mode-III fracture is minimal or non-existent in the case of a pre-stressed specimen subjected to dynamic loading. Since the specimen is very thin, a plane stress condition is



assumed and the effect of out-of-plane bending on the fracture process can be neglected. The out-of-plane displacement,  $w$ , at a location 3 mm ahead of the original crack tip for some selected specimens is listed in Table 3.4. The maximum out-of-plane displacement decreases by approximately 20% with the increase in applied pre-load from 1750 N to 3500 N. It is noted that the stereovision's depth of field in our studies is greater than the maximum out-of-plane displacement achieved by the specimen. Thus, the images remain in focus during the entirety of the experiment and the accuracy of the full-field displacement measurements obtained from digital image correlation is not affected by defocus.

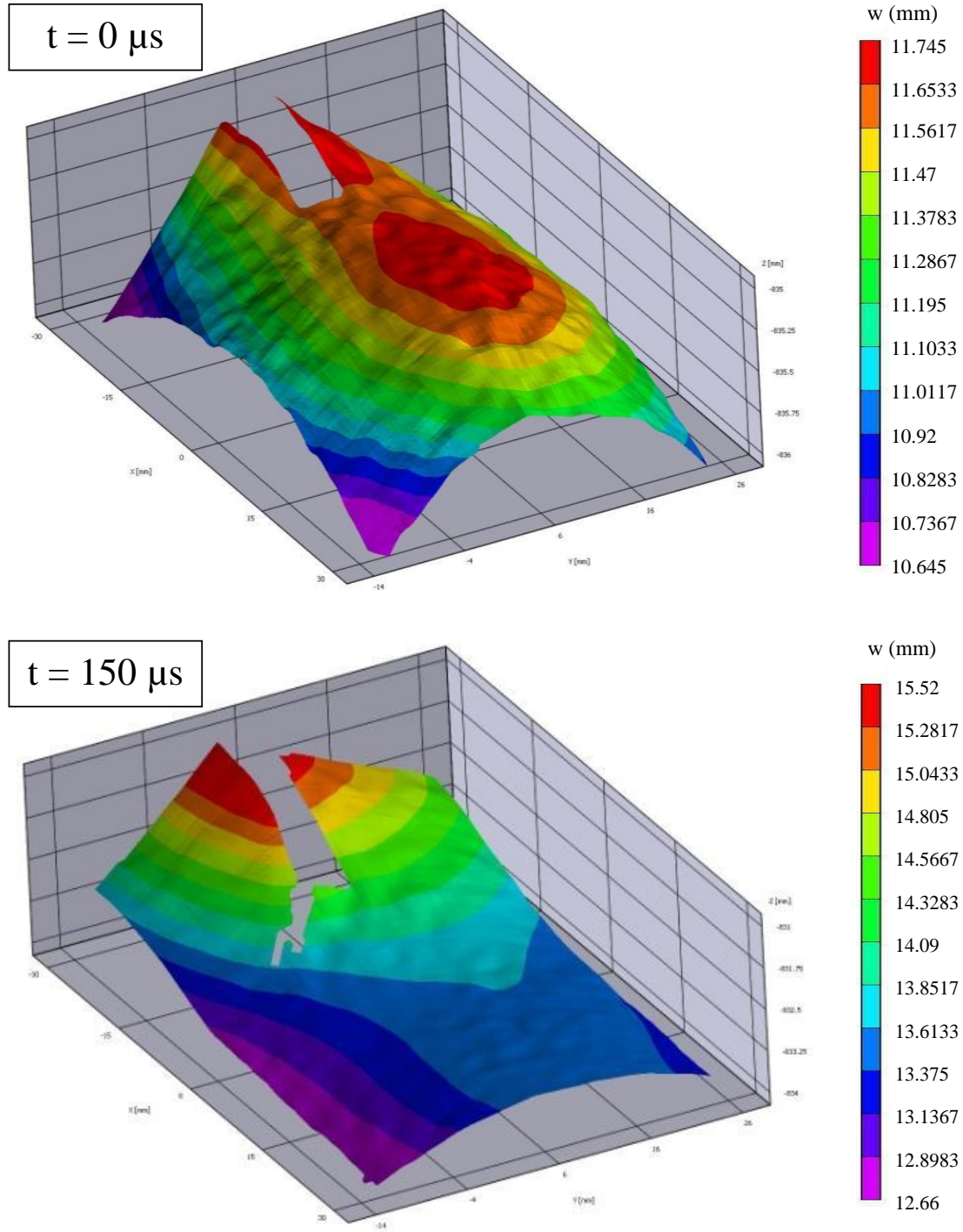


Figure 3.13 3D contour of the out-of-plane displacement component,  $w$ , before and after crack initiation for  $\beta = 45^\circ$  specimen, exposed to dynamic loading with a pre-load magnitude of 3500 N. Note that here  $t = 0 \mu\text{s}$  indicates the onset of crack propagation.

Table 3.4- Maximum out-of-plane displacement,  $w$ , at a location 3 mm ahead of the crack tip just before crack initiation

Fiber orientation ( $\beta$ )	Out-of-plane displacement, $w$ (mm)	
	1750 N pre-load	3500 N pre-load
0°	12.233	9.975
45°	13.639	11.630

Selected strain and displacement contours for the  $\beta = 0^\circ$  specimen during the time prior to crack initiation are depicted in Figure 3.14. The evolution of  $K_I$  up to the onset of crack growth was calculated using both the displacement and strain fields obtained from DIC. This variation of stress intensity factor as a function of time for a specimen exposed to a 3500 N preload is shown in Figure 3.15. The trend exhibited by the evolution of  $K_{ID}$  is irregular, especially during the early stages. This is believed to be characteristic of the material, and unrelated to variations in the loading pulse. As can be seen in a typical pressure profile obtained at the muzzle of the shock tube, shown in Figure 3, the loading pulse is nearly constant for almost 3 milliseconds. The duration of the experiment, from the beginning of loading till crack initiation, is about 800  $\mu$ s and lies in the middle of this constant region. The irregularities could be associated with micro-cracking and other local failure phenomena, which are not considered in this work.

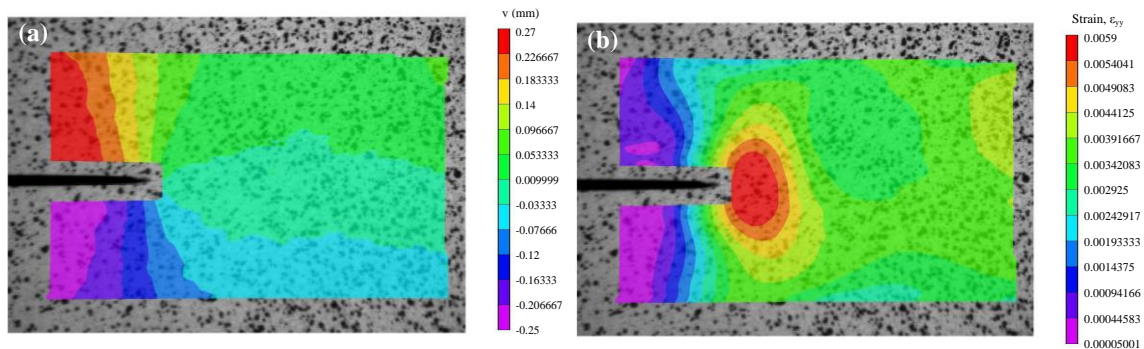


Figure 3.14 Contours of (a) vertical displacement component,  $v$  and (b) vertical strain component,  $\epsilon_{yy}$ , at the moment of crack initiation for the  $\beta = 0^\circ$  specimen subjected to shock loading. The pre-load magnitude applied on the specimen is 3500 N

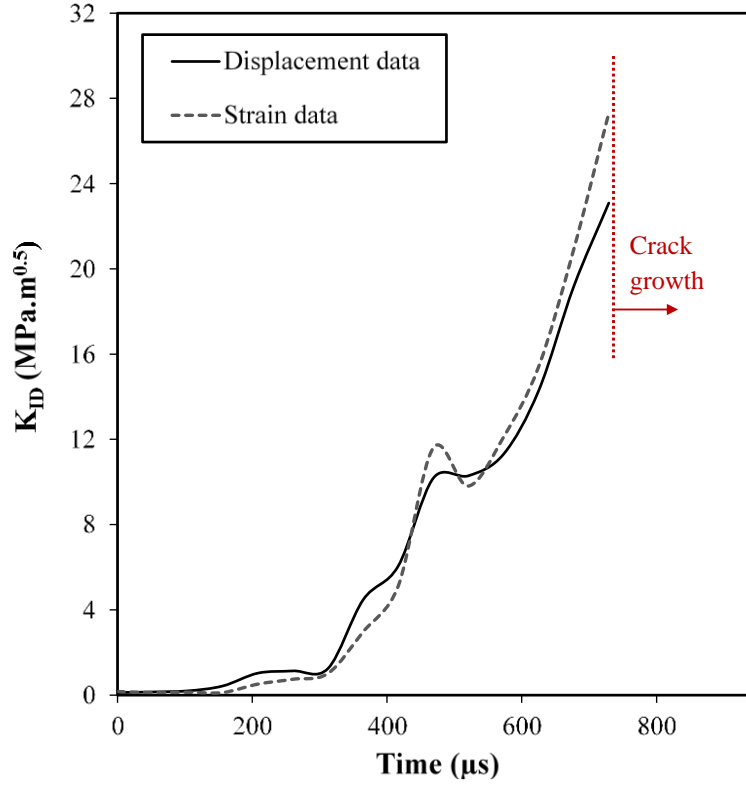


Figure 3.15 Evolution of dynamic  $K_I$  value up to the crack initiation, calculated based on displacement as well as strain data for the  $\beta = 0^\circ$  specimen subjected to dynamic loading with a pre-load magnitude of 3500 N

The dynamic stress intensity factor at the onset of crack initiation for pre-stressed specimens as a function of specimen fiber orientation and pre-load magnitude is shown in Figure 3.16. It is observed that the stress intensity factor decreases as the angle of fiber orientation increases from  $0^\circ$  to  $45^\circ$ . Additionally, the dynamic stress intensity factor decreases consistently as the pre-load increases. To provide a clear comparison between the values of quasi-static and dynamic stress intensity factors obtained in this work, the effective dynamic  $K_I$  value was estimated as the summation of  $K_I$  values calculated from the pre-loading and shock loading stages, as

$$K_{ID}^{eff} = K_I^{preload} + K_I^{shock} \quad (3.8)$$

where  $K_{ID}^{eff}$  is the effective dynamic stress intensity factor,  $K_I^{preload}$  is the pre-load stress intensity factor, and  $K_I^{shock}$  is the stress intensity factor obtained from the shock loading experiment. The values calculated for  $K_{ID}^{eff}$  are listed in Table 3.5. Comparing these values with those obtained from the quasi-static loading condition, dynamic loading resulted in an approximate increase of 15% for the  $\beta = 0^\circ$  specimen, and 25% for the  $\beta = 45^\circ$  specimen. An increased value of dynamic stress intensity factor when compared to the quasi-static value was also reported in [3], and was attributed to the degree of bridging present during quasi-static and dynamic loading conditions.

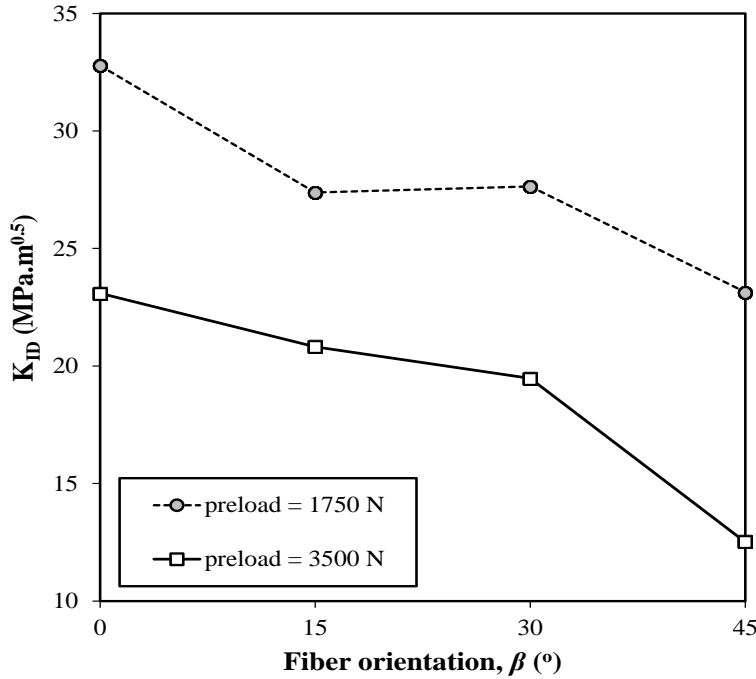


Figure 3.16 Dynamic stress intensity factor,  $K_{ID}$ , obtained for different specimens subjected to different pre-load values.

Table 3.5 Effective dynamic stress intensity factor,  $K_{ID}^{eff}$ .

Fiber orientation ( $\beta$ )	effective dynamic stress intensity factor, $K_{ID}^{eff}$ (MPa.m <sup>0.5</sup> )	
	1750 N pre-load	3500 N pre-load
0°	42.78	43.14
45°	33.03	28.73

Regarding the effect of preload on the critical dynamic stress intensity factor, when the fibers are along the primary loading direction ( $\theta = 0^\circ$ ), the preload has negligible effect. However, when the fibers are oriented at  $\theta = 45^\circ$  sample, the effect of preload is to reduce  $K_{ID}^{eff}$ . These experimental results can be understood by noting that the material is an orthogonally woven composite. Thus, growth of a through-thickness crack requires that the woven fibers separate. When the fibers are in the principal loading direction and are the primary loading carrying members, the preload increases the tensile loading in these fibers and hence increases the initial stress intensity value. When the dynamic loading process initiates, the dynamic component of the stress intensity factor is smaller for the larger preload. If one assumes that the glass fiber fracture process is the same for our experiments (though the critical values may be rate dependent), then the fibers would fail when the conditions at the crack tip reach the same critical dynamic stress intensity factor for both preload conditions since they were subjected to the same dynamic loading conditions.

In the case of off-axis specimen ( $45^\circ$ ), it is less clear how the critical effective stress intensity factor evolves with increasing preload. One plausible explanation deals with the role of the matrix in the fracture process. Since the fibers are off-axis, the matrix would initially take much of the load. However, as the loading process progress, the fibers begin to share the load. The application of preload in the  $45^\circ$  specimen would stretch and rotate the fibers towards the loading direction and makes the matrix less involved in the fracture resistance process. Due to this, the effective stress intensity factor in the case of  $45^\circ$  specimen would tend to decrease as the preload increases. In this regard, it is noted that a similar trend was observed for the stress-strain behavior of a similar material at different fiber orientation angles [11, 22].

Finally, to provide additional insight regarding the effect of loading rate, variation of  $dK_I/dt$ , i.e. the time derivative of the stress intensity factor in dynamic and quasi-static conditions, was examined. The evolution of  $dK_I/dt$  was plotted with respect to  $K_I$  for a specimen having  $\beta = 0^\circ$  as shown in Figure 3.17. The higher rate observed in the evolution of the stress intensity factor in the dynamic case along with strain rate sensitivity of the material could be taken as the main factor resulting in an increase in SIF during dynamic loading condition.

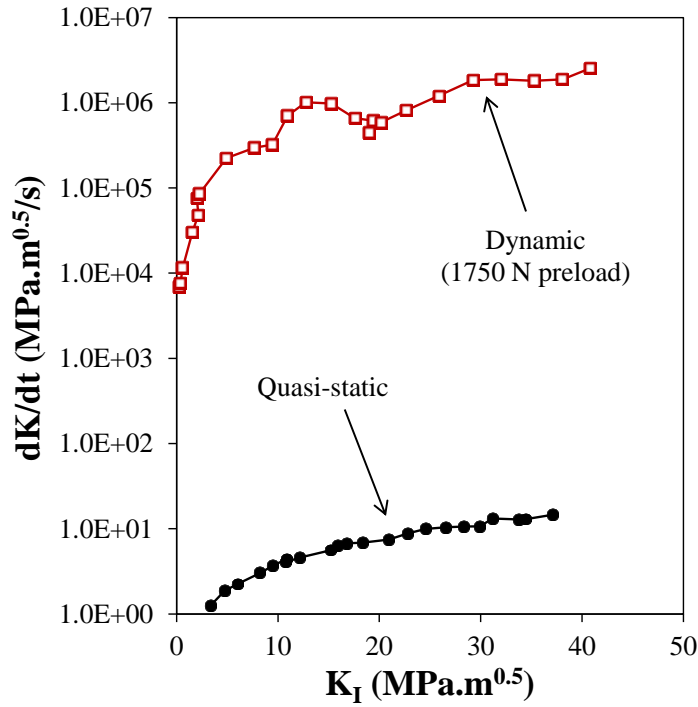


Figure 3.17 Variation of the rate of change of stress intensity factor ( $dK/dt$ ) up to the crack initiation,  $\beta = 0^\circ$  specimen.

### 3.6 CONCLUSIONS

The fracture response of a pre-stressed orthogonally woven glass-fiber reinforced composite was investigated using a shock tube apparatus. The full-field displacement and strains were obtained using 3D digital image correlation, and the fracture parameters were

extracted using an over-deterministic approach. It was demonstrated that the shock apparatus can be used to generate Mode-I dynamic fracture loading on pre-stressed specimens. Furthermore, the full field 3D digital image correlation method can be used to extract displacement components at these high rates of loading. Based on the experiment the following points are observed;

- The crack tip velocity increases as the reinforcing fiber angle increases from  $0^\circ$  to  $45^\circ$ .
- The magnitude of the applied pre-load also significantly affects the crack tip velocity, increases with the magnitude.
- The dynamic stress intensity factor decreases as the reinforcing fiber angle increases from  $0^\circ$  to  $45^\circ$ .
- The material has some strain rate sensitivity for the rates that were applied, with the crack initiation stress intensity factor being higher for dynamic loading when compared to the quasi-static loading.
- The magnitude of the applied preload has negligible effect on the effective stress intensity factor for  $0^\circ$  fiber orientation, whereas the preload decreases the effective stress intensity factor for  $45^\circ$  fiber orientation.



## LIST OF REFERENCES

- [1] Lambros J, Rosakis AJ. Dynamic crack initiation and growth in thick unidirectional graphite/epoxy plates. *Compos Sci Technol* 1997; 57: 55-65.
- [2] Compston P, Jar PYB, Davies P. Matrix effect on the static and dynamic interlaminar fracture toughness of glass-fiber marine composites. *Compos Part B-Eng* 1998; 29B: 505-16.
- [3] Lee D, Tippur H, Kirugulige M. Experimental study of dynamic crack growth in unidirectional graphite/epoxy composites using digital image correlation method and high-speed photography. *J Compos Mater* 2009; 43: 2081-2108.
- [4] Sun CT, Han C. A method for testing interlaminar dynamic fracture toughness of polymeric composites. *Compos Part B-Eng* 2004; 35B: 647-55.
- [5] Naik NK, Asmelash A, Kavala VR, Veerajulu C. Interlaminar shear properties of polymer matrix composites: strain rate effect. *Mech Mater* 2007; 39: 1043-52.
- [6] Lee D, : Tippur H, Bogert P. Quasi-static and dynamic fracture of graphite/epoxy composites. An optical study of loading-rate effects. *Compos Part B-Eng* 2010; 41B: 462-74.
- [7] Shivakumar Gouda PS, Kudar SK, Prabhuswamy S, Jawali D. Fracture toughness of glass-carbon (0/90)s fiber reinforced polymer composite – an experimental and numerical study. *J Min Mater Char Eng* 2011; 10: 671-82.
- [8] Kidane, A. Shukla A. Quasi-Static and Dynamic Fracture Initiation Toughness of Ti/TiB Layered Functionally Graded Material under Thermo-Mechanical Loading. *Eng Fract Mech* 2010; 77: 479-91.
- [9] Kidane, A. On the failure and fracture of polymer foam containing discontinuities, *ISRN Materials Science*, 2013, 1-9, 408596, 2013.
- [10] Dyer SR, Lassila LVJ, Jokinen M, Vallittu PK. Effect of fiber position and orientation on fracture load of fiber-reinforced composite. *Dent Mater* 2004; 20: 947-55.
- [11] Koohbor B, Mallon S, Kidane A, Sutton MA. A DIC-based study of in-plane mechanical response and fracture of orthotropic carbon fiber reinforced composite. *Compos Part B* 2014; 66: 388–99

- [12] Shukla A, Agarwal BD, Bhushan B. Determination of stress intensity factor in orthotropic composite materials using strain gages. *Eng Fract Mech* 1989; 32: 469-77.
- [13] Khanna SK, Shukla A. On the use of strain gages in dynamic fracture mechanics. *Eng Fract Mech* 1995; 51: 933-48.
- [14] Khanna SK, Shukla A. Development of stress field equations and determination of stress intensity factor during dynamic fracture of orthotropic composite materials. *Eng Fract Mech* 1994; 47: 345-59.
- [15] Kokaly MT, Lee J, Kobayashi AS. Moire interferometry for dynamic fracture study. *Opt Lasers Eng* 2003; 40: 231-247.
- [16] Sutton MA, Mingqi C, Peters WH, Chao YJ, McNeill SR. Application of an optimized digital correlation method to planar deformation analysis. *Image Vision Comput* 1986; 4: 143-50.
- [17] McNeil SR, Peters WH, Sutton MA. Estimation of stress intensity factor by digital image correlation. *Eng Fract Mech* 1987; 28: 101-12.
- [18] Chu TC, Ranson WF, Sutton MA, Peters WH. Application of digital image correlation technique to experimental mechanics. *Exp Mech* 1985; 25: 232-45.
- [19] Luo PF, Chao YJ, Sutton MA, Peters WH. Accurate measurement of three-dimensional deformations in deformable and rigid bodies using computer vision. *Exp Mech* 1993; 33: 123-133.
- [20] Helm JD, McNeill SR, Sutton MA. Improved three-dimensional image correlation for surface displacement measurement. *Opt Eng* 1996; 35: 1911-1920.
- [21] Sutton MA, Cheng CS, Zavattieri P, Yan J, Deng X. Three-dimensional digital image correlation to quantify deformation and crack-opening displacement in ductile aluminum under mixed-mode I/III loading. *Opt Eng* 2006; 46: 1-17.
- [22] Pollock P, Yu L, Sutton MA, Guo S, Majumdar P, Gresil M. Full field measurements for determining orthotropic elastic parameters of woven glass-epoxy composites using off-axis tensile specimens. *Exp Tech* 2012;
- [23] Fernandez-Canteli A, Arguelles A, Vina J, Ramulu M, Kobayashi AS. Dynamic fracture toughness measurements in composites by instrumented Charpy testing: influence of aging. *Compos Sci Technol* 2002; 62: 1315-25.
- [24] Wosu SN, Hui D, Dutta PK. Dynamic mixed-mode I/II delamination fracture and energy release rate of unidirectional graphite/epoxy composites. *Eng Fract Mech* 2005; 72: 1531-58.

- [25] Heimbs S, Heller S, Middendorf P, Hahnel F, Weisse J. Low velocity impact on CRFP plates with compressive preload: test and modeling. *Int J Impact Eng* 2009; 36: 1182-93.
- [26] <http://www.norplex-micarta.com> .
- [27] LeBlanc J, Shukla A, Rousseau C, Bogdanovich A Shock loading of three dimensional woven composite materials. *Compos Struct* 2007; 79: 344–55.
- [28] <http://www.correlatedsolutions.com> .
- [29] Barker DB, Sanford RJ, Chona R. Determining  $K_I$  and related stress-field parameters from displacement fields. *Exp Mech* 1985; 25: 399-407.
- [30] Yoneyama S, Morimoto Y, Takashi M. Automatic evaluation of mixed-mode stress intensity factors utilizing digital image correlation. *Strain* 2006; 42: 21-9.
- [31] Yates JR, Zanganeh M, Tai YH. Quantifying crack tip displacement fields with DIC. *Eng Fract Mech* 2010; 77: 2063-76.
- [32] Berger JR, Dally JW. An overdeterministic approach for measuring  $K_I$  using strain gages. *Exp Mech* 1988; 28: 142-45.
- [33] Kim K, Ye L. Effects of thickness and environmental temperature on fracture behavior of polyetherimide (PEI). *J Mater Sci* 2004; 39: 1267-76.
- [34] Anderson TL (2005) *Fracture mechanics – Fundamentals and applications*, 3rd ed. Taylor & Francis, Florida, pp 360-369.
- [35] Yanase K, Ju JW (2013) Toughening behavior of unidirectional fiber reinforced composites containing a crack-like flaw: Matrix crack without fiber break. *Int J Damage Mech* 22: 336-355.

## CHAPTER 4

### OBSERVATION OF PMDI FOAM SUBJECTED TO SHOCK LOADING

#### 4.1 ABSTRACT

Dynamic material response of polymer foam subjected to shock loading has been investigated, and the effects of density and loading rate have been studied. Cubic specimens 20 and 30 lb/ft<sup>3</sup> nominal densities were subjected to shock loading using a single diaphragm shock tube apparatus. Full field displacements and strain fields are obtained with the use of stereo high speed cameras in conjunction with the 3D digital image correlation technique. Simultaneously, load data is obtained with the use of piezotronic load cells. Material responses of the two different mass densities of polymer foam have been examined, while the effect of loading rate is also examined by comparison with results from quasi-static compression testing. The material response as a function of loading rate was recovered using load cell data and digital image correlation strain fields. Failure mechanisms are observed to differ in specimens of different density. Failure stress is seen to increase significantly with increasing foam density. Both 20 and 30 lb/ft<sup>3</sup> density foams exhibit substantial strain rate dependence, with large increases in stress at failure observed at an elevated strain rate.

#### 4.2 INTRODUCTION

Foam materials are often desirable for engineering applications in which energy absorption is essential due to their ability to facilitate large deformations at a relatively constant stress. As a result, polymeric foam has been utilized extensively in automotive

industry to promote safety in the event of accidents, and also in shipping applications requiring sensitive objects to be protected from impact damage. Many of these uses inherently entail elevated loading rates, such as high speed vehicle crashes or impact on packaged items. Therefore, material properties obtained from quasi-static testing may not be suitable for evaluation of material performance in such situations, as such properties may be highly strain rate dependent.

Substantial work has been established detailing the effect of loading rate and density on fracture toughness in polymeric foams. Experimental work by Kabir et al. [1] examining the effect of loading rate on the fracture toughness of PVC foam indicated that the dynamic fracture toughness was  $\approx 2.75 \text{ MPa m}^{0.5}$ , nearly four times the value observed in quasi-static testing. Marsavina et al. [2] used quasi-static and instrumented impact tests on polyurethane foams of varying density, also observing increased fracture toughness under dynamic conditions. The digital image correlation technique has proven robust for use on polymer foams, as shown in the quasi-static fracture work of Jin et al. [3]. Tensile and fracture failure in foam containing discontinuities was examined experimentally by Kidane et al. [4, 5] with the use of DIC. Dynamic compaction of foam has been considered in a numerical analysis by Nian et al. [6] which concludes that energy absorption in foam materials is greater than in similar quasi-static loading experiments.

The present work attempts to characterize the effect of both elevated strain rate and also density on the compressive behavior of PMDI foams, utilizing high-speed imaging and 3D digital image correlation. Additionally, direct measurements of specimen loads are obtained using piezotronic load cells.

#### 4.3 MATERIAL AND SPECIMEN GEOMETRY

In this work, rigid closed-cell PMDI (polymeric methylene diphenyl diisocyanate) foams with nominal densities of 20 and 30 lb/ft<sup>3</sup> (or 320 and 480 kg/m<sup>3</sup>, respectively) are subjected to shock loading. Both the higher and lower density foams were fashioned into 25.4 mm cubic specimens from cylindrical billets, shown in Fig. 4.1a, with the use of a milling machine. A slight difference in color is apparent between the two densities, with both exhibiting smooth uniform surfaces. The specimen geometry is also shown below in Figure 4.1a.

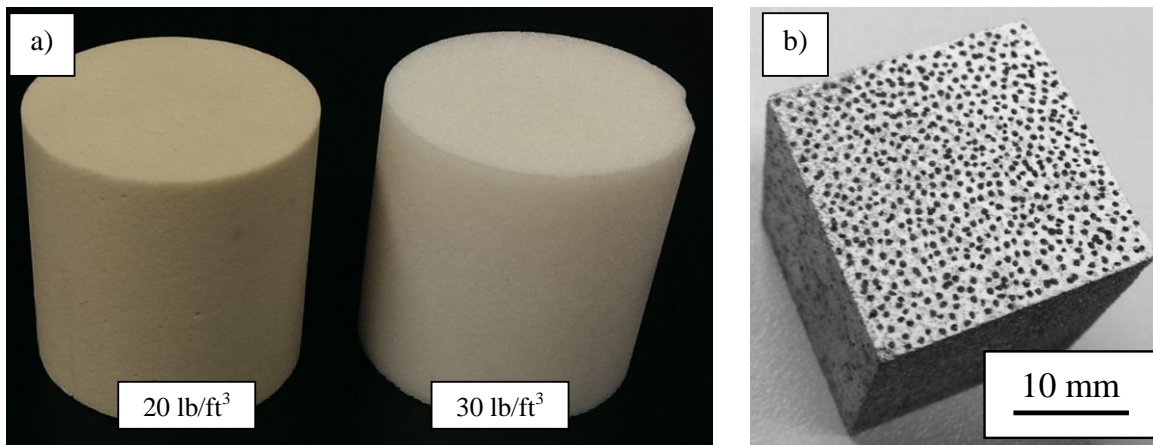


Figure 4.1 Raw foam billets (a) and typical specimen (b) with speckled surface used in the full field observations.

Displacement and strain data was extracted from images of the specimen captured using a stereo camera arrangement in both quasi-static and dynamic testing. This data was extracted with the use 3D digital image correlation, facilitated by commercial software Vic-3D. This technique necessitates a speckle pattern to be applied to one surface of each specimen. The higher density foam exhibited a very white surface hue, allowing black speckles to be applied directly to the foam surface. The lower density foam exhibited a substantially darker, more yellow hue; requiring a thin layer of white paint to be applied before specking to maintain an adequate contrast ratio in the speckle pattern. Due to the relatively small scale of the specimen and the high magnification used to observe specimen

behavior, speckles were applied to each surface by hand using a fine point ink marker. This process of speckle application proved to be superior to paint, providing small, well defined speckles; thus resulting in an excellent contrast exhibited by the pattern. A typical speckle pattern is shown in Figure 4.1-b.

#### 4.4 EXPERIMENTAL

For reference, quasi-static compression testing was done on both the 20 lb/ft<sup>3</sup> and 30 lb/ft<sup>3</sup> specimens using an MTS 458 load frame fitted with compression platens. Loading was applied monotonically at a rate of 0.001 in/s or approximately 1.5 mm/min until failure using the aforementioned specimen geometry with ample lubricant applied between the specimen and platen. During testing, stereo images were acquired every second using 5 megapixel cameras. Specimen displacement and strain fields were extracted from these images, with the use of 3D digital image correlation, facilitated by commercial software Vic-3D. Load and displacement data were collected simultaneously using a load cell and extensometer, respectively. The arrangement of cameras, specimen, and load frame is depicted in Figure 4.2.

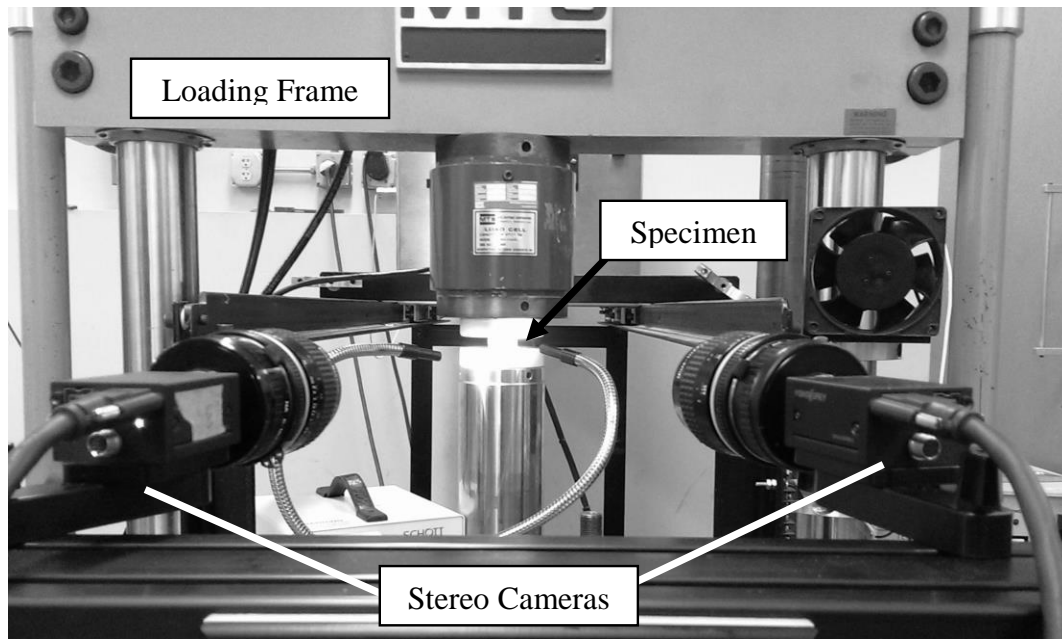


Figure 4.2 Quasi-static experimental setup

A shock tube apparatus was used to facilitate dynamic testing. As described in Chapter 2.1, the shock tube consists of a tube having one closed end opposite the specimen, separated by a Mylar diaphragm into a 2 m driver section and a 6 m driven section. The driver section, existing at the end opposite the specimen, is pressurized with helium until the Mylar diaphragm ruptures. After the diaphragm has burst, the helium expands rapidly from the high pressure driver section into the lower pressure driven section towards the specimen. In these studies, the converging nozzle section described in Ch. 2 was used to increase shock velocity. The velocity and magnitude of the pressure wave produced by the shock tube can be manipulated by increasing or decreasing the number of Mylar sheets forming the diaphragm that separates the driver and driven sections of the tube. The shock tube setup for these experiments is shown in Figure 4.3.



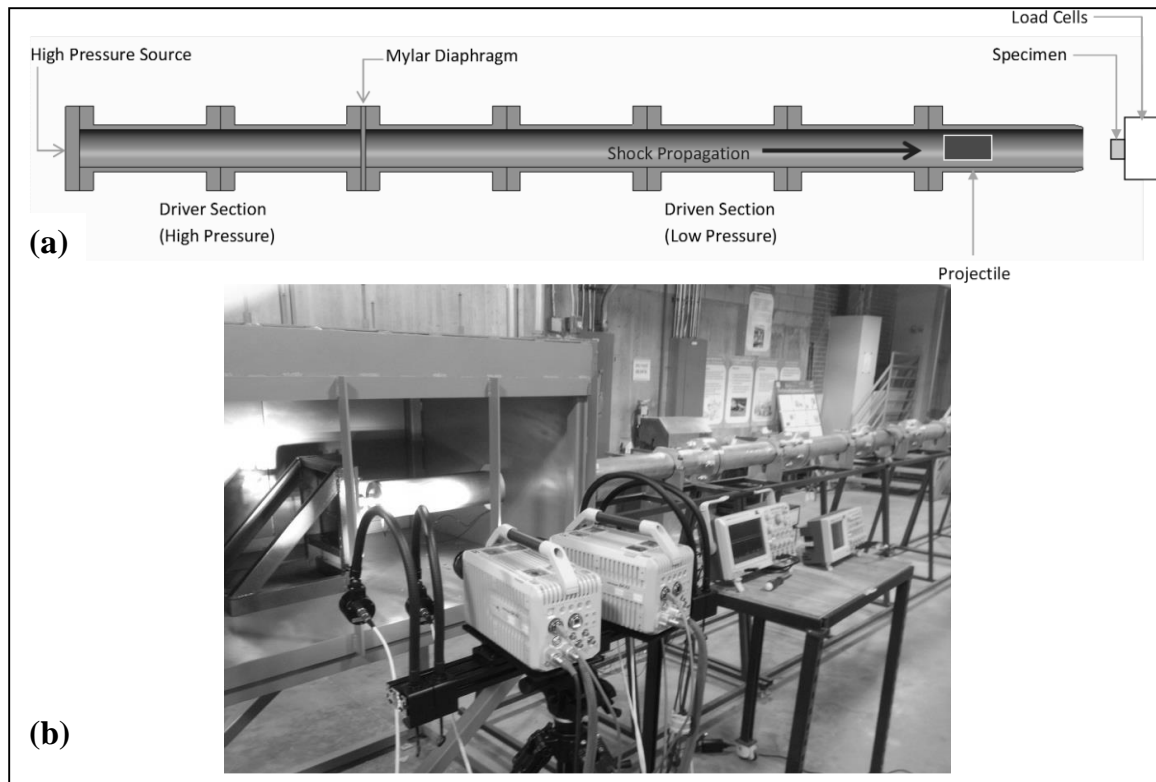


Figure 4.3 CAD drawing (a) and actual setup (b) of the shock tube apparatus.

In conjunction with the shock tube, a projectile was utilized to increase energy transfer to the specimen. This projectile was constructed of alloy 7068 aluminum, 72 mm in length and 50 mm in diameter, and hollowed from one end to reduce mass to 170 grams. The projectile is shown in Figure 4.4.

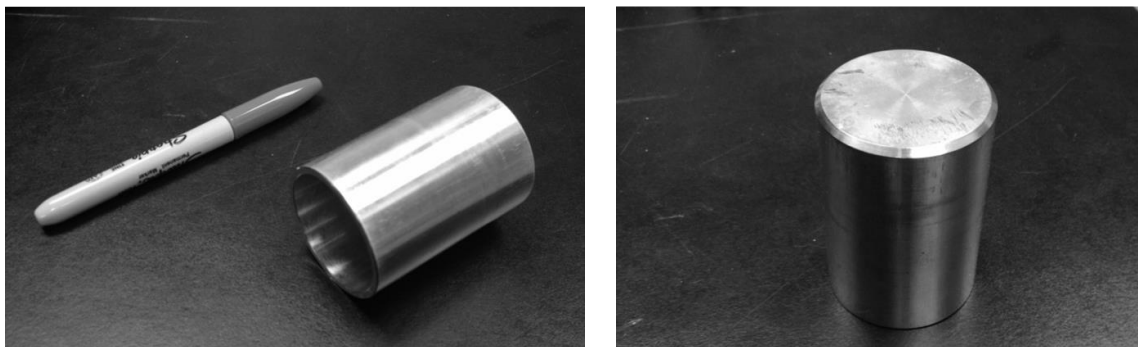


Figure 4.4 The projectile used in the shock tube apparatus to increase energy transfer to the specimen

Specimen load data was observed using a loading fixture incorporating piezotronic load cells placed behind the specimen. The three load cells were arranged in a specially made fixture upon which the specimens were affixed, with lithium grease serving to lubricate and affix the specimen. Use of three load cells, rather than a single cell, proved relevant in that the multiple sensors facilitated examination of the specimen load distribution in addition to the simple acquisition of the specimen load magnitude.

An oscilloscope was used to acquire data from the load cells, and also to trigger data and image acquisition. Load cell data was acquired at a frequency of  $10^6$  Hz with the use of an oscilloscope, which also served to trigger data and image acquisition. Images were acquired using Photron SAX-2 high speed cameras in a stereo configuration at a rate of  $10^5$  fps. Additional LED light sources mounted alongside the cameras, required for high speed image acquisition, were also utilized. The oscilloscope and stereo high speed camera system can also be seen in Figure 3. Dynamic experiments were carried out by first inserting the projectile fully into the 1 m long section of reduced diameter, and then placing a well lubricated specimen onto the test fixture. Only one layer of Mylar was used in the shock tube for all experiments presented here.

#### 4.5 RESULTS AND DISCUSSION

The stress strain plots for both  $20 \text{ lb/ft}^3$  and  $30 \text{ lb/ft}^3$  density specimens under quasi-static testing are shown in Figure 4.5. As shown in Figure 4.5, the lower density foam compressed to nearly 40 % strain without apparent densification. The  $30 \text{ lb/ft}^3$  foam, however, exhibits a prominent densification stage after 25 % strain. Stress levels in the  $20 \text{ lb/ft}^3$  specimen rise only slightly from the plateau stress to reach approximately 11.5 MPa

at failure, while the 30 lb/ft<sup>3</sup> foam experiences substantial densification as the stress increases rapidly to nearly 48 MPa before failure.

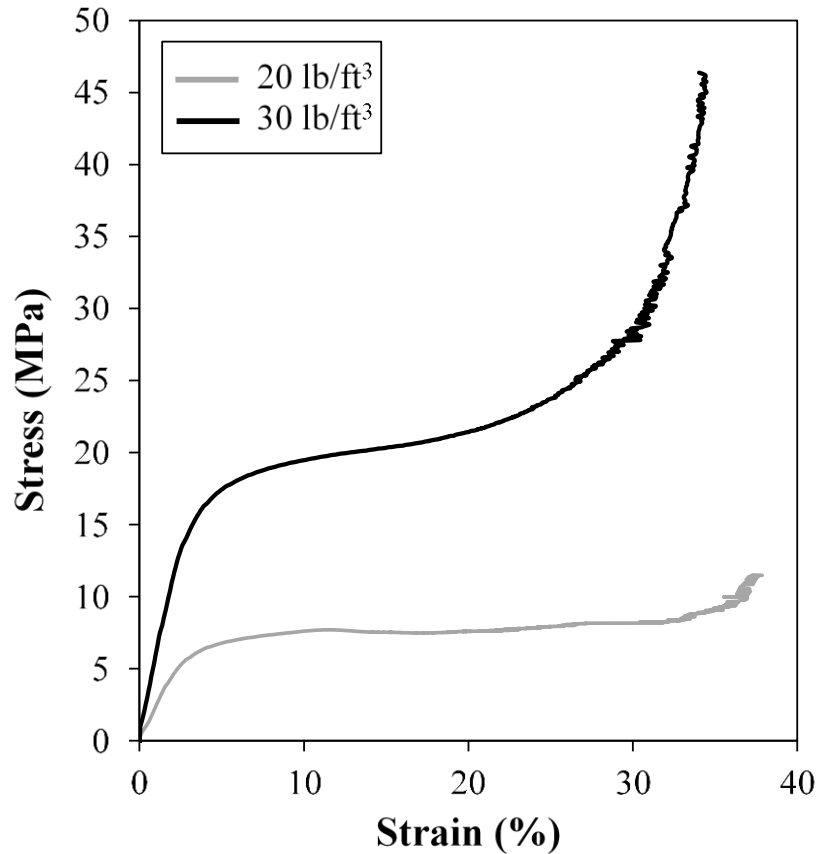


Figure 4.5 Stress-time plot as a function of density under quasi-static loading

In all the dynamic experiments, specimens are seen to disintegrate after being impacted by projectile; only very fine particles remain at the conclusion of the experiment. Load data collected is sinusoidal in form; with duration of 60  $\mu$ s. Specimen failure is evident in the stress vs. time curves; a rapid decline in stress occurs after reaching a maximum.

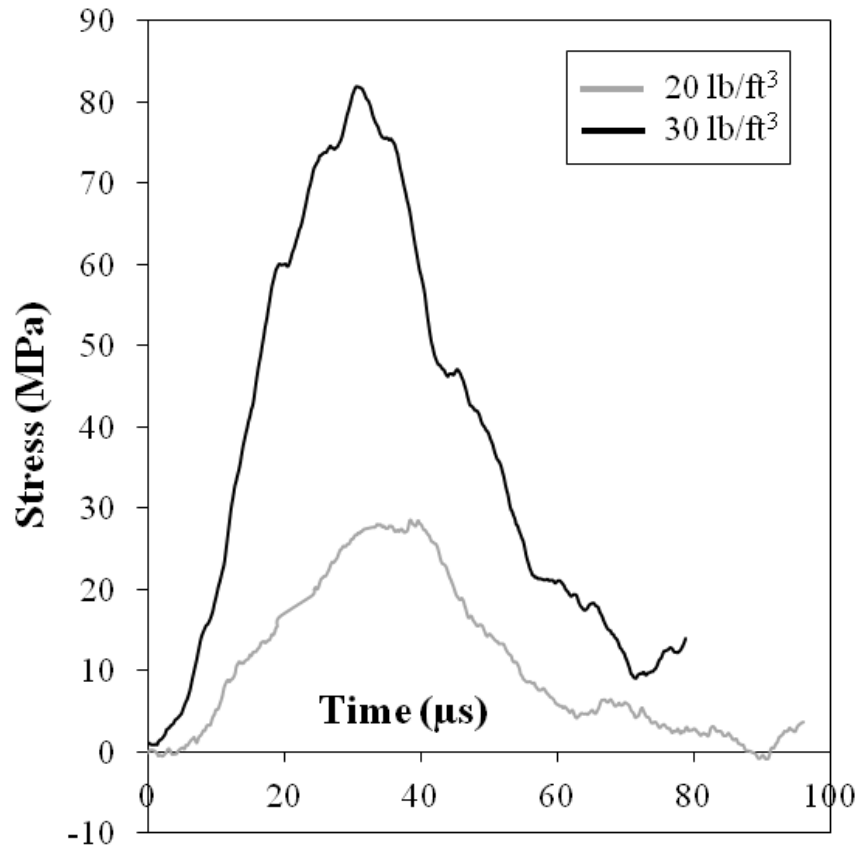


Figure 4.6 Stress vs. time plot for dynamic loading condition.

High speed images of typical specimen deformation during dynamic loading for both 20 and 30 lb/ft<sup>3</sup> foams are shown in Fig. 4.8. Projectile velocity was also extrapolated from these images by observing the projectile position as a function of time, and found to be consistent at 60 m/s. Kinetic energy of the projectile before impact was found to be approximately 300 J. Images were analyzed using VIC-3D to obtain axial strain measurements as a function of time. Typical axial strain fields at different times during the dynamic loading event are shown in Figure 4.8. Using these strain measurements, the strain rate present in the dynamic testing was calculated, as shown in Figure 4.9.

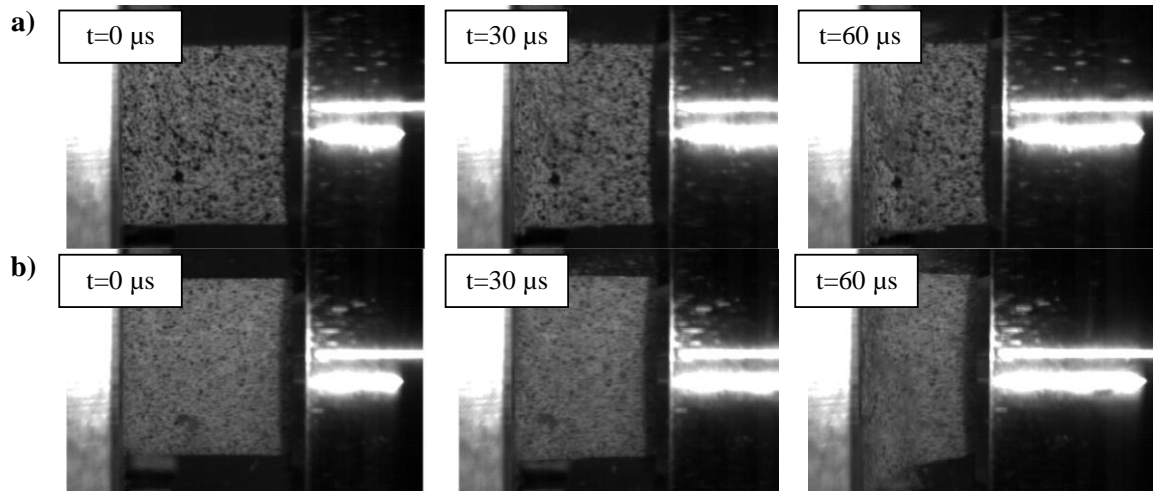


Figure 4.7 The dynamic deformation and failure behavior of 20 lb/ft<sup>3</sup> (a) and 30 lb/ft<sup>3</sup> (b) specimens at different times.

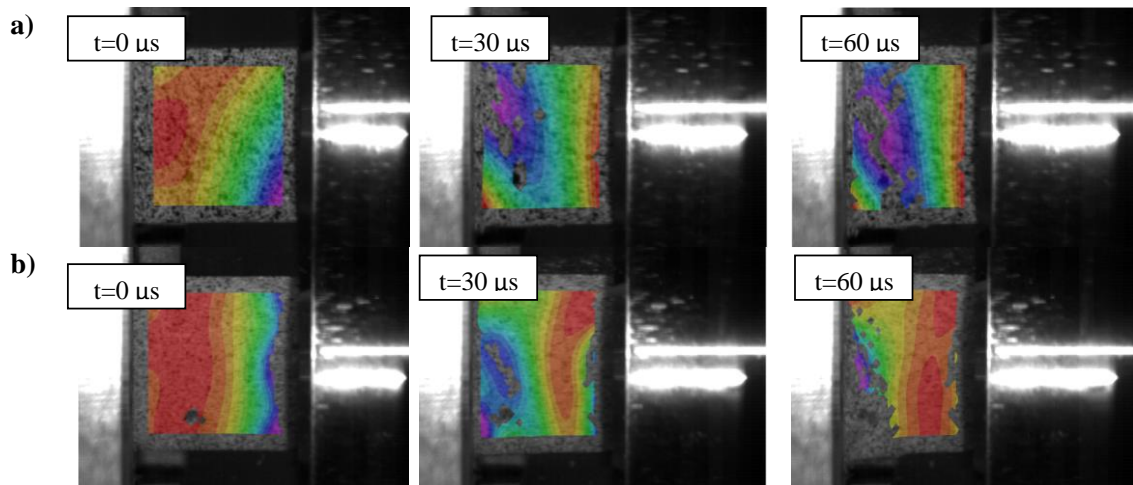


Figure 4.8 Dynamic axial strain contours of 20 lb/ft<sup>3</sup> (a) and 30 lb/ft<sup>3</sup> (b) specimens at different times.

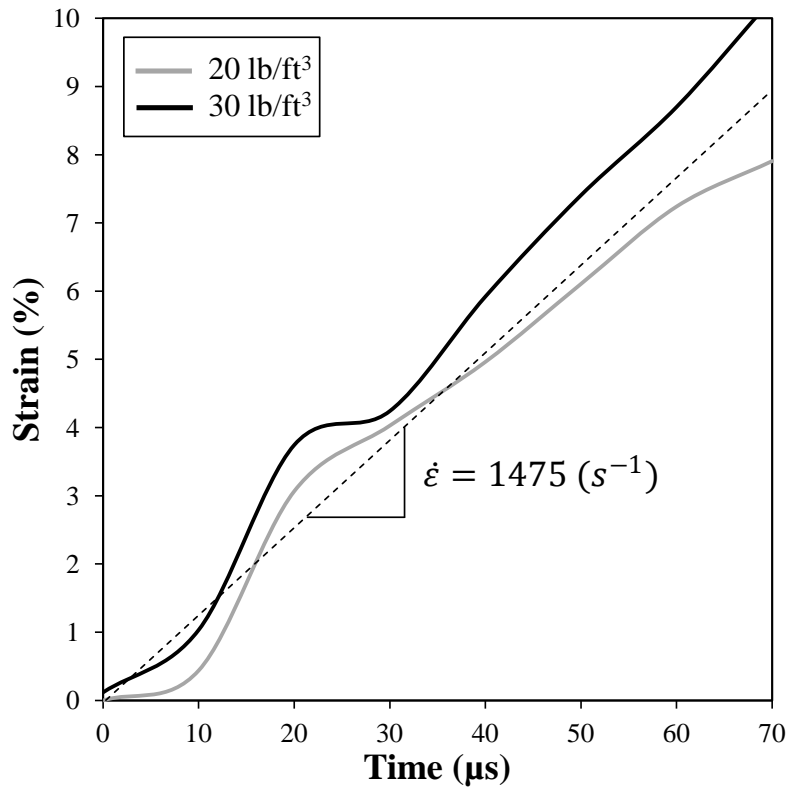


Figure 4.9 Strain histories acquired from dynamic testing.

#### 4.6 CONCLUSIONS

Material testing has been done at a strain rate of approximately  $1600 \text{ s}^{-1}$  with 20 lb/ft<sup>3</sup> and 30 lb/ft<sup>3</sup> polymeric methylene diphenyl diisocyanate foam using a shock tube in conjunction with a projectile, piezotronic load cells, and a stereo high speed camera system. Both materials are found to disintegrate into fine particulates after failure. The stress history of the specimens during dynamic loading was obtained from the load cells, while material deformation was observed using high speed stereo imaging in combination with 3D digital image correlation. For comparative use, quasi-static compression testing was done, also with the utilization of stereo imaging and 3D digital image correlation. The maximum stress achieved in both the 20 lb/ft<sup>3</sup> and 30 lb/ft<sup>3</sup> specimens during dynamic testing are far greater than maximum stresses observed during quasi-static testing. Unlike

quasi-static failure, in the case of dynamic loading the 20 lb/ft<sup>3</sup> specimens appear to fail after initiation of a myriad of small fractures, initiating at 45 degrees to the axis of loading, while the 30 lb/ft<sup>3</sup> specimens appeared to simply pulverize into fine particles.

## LIST OF REFERENCES

- [1] Kabir, M.D. Saha, M.C. Jeelani, S. Tensile and fracture behavior of polymer foams, *Materials Science and Engineering A* 429, 225–235, 2006.
- [2] Marsavina, L. Linul, E. Voiconi, T. Sadowski, T. A comparison between dynamic and static fracture toughness of polyurethane foams. *Polymer Testing* 2013; 32: 73-680.
- [3] Jin, H. Lu, W.Y. Hong, S. Connelly, K. Fracture behavior of polyurethane foams, *Society for Experimental Mechanics*, Springfield MA, 2007.
- [4] Kidane A. On the Failure and Fracture of Polymer Foam Containing Discontinuities. *ISRN Mater Sci* 2013; 2013: 1-9.
- [5] Kidane, A. Ravichandran, G. Failure and Fracture Behavior of Brittle Polymer Foam, *Experimental and Applied Mechanics, Conference Proceedings of the Society for Experimental Mechanics Series*, Volume 6, 91-98, 2011.
- [6] Nian, W. Subramaniam, K. Andreopoulos, Y. Dynamic compaction of foam under blast loading considering fluid-structure interaction effects, *International J Impact Eng* 2007; 50: 29-39.



## CHAPTER 5

### DYNAMIC TORSIONAL EXPERIMENTS ON AA7050T-6571

#### 5.1 ABSTRACT

A TSHB has been implemented to observe strain rate effects in the material response of aluminum alloy 7050T-7651. The material, received in the form of 32 mm thick plates, has been tested in the as-received condition and also in the as friction-stir welded (FSW) condition. Microstructural observations have been made using optical microscopy, revealing a fine, equiaxed structure of small grains in the FSW material state and an irregular structure of elongated and markedly larger grains in the as-received material condition. Quasi-static tensile and high rate torsional testing depict lower yield and flow stresses in the FSW material when compared to the base metal. Testing further demonstrates the presence of appreciable rate dependence in both material states. The present work is also indicative of an increased work hardening rate in the FSW material, while the base metal exhibits only minimal work hardening. The increased propensity for work hardening and decreased mechanical strength in the FSW material is found to be the primary difference between the two material states.

#### 5.2 INTRODUCTION

Aluminum alloys have traditionally been the engineering material of choice in aerospace applications, attributable to their high strength to weight ratio and corrosion resistance [1, 2]. Aluminum alloy 7050 is an aerospace grade of aluminum that incorporates desirable qualities such as high strength, increased resistance to stress corrosion cracking

(SCC), and toughness. The temper studied here is 7050-T7651, which possesses the greatest strength of all aerospace aluminum alloys with good corrosion resistance, while maintaining an average resistance to stress corrosion cracking [3]. This alloy also exhibits minimal quench sensitivity, allowing it to maintain high strength in thicker sections. This makes the alloy desirable in applications requiring thick plate (75 mm to 150 mm) [4], such as fuselage frames, bulkheads, and wing skins. These aerospace components may be vulnerable to impact loading, in the event of a collision with flying debris for example, therefore subjecting the materials to elevated strain rates. In such applications where reliability is critical, an adequate understanding of material behavior at higher strain rates is desirable.

In general, contemporary literature contains minimal information regarding the properties of aluminum alloy 7050. Some investigations regarding micromechanical and fracture response of this material have taken place, mostly utilizing indentation techniques [5, 6]. Han et al. [7] have also worked to study the effect of solution heat treatment on the mechanical characteristics and fracture properties of AA7050. Existing work by Ren et al. [8] considers the effect of orientation with respect to material elongation during the forging process on the tensile and fatigue properties of AA7050. Zheng et al. [9] characterized the effect of large plastic deformation on the microstructure and mechanical response of AA7050. Established work dealing with AA7050 is limited to cases considering quasi-static loading conditions, and is often abstract in nature. Although a vast amount of effort has been devoted to characterize similar, more popular alloys such as AA7075, it would seem that a more thorough understanding of material behavior exhibited by AA7050 would be worthwhile, particularly when considering elevated strain rate conditions.

The demand for a joining process able to produce high strength bonds containing minimal defects in materials difficult to join with conventional fusion processes, such as 7000 series aluminum alloys, has given rise to the friction stir welding (FSW) process [10, 11]. This process is particularly advantageous in the case of thick plate applications, where AA7050 is widely used. Changes in microstructure and hardness as a result of friction-stir welding have been well documented in AA7050 [12]. Tensile strength and hardness in the weld material have also been observed while investigating the effect of submerging the process in water [13]. However, mechanical characteristics of friction-stir welded material at elevated strain rates has received no attention in established work.

The present work attempts to characterize the mechanical behavior of 7050T-7651 aluminum alloy in as-received and as friction-stir welded conditions at effective strain rates from 300/sec to 900/sec with the use of a THSB apparatus. The TSHB has proved to be a robust piece of equipment, having been used successfully to test a wide variety of materials including composites, aluminum, stainless steel, and even the super alloy Inconel at elevated strain rates [14-17]. The torsional variant of the very popular compression Hopkinson bar is favored here, as high strain rate torsional testing of materials has been shown to provide more accurate results compared to similar compressive experiments [18].

### 5.3 THEORY

Consider a system comprised of an incident and transmitter bar, each of diameter  $D$  and shear modulus  $G$ , with a tubular specimen having gage diameter and length  $D_s$  and  $L_s$ , respectively, cemented between the two bars as shown in Figure 5.1.

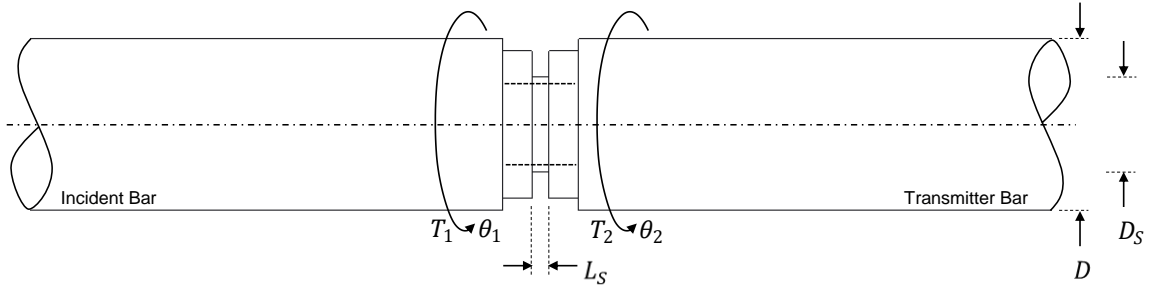


Figure 5.1- Schematic of specimen affixed to incident bar and transmitter bar.

The torsional strain present in the specimen is then:

$$\gamma_s = \frac{D_s}{2L_s} [\theta_1 - \theta_2] \quad (5.1)$$

where  $D_s$  and  $L_s$  are gage mean diameter and length of the specimen, respectively, and the quantities  $\theta_1$  and  $\theta_2$  represent angular rotation of the incident and transmitter bar, respectively. The specimen strain rate can then be expressed as:

$$\dot{\gamma}_s = \frac{D_s}{2L_s} \left[ \frac{\partial \theta_1}{\partial t} - \frac{\partial \theta_2}{\partial t} \right] \quad (5.2)$$

The time derivative of the angular rotation at the specimen interface with the incident bar can then be expressed in terms of shear strains present in the incident bar by Eq. 5.3.

$$\frac{\partial \theta_1}{\partial t} = \frac{2C_s}{D} [\gamma_I(t) - \gamma_R(t)] \quad (5.3)$$

Here,  $C_s$  is the shear wave speed in the bar material. Similarly, the time derivative of the angular rotation at the specimen interface with the transmitter bar is defined in Eq. 5.4.

$$\frac{\partial \theta_2}{\partial t} = \frac{2C_s}{D} [\gamma_T(t)] \quad (5.4)$$

Substituting Eqs. (5.3) and (5.4) into Eq. (5.2), the strain rate present in the specimen can be expressed in terms of elastic strains measured in the incident and transmitter bar as shown in Eq. 5.5 [19].

$$\dot{\gamma}_s(t) = \frac{C_s D_s}{L_s D} [\gamma_I(t) - \gamma_R(t) - \gamma_T(t)] \quad (5.5)$$

Assuming stress equilibrium, it is often customary to make use of the identity in which:

$$\gamma_T(t) = \gamma_I(t) + \gamma_R(t) \quad (5.6)$$

in order to express the strain rate exclusively in terms of the reflected strain pulse  $\gamma_R(t)$ , as:

$$\dot{\gamma}_s(t) = \frac{2C_s D_s}{L_s D} [\gamma_R(t)] \quad (5.7)$$

However, since the perfectly ideal condition of equilibrium considered in Eq. (5.7) is unachievable within the limits of practicality, the present work will consider the strain rate as an average of the time derivatives of rotations at the specimen interface with the incident and transmitter bars, as given in Eq. (5.5). By integrating Eq. (5.5) with respect to time, the specimen strain as a function of time can be expressed as:

$$\gamma_s(t) = \frac{2C_s D_s}{L_s D} \int_0^t [\gamma_T(t) - \gamma_I(t) + \gamma_R(t)] dt \quad (5.8)$$

Similarly, Eq. (5.7) can be integrated to yield specimen strain as a function of time:

$$\gamma_s(t) = \frac{2C_s D_s}{L_s D} \int_0^t \gamma_R(t) dt \quad (5.9)$$

Again, this expression will be disregarded in favor of Eq. (5.8) in the proceeding analyses in order to maintain generality. The shear stress present in the gage section of the specimen can be expressed as:

$$\tau_s(t) = \frac{2T_s(t)}{D_s^2 t_s \pi} \quad (5.10)$$

Here,  $t_s$  is the gage thickness of the specimen.  $T_s$  is the average of the torque exerted on the specimen interface with the incident bar,  $T_I$ , and the torque exerted on the specimen interface with the transmitter bar is  $T_2$ . The torque at the specimen interface with the incident bar can be calculated based on the observed strain waves in the incident bar, as well as the shear modulus and diameter of the bar using Eq. (5.11):

$$T_1(t) = \frac{GD^3\pi}{16} [\gamma_I(t) + \gamma_R(t)] \quad (5.11)$$

Similarly, the torque present at the specimen interface with the transmitter bar is given as:

$$T_2(t) = \frac{GD^3\pi}{16} [\gamma_T(t)] \quad (5.12)$$

By substituting Eqs. (5.11) and (5.12) into Eq. (5.10), the shear stress in the specimen can be expressed directly as a function of the strain waves present in the incident and transmitter bars as:

$$\tau_s(t) = \frac{GD^3}{16D_s^2t_s} [\gamma_I(t) + \gamma_R(t) + \gamma_T(t)] \quad (5.13)$$

As before, the assumption of equilibrium can be utilized to simplify the above expression to be solely a function of  $\gamma_T(t)$  as:

$$\tau_s(t) = \frac{GD^3}{8D_s^2t_s} [\gamma_T(t)] \quad (5.14)$$

The torques  $T_I$  and  $T_2$  can be of additional utility when attempting to quantify the presence of stress equilibrium in the specimen. The torque ratio,  $T_I/T_2$ , can be observed and interpreted to represent the degree to which stress equilibrium has been achieved in the specimen, with a ratio of unity representing perfect equilibrium. As aforementioned, it is often impractical for one to expect such perfect equilibrium in a typical test. However, it

still is important that a torque ratio as near as possible to unity be maintained. Further information regarding principles of operation and theory of the TSHB apparatus can be obtained elsewhere in the literature [19].

#### 5.4 MATERIAL AND SPECIMEN GEOMETRY

The present work utilizes tubular thin-walled specimens, having dimensions depicted in Figure 5.2. The gage section is 2.41 mm in length, with a nominal wall thickness and mean diameter of 0.5 mm and 12.97 mm, respectively. In order to reduce the likelihood of distortion and irregularity in the thin-walled gage length, cutting stresses during manufacturing were minimized by carefully selecting the order in which machining processes were carried out. After being turned to the correct outer diameter, the specimen was drilled to a diameter large enough to accommodate a boring bar. The outer groove was then fashioned, and subsequently the inside diameter was bored to a nominal dimension in very small increments. All machining processes were performed on CNC equipment. Specialized gage blocks were fabricated so that the outer diameter of the thin-walled gage section could be precisely measured, as can be seen in Figure 5.3, accounting for any minimal variations in specimen dimension.

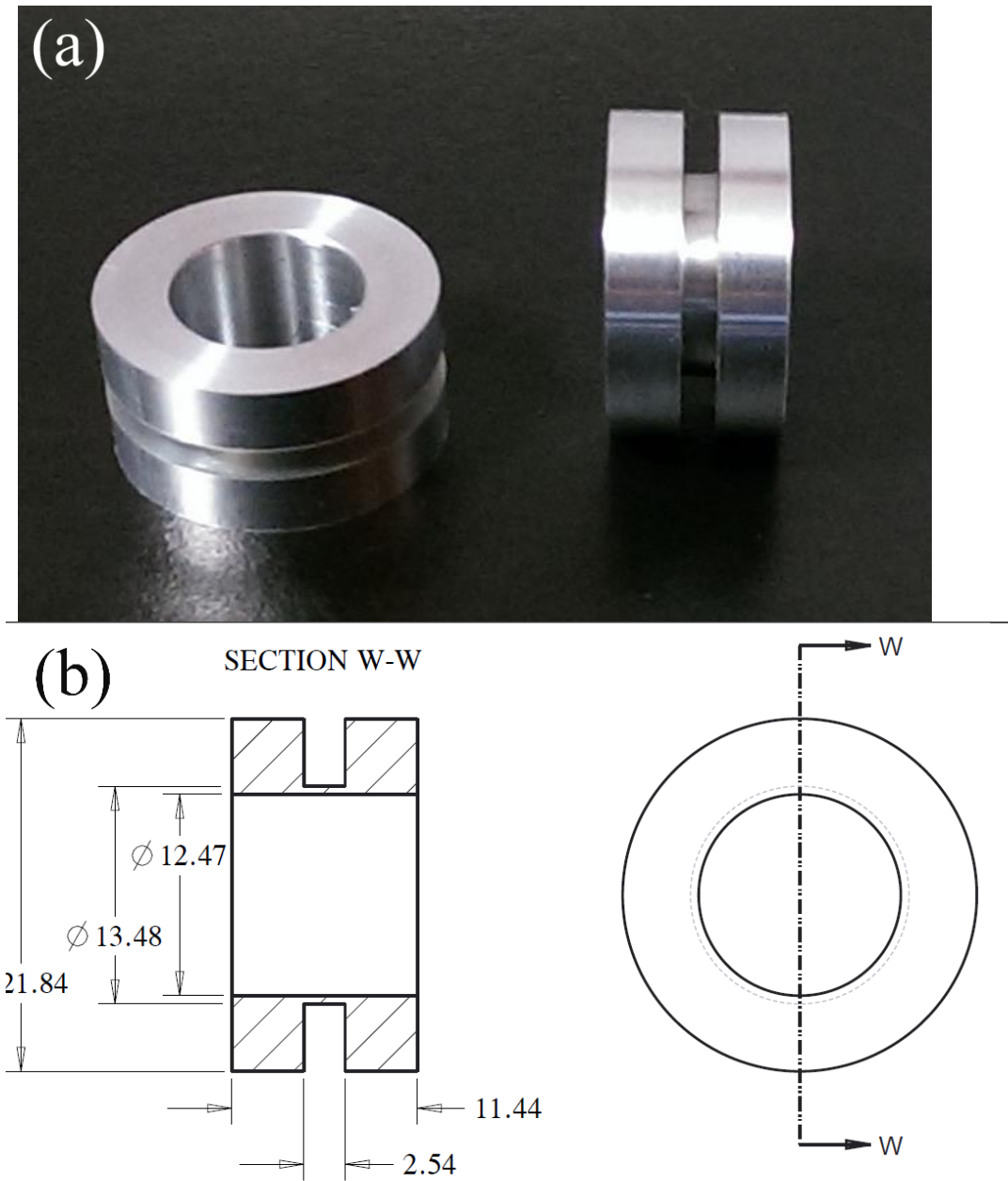


Figure 5.2 Typical thin wall tubular specimens (a) and dimensions, given in mm (b).



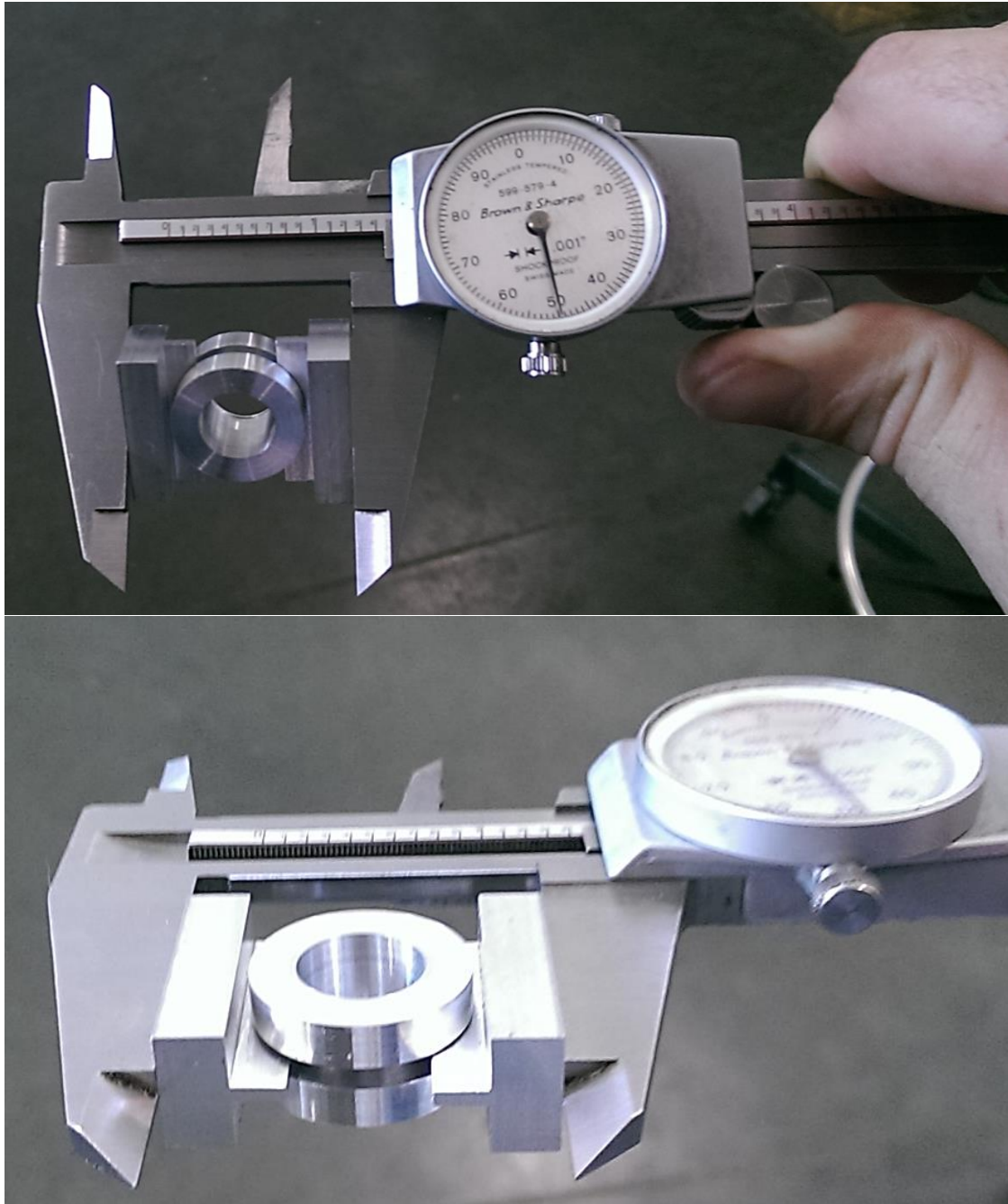


Figure 5.3 Gage blocks used to precisely measure outer diameter of gage section.

Aluminum alloy 7050-T7651 plate manufactured by Kaiser Aluminum was used as the base metal for the present study. The friction stir welding process was used to join two 32 mm thick plates with a butt joint, producing a process zone approximately 19 mm wide at the root and 28 mm wide at the crown. The welding process was carried out on the USC

FSW Process Development System, on which further detail can be found in the literature [11, 12]. This allows for specimens to be extracted exclusively from the large process zone, producing ideal conditions in which the FSW modified material is the sole constituent of the specimen. Specimens were also extracted from the base metal in similar fashion. All specimens were extracted with the specimen axis of symmetry aligned with the rolling and weld directions, as depicted below in Figure 5.4.

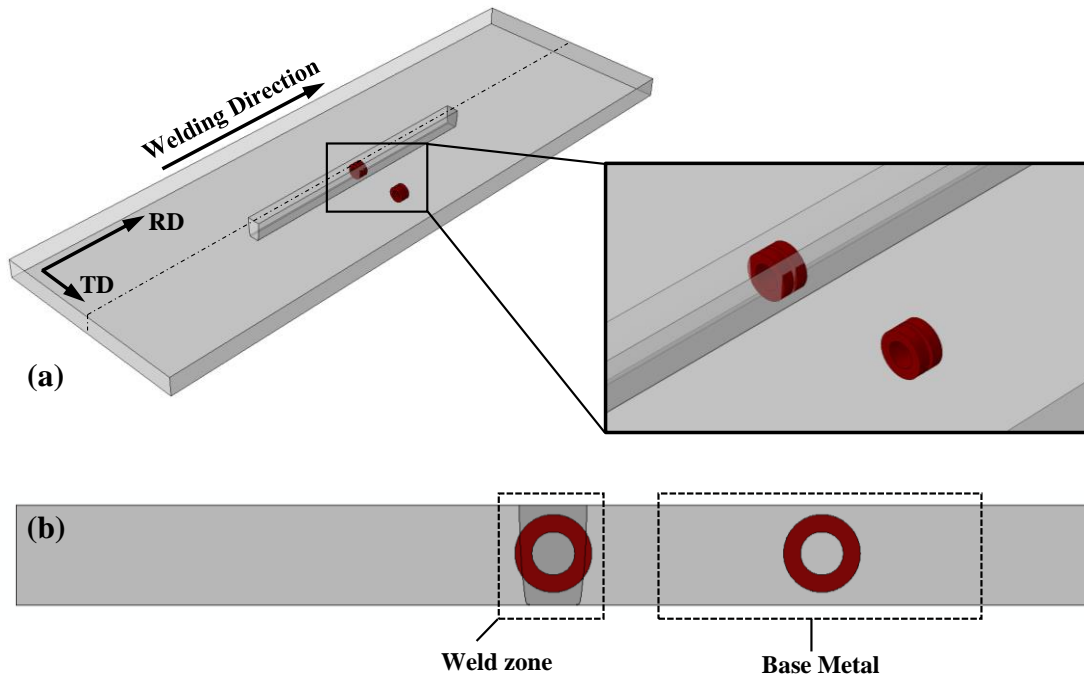


Figure 5.4 Orientation of specimens extracted from FSW process zone and base metal.

The grain structure of the base metal and FSW process zone were observed and analyzed prior to testing. To do so, standard metallographic procedures were followed for each specimen including grinding, polishing, and etching. Keller's etchant solution was utilized to reveal the grain structure of the material, and the average grain size was measured by determining the number of grains intersecting a given length of a random line [20]. The fracture surfaces of the failed specimens were also observed using high resolution scanning electron microscopy (SEM).

## 5.5 EXPERIMENTAL APPARATUS AND PROCEDURE

### 5.5.1 TORSIONAL SPLIT HOPKINSON BAR

The experimental apparatus utilized in the current work is a stored torque TSHB as described in Chapter 2. The apparatus consists of an incident and transmitter bar, each comprised of a 25.4 mm in diameter 7075-T6 aluminum rod, a rotary actuator, and clamping mechanism. A specimen is affixed between the incident and transmitter bar with the use of a high strength epoxy.

### 5.5.2 DATA ACQUISITION

Experimental data is acquired with the use of strain gages mounted on the incident and transmitter bars in conjunction with an oscilloscope. The oscilloscope is also used to trigger data acquisition. Signal conditioning amplifiers are also employed to maximize precision in the obtained strain measurements. Strain gages are mounted in diametrically opposed pairs on each bar, and the outputs averaged for each pair to negate the inevitable presence of small amounts of bending. The gage pairs are mounted in the center of each bar, as to avoid overlap with reflected pulses in each bar.

### 5.5.3 EXPERIMENTAL PROCEDURE

Experiments are carried out by first affixing a specimen between the incident and transmitter bars with the use of a high-strength epoxy. The epoxy is then allowed to cure for several hours to ensure an adequate bond. The clamping mechanism is then readied by installing an unbroken notched bolt into the jaws of the vise. Clamping pressure is applied to the incident bar, and the rotary actuator is then used to apply a predetermined rotation to the free end of the incident bar; thus elastically storing a torque in the portion of the incident bar between the rotary actuator and clamping mechanism. This torque is then

instantaneously released by further applying clamping force, causing the notched bolt to fracture and the clamping jaws to release the incident bar. Torsional stress waves then propagate towards the specimen, dynamically loading the specimen in torsion. Once the wave reaches the specimen, some of the wave is transmitted to the transmitter bar through the specimen while some of the wave is reflected back to the incident bar.

A number of experiments are conducted, using both types of the specimens, at different strain rates. The strain rate was altered by varying the predetermined rotation angle at the end of the incident bar. It is worthwhile to note that the duration of the incident pulse can be varied by changing the position of the clamp relative to the end of the incident bar. However, in these experiments the position of the clamp was fixed at a position facilitating the longest possible duration of the incident pulse while also avoiding overlap of the incident and reflected pulses.

## 5.6 RESULTS AND DISCUSSION

### 5.6.1 MICROSTRUCTURAL OBSERVATIONS

The microstructure of specimens extracted from the base metal and FSW process zone are depicted with micrographic images given in Figure 5.5. The grain structures are remarkably different in size and arrangement. The FSW material is characterized by a remarkably regular structure of small, equiaxed grains with a mean grain size  $9.61\mu\text{m}$ . In stark contrast, the base metal exhibits irregularity in grain size and structure, with a much larger average grain size of  $29.62\mu\text{m}$  and a discernable elongation in the rolling direction. From these measurements, there are approximately 17 grains across the gage thickness of the typical base metal specimen, while about 52 grains exist across the gage thickness in the typical FSW specimen. In either case, the corresponding ratio of grain size to wall

thickness is much larger than the 1:7 ratio present in Al 1100-0 specimens used successfully by Duffy et al [15]. Based on these observations, it would seem clear that a more than adequate representative volume has been present in the gage sections of the specimens used in the present work.

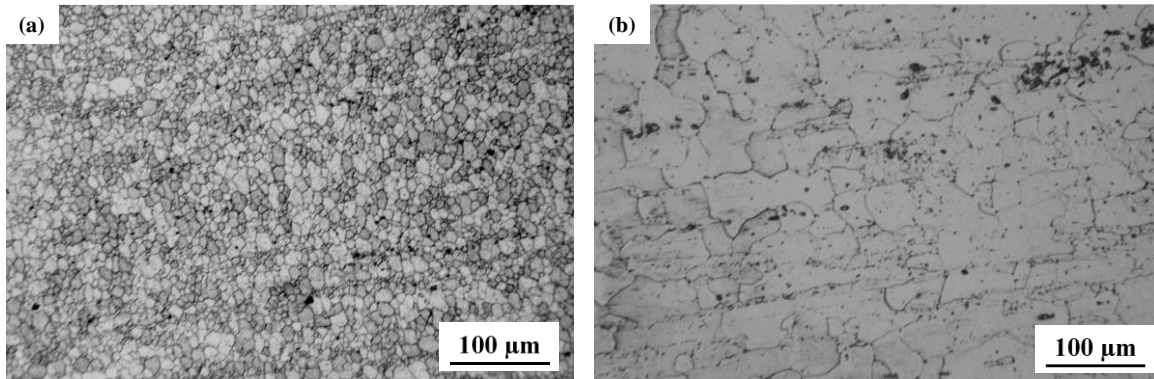


Figure 5.5 Optical micrograph of (a) friction-stir weld fusion zone and (b) base metal.

#### 5.6.2 WAVE ANALYSIS

Typical strain time histories obtained from the gage pairs mounted on the incident and transmitter bars are given in Figure 5.6. The obtained waveforms are nearly ideal, characterized by short rise times, long durations at a constant magnitude, and only small rounded peaks present in the incident pulse immediately after rise time. The relation given in Eq. 5.6 is exemplified in the typical strain histories in Figure 5.8, evident in the prominent increase in the magnitude of the reflected strain pulse, corresponding to the instance at which the transmitted pulse diminishes.

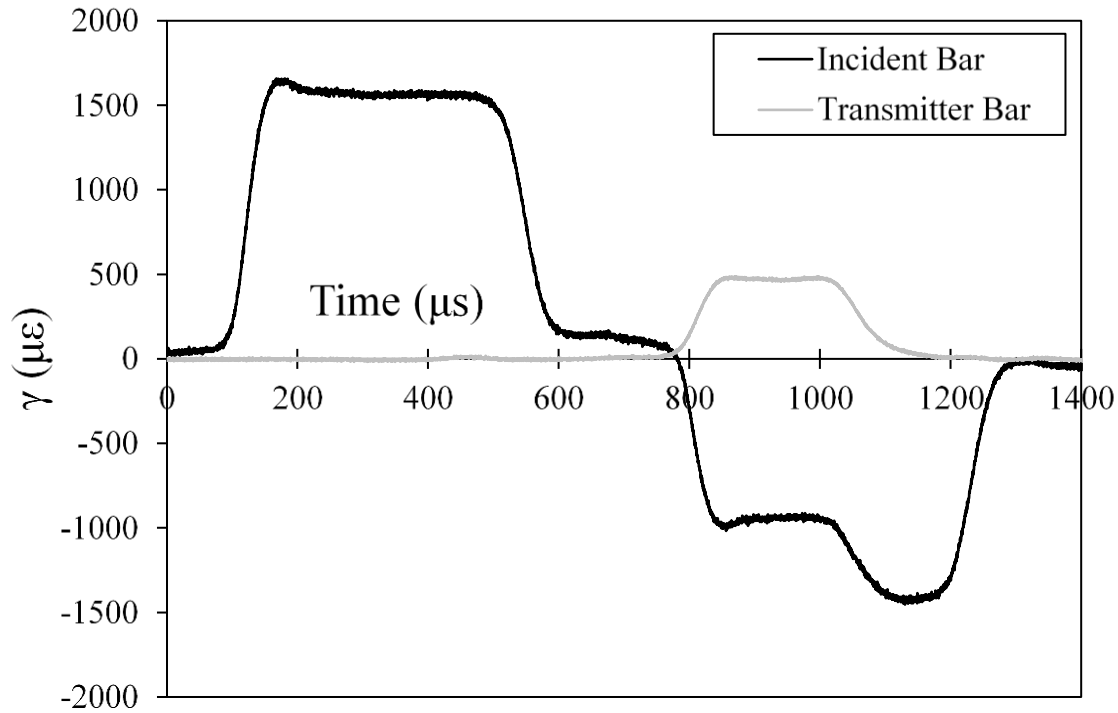


Figure 5.6 Typical Strain histories obtained from gages on incident and transmitter bars.

Typical incident, reflected, and transmitted strain pulses truncated from the strain histories, as shown in Figure 5.7. It is worthwhile to note that the duration of the transmitted pulse is also the duration of the experiment; this is clear from the fact that once the specimen has failed, incident strain pulses can no longer propagate through the specimen into the transmitter bar. The typical pulses shown in Figure 5.7 depict an experimental duration beginning and ending at approximately 100  $\mu\text{s}$  and 300  $\mu\text{s}$ , respectively. The experimental duration is highly dependent upon strain rate, typically decreasing with increasing strain rate.

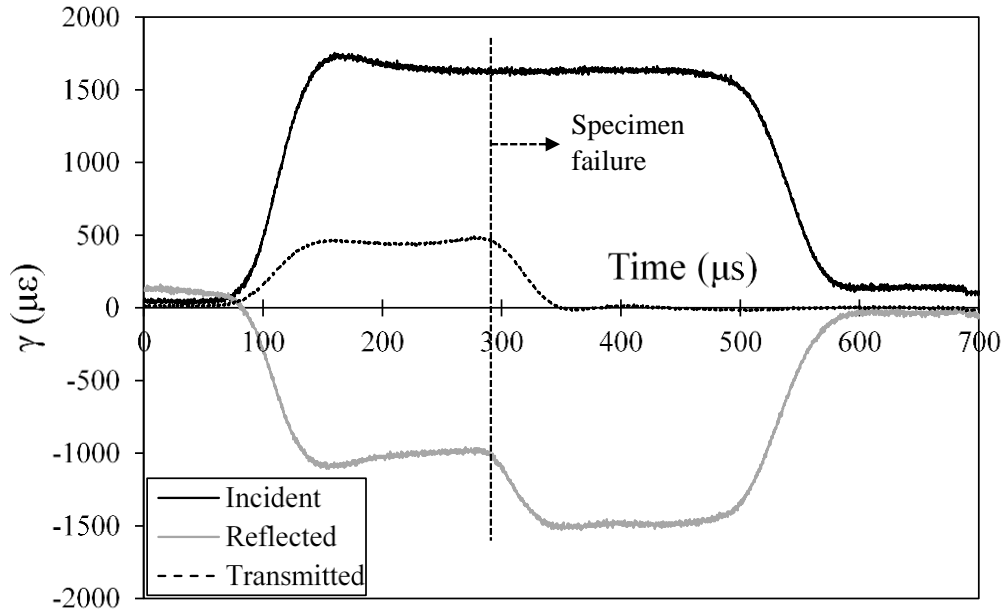


Figure 5.7 Typical incident, reflected, and transmitted strain pulses.

The specimen strain rate can then be found from these pulses by applying Eq. 5.5. A typical evolution of specimen strain rate is given in Figure 5.8. Again, the evolution of specimen strain rate approaches the ideal, with a nearly constant strain rate present in the specimen throughout the entire duration of the experiment. As previously discussed, the ratio of the torques applied to either side of the specimen is generally of significant interest. A typical evolution of this torque ratio is presented in Figure 5.9, depicting a ratio of no less than 0.8. In the present work, this torque ratio was found to be characteristic of the apparatus and specimen geometry, with all tests maintaining a nearly constant value of approximately 0.8 during the entirety of the experimental duration, regardless of strain rates present in the specimen. The torque ratio approaching unity present in all tests discussed in the current work suggests the presence of stress equilibrium in the specimen; a vital assumption that must be met in any TSHB test [15].

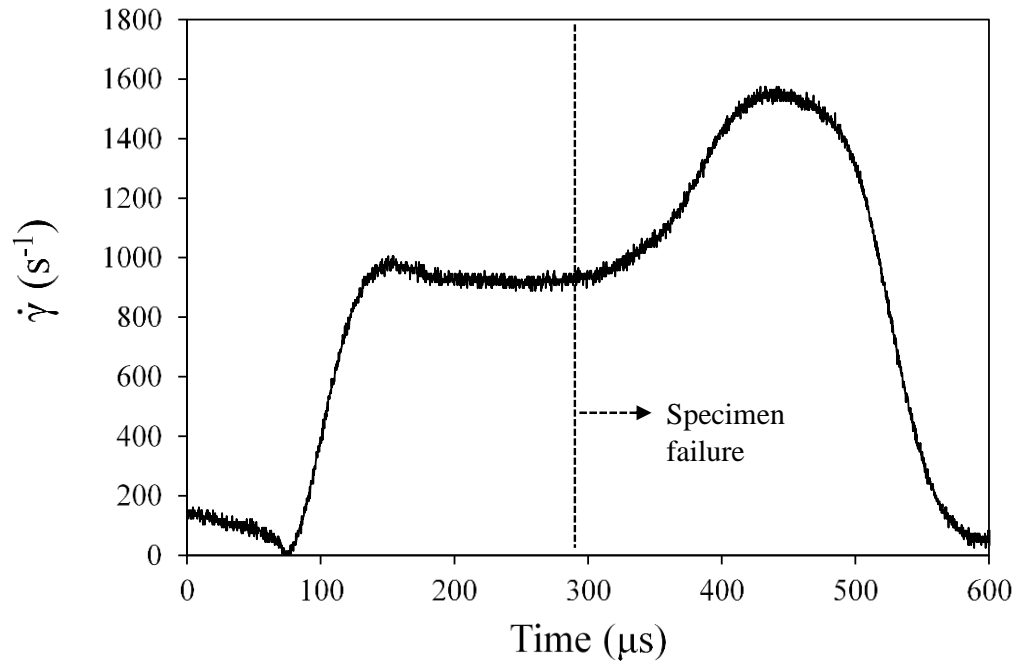


Figure 5.8- Typical evolution of specimen strain rate.

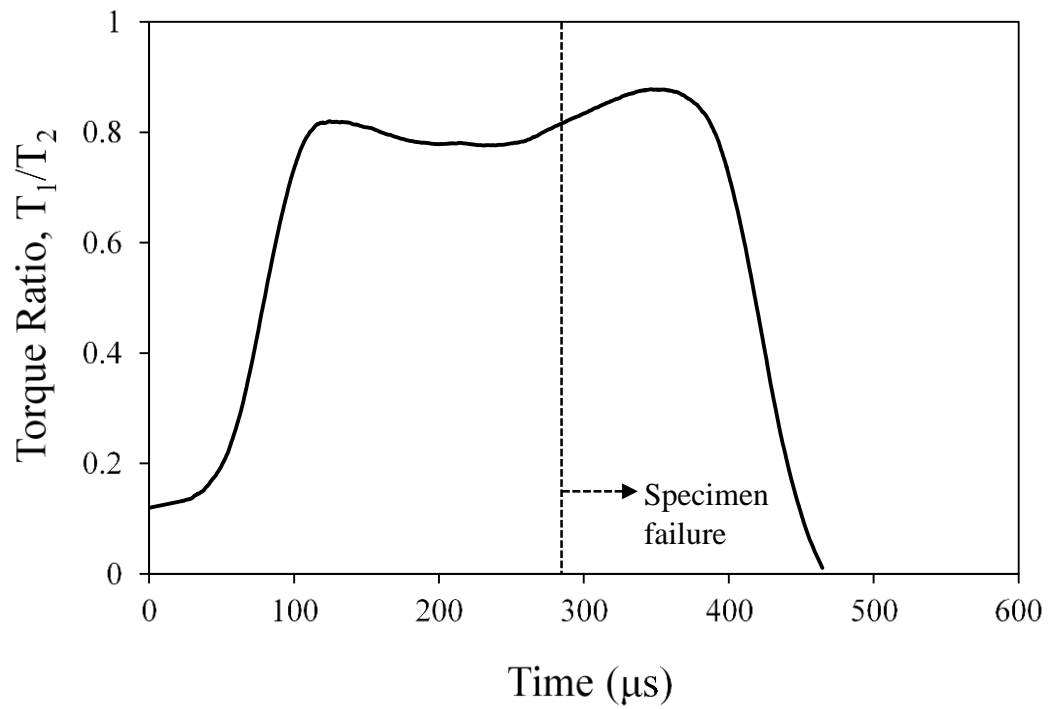


Figure 5. 9 Typical evolution of torque ratio.



### 5.6.3 QUASI-STATIC STRESS-STRAIN BEHAVIOR

Quasi-static tensile tests were performed to evaluate the stress-strain response of both the base and FSW material. Stress strain relations obtained from this testing are given in Figure 5.10. The alloy is found to exhibit obvious differences in mechanical behavior between these two states, as one would expect from the vastly different microstructures observed in each. Most notably, the FSW material state experiences a relatively large amount of work hardening while also exhibiting a lower yield and flow stress. In contrast, the base metal exhibits stronger mechanical properties, including a much higher yield stress, while the plastic flow stress remains nearly constant thereafter with minimal work hardening. Considering the remarkably smaller grain size present in the FSW specimen, a higher yield strength was expected, following the well-established Hall-Petch relation [21, 22]. However, one should note that although the grain size is smaller in the FSW specimens, the base metal might have been subjected to various deformation and heat treatment cycles prior to the welding process, through which a highly work hardened structure could have been developed within the base metal. Such highly work-hardened structure, which is usually accompanied with a large dislocation density and a high internal stored energy, may be interpreted as the reason behind the stronger mechanical response observed for base-metal specimen in this work. Consideration of the processing history of the as-received AA7050 plates is not within the scope of this work.

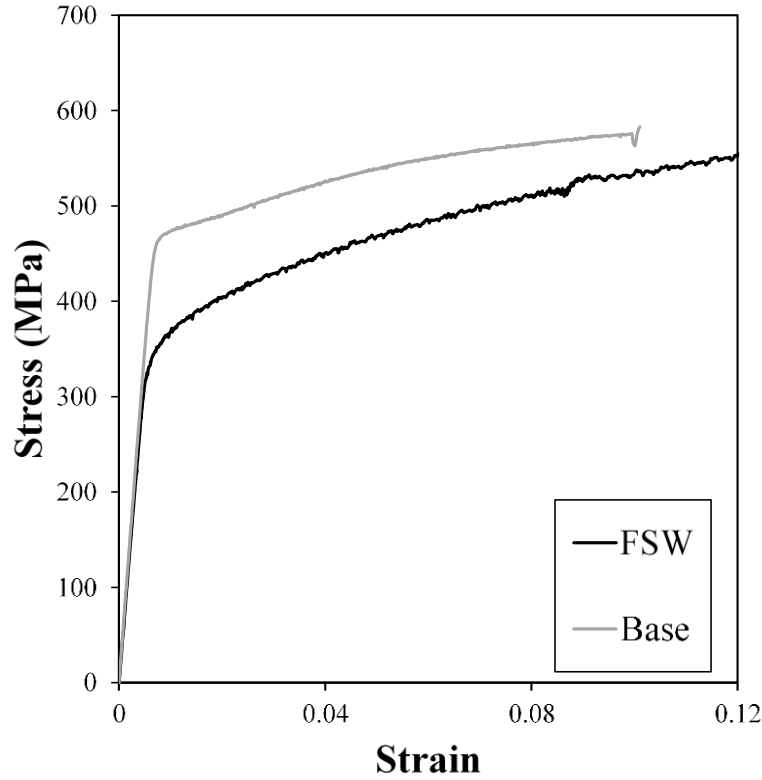


Figure 5.10 Stress-strain curves obtained from quasi-static tensile tests for FSW and base metal.

#### 5.6.4 DYNAMIC STRESS-STRAIN BEHAVIOR

Stress-strain curves obtained at elevated strain rates are presented for FSW and as received material in Figure 5.11. These resulting stress strain curves are given in terms of effective stress, strain, and strain rate using the relations in Eq. 5.15 in order to facilitate comparison with quasi-static tensile tests.

$$\bar{\sigma} = \sqrt{3}\tau \quad (5.15-a)$$

$$\bar{\epsilon} = \frac{\gamma}{\sqrt{3}} \quad (5.15-b)$$

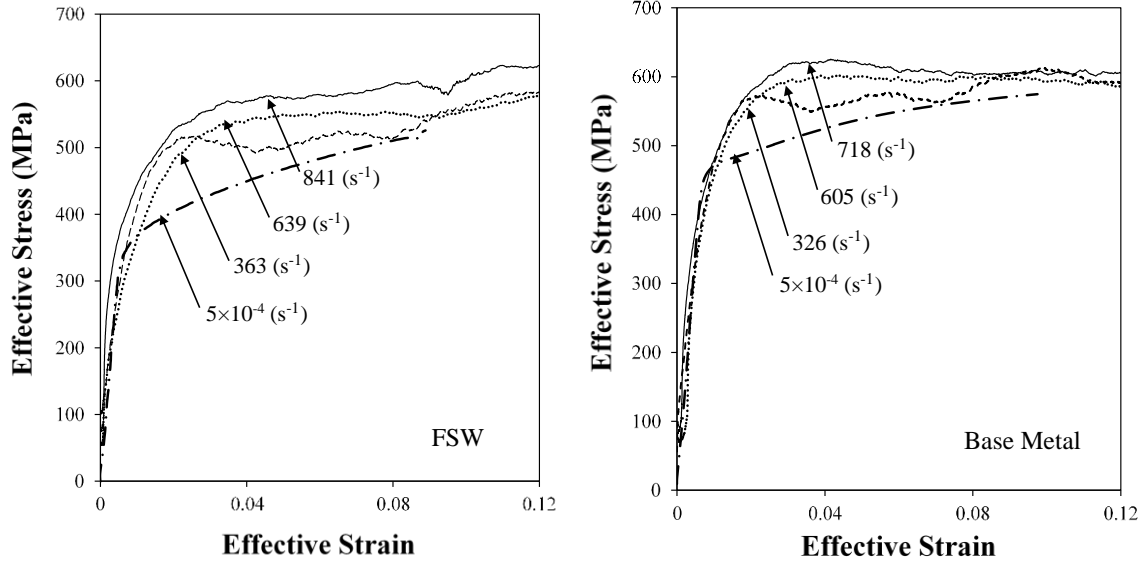


Figure 5.11 Stress-strain curves experimentally obtained from dynamic torsion tests.

The dynamic curves are found to lie above those obtained from quasi-static conditions in all cases, indicating some appreciable strain rate dependence in both material states for the range of strain rates considered in this study. Stress levels increase gradually with increasing strain rate. Stress levels in dynamic tests on specimens extracted from FSW material appear to be slightly more rate dependent when compared to similar tests on base metal. For both material states, the rate of work hardening obtained from dynamic torsional testing is observed to be less than that found in the corresponding quasi-static case. The FSW material continues to be consistently weaker than the base metal at elevated strain rates. The stress-strain relations obtained experimentally at elevated strain rates for this alloy were fitted using the Hill fitting function, taking the form depicted below in Eq. 16.

$$\bar{\sigma} = A \frac{\bar{\epsilon}^n}{K^n + \bar{\epsilon}^n} \quad (5.16)$$

This type of fitting yields curves having very high coefficients of determination with respect to the experimentally obtained dynamic data, typically 0.96 and above. It should

be made clear that these fitted curves are proposed only to facilitate analysis within the range of parameters explored experimentally herein. Therefore, the Hill equation and the corresponding parameters found from the experimental data are not proposed as a constitutive model nor are they used as such in the present work. These fitted curves are shown in Figure 5.12 alongside the quasi-static data.

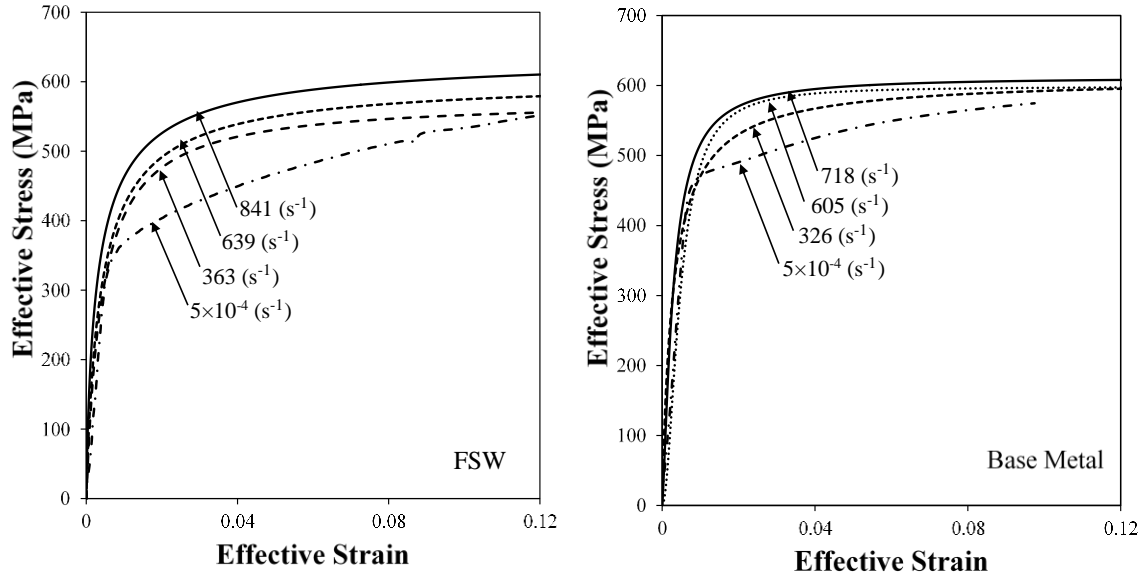


Figure 5.12 Fitted stress-strain curves obtained using experimental data.

Work hardening rates are extracted from the fitted stress-strain curves as presented in Figure 5.13. In all instances, the FSW material is seen to exhibit substantially more work hardening than the base metal. Furthermore, increasing strain rates appear to lower the work hardening rate in the FSW material, where work hardening rates are seen to converge in all high strain rate tests to a value that is approximately 60% of that observed in the quasi-static case. The base metal again diverges from this trend, with some increase in work hardening rate occurring at elevated strain rates when compared to the quasi-static case. The dynamic tests again exhibit some convergence at only slightly elevated work

hardening rates for the base metal. All work hardening rates are seen to decrease with increasing strain.

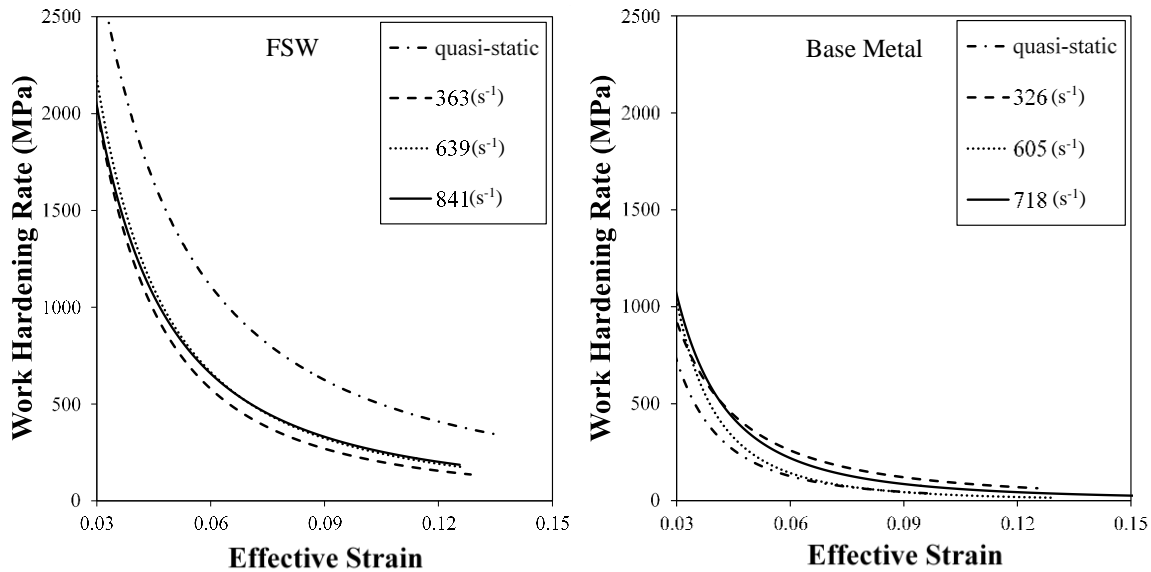


Figure 5.13 Work hardening rates extracted from fitted stress-strain curves.

This increased strain hardening observed in the FSW material when compared to the base metal is likely related to the differences in grain structure between the two. The substantially smaller and equiaxed grain structure present in the FSW material may provide a shorter path for the free movement of dislocations during the deformation process [23]. For a known deformation occurring over a given time, this shorter path may induce a higher rate of dislocation pile up at grain boundaries, resulting in an increased work hardening. On the other hand, the irregular, large grain structure comprising the base metal may induce an opposite mechanism, in which longer free paths for dislocations might result in lower rates of dislocation pile up at grain boundaries, thus resulting in a lower work hardening rate [23].

In explaining the decrease in work hardening observed in the FSW material as strain rates increase, the dislocation annihilation phenomenon must be considered. This

phenomenon occurs especially in metals with high stacking fault energy (SFE), such as aluminum alloys, for which recovery is the principle restoration mechanism [24]. At high strain rates, dislocation density will increase at a higher rate, and therefore the chance of dislocation annihilation increases at a corresponding rate. This results in a lower overall dislocation density in the microstructure of the material. As a result of this lower overall dislocation density, work hardening would be seen to decrease at elevated strain rates. Such a mechanism is actually evident in the experimental data, wherein dynamic experiments tend to achieve a plateau in the shape of the stress strain curve at strain levels much lower than those at which plateaus are achieved in similar quasi-static tests.

#### 5.6.5 FRACTOGRAPHY

Fracture surfaces present on FSW and base metal specimens tested at the highest strain rates achieved were examined with the use of a scanning electron microscope (SEM). Images of these fracture surfaces are presented in Figure 5.14. Voids are apparent in the fracture surface of both specimen types, indicative of a ductile failure mechanism [16, 25]. This observation is bolstered by the large amounts of strain achieved prior to failure in all tests. These voids are proportionate to the grain size, and as expected are much smaller in the FSW material when compared to the base metal. The shape of a typical void appears to be elongated in the direction of the applied shear stress in both specimen types, as is illustrated in the images with the use of arrows.

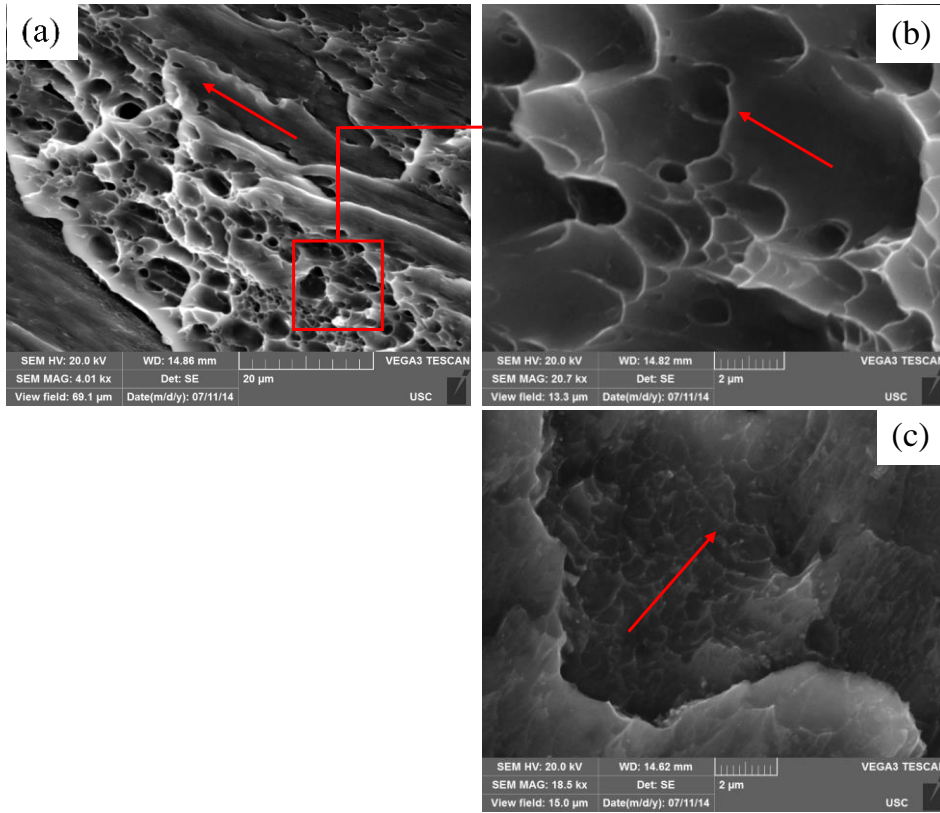


Figure 5.14 SEM images of fracture surfaces present on a base metal specimen low (a) and high (b) magnification, and a FSW material specimen at high magnification (c).

## 5.7 CONCLUSIONS

A TSHB apparatus has been used to perform high strain rate testing on aluminum alloy 7050T-6571 in both the as received and friction-stir welded conditions. Quasi-static tensile tests have been performed for reference on both material states. The microstructures of each state are observed to be vastly different, as the FSW state containing small, equiaxed grain structure while the base metal consists of an irregular and much larger grain structure.

Quasi-static tests characterize the FSW as having generally weaker mechanical behavior, accompanied by increased strain hardening when compared to the base metal. This trend is also apparent at elevated strain rates, as the FSW material continues to exhibit

lower yield and plastic flow stresses when compared to the base metal. Dynamic tests are indicative of the existence of some strain rate sensitivity in both material states, however this is slightly more pronounced in the FSW material. This rate dependence manifests in the form of higher stresses at material yield and during plastic flow, as well as an increase in strain levels achieved at the onset of plateau. Work hardening is almost unchanged in the base metal at elevated strain rates. Conversely, the FSW material exhibits a decreased propensity for work hardening at elevated strain rates. SEM observations of fracture surfaces present on specimens tested at elevated strain rates depict the presence of voids in both material states, having diameters commensurate with grain sized. Elongation is also apparent in these voids, occurring in the direction of applied shear stress. The presence of voids suggests the material remains ductile in both the FSW and base metal states at dynamic strain rates.



## LIST OF REFERENCES

- [1] Heinz A, Haszler A, Keidel C, Moldenhauer S, Benedictus R, Miller WS. Recent development in aluminum alloys for aerospace applications. *Mater Sci Eng A* 2000; 280: 102-7.
- [2] Immarigeon JP, Holt RT, Koul AK, Zhao L, Wallace W, Beddoes JC. Lightweight materials for aircraft applications. *Mater Charact* 1995; 35: 41–6.
- [3] Wu Y, Froes F, Alvarez A, Li C, Liu J. Microstructure and properties of a new super-high-strength Al–Zn–Mg–Cu alloy C912. *Mater Design* 1997; 18: 211-15.
- [4] Hill MR, Panontin TL. Micromechanical modeling of fracture initiation in 7050 aluminum. *Eng Fract Mech* 2002; 69: 2163–86.
- [5] Li J, Li F, Xue F, Cai J, Chen B. Micromechanical behavior study of forged 7050 aluminum alloy by microindentation. *Mater Design* 2012; 37: 491-99.
- [6] Li J, Li F, He M, Xue F, Zhang M, Wang C. Indentation technique for estimating the fracture toughness of 7050 aluminum alloy with the Berkovich indenter. *Mater Design* 2012; 40: 176-84.
- [7] Han NM, Zhang XM, Liu SD, He DG, Zhang R. Effect of solution treatment on the strength and fracture toughness of aluminum alloy 7050. *J Alloy Compd* 2011; 509: 4138-45.
- [8] Ren X, Zhang L, Chen Y, Sun F, Zhang W, Lin L, Wang Y. Tensile and Fatigue Properties of 7050 Aluminum Alloy Axle Box used for High Speed Train. *Procedia Eng* 2012; 27: 914-22.
- [9] Zheng LJ, Li HX, Hashmi MF, Chen CQ, Zhang Y, Zeng MG. Evolution of microstructure and strengthening of 7050 Al alloy by ECAP combined with heat-treatment. *J Mater Process Tech* 2006; 171: 100-7.
- [10] Mendes N, Loureiro A, Martins C, Neto P, Pires JN. Effect of friction stir welding parameters on morphology and strength of acrylonitrile butadiene styrene plate welds. *Mater Design* 2014; 58: 457-64.
- [11] Thomas WM, Nicholas ED. Friction stir welding for the transportation industries. *Mater Design* 1997; 18: 269-73.

- [12] Canaday CT, Moore MA, Tang W, Reynolds AP. Through thickness property variations in a thick plate AA7050 friction stir welded joint. *Mater Sci Eng A* 2013; 559: 678-82.
- [13] Upadhyay P, Reynolds AP. Effects of thermal boundary conditions in friction stir welded AA7050-T7 sheets. *Mater Sci Eng A* 2010; 527: 1537-43.
- [14] Naik NK, Asmelash A, Kavala VR, Ch V. Interlaminar shear properties of polymer matrix composites: Strain rate effect. *Mech Mater* 2007; 39: 1043-52.
- [15] Duffy J, Campbell JD, Hawley RH. On the use of a torsional split Hopkinson bar to study rate effects in 1100-0 aluminum. *J Appl Mech* 1971; 38: 83-91.
- [16] Lee WS, Cheng JI, Lin CF. Deformation and failure response of 304L stainless steel SMAW joint under dynamic shear loading. *Mater Sci Eng A* 2004; 381: 206-15.
- [17] Kobayashi T, Simons JW, Brown CS, Shockey DA. Plastic flow behavior of Inconel 718 under dynamic shear loads. *Int J Impact Eng* 2008; 35: 389-96.
- [18] Gilat A, Cheng CS. Modeling torsional split Hopkinson bar tests at strain rates above  $10,000 \text{ s}^{-1}$ . *Int J Plast* 2002; 18: 787–99.
- [19] Gilat A. Torsional Kolsky Bar Testing. In: Kuhn H, Medlin D, editors. *ASM Handbook Volume 8: Mechanical Testing and Evaluation*, Ohio: ASM; 2000, p. 505-15.
- [20] Higginson RL, Sellars CM. *Worked examples in quantitative metallography*. UK: Maney Publishing; 2003.
- [21] Sato YS, Urata M, Kokawa H, Ikeda K. Hall-Petch relationship in friction stir welds of equal channel angular-pressed aluminum alloys. *Mater Sci Eng A* 2003; 354: 298-305.
- [22] Hansen N. Hall-Petch relation and boundary strengthening. *Scripta Mater* 2004; 51: 801-6.
- [23] Barlat F, Glazov, MV, Brem JC, Lege JC. A simple model for dislocation behavior, strain and strain rate hardening evolution in deforming aluminum alloys. *Int J Plasticity* 2002; 18: 919-39.
- [24] Humphreys FJ, Hatherly M. *Recrystallization and related annealing phenomena*. 2<sup>nd</sup> ed. UK: Elsevier; 2004.
- [25] Hull D. *Fractography – Observing, measuring and interpreting fracture surface topography*. UK: Cambridge University Press, 1999.

## CHAPTER 6

### SUMMARY AND RECOMMENDATIONS

#### 6.1 SUMMARY

Experimental equipment capable of examining mechanical properties of engineering materials at elevated strain rates has been designed, constructed, and utilized to test composite, foam, and aluminum specimens under dynamic loading conditions. The shock tube apparatus and TSHB apparatus detailed in this work, along with the experimental research conducted with their use, are the culmination of tremendous amounts of work by the author. The appreciable strain rate dependence observed in the experimental studies detailed in the current work exemplify the importance of characterizing engineering materials at elevated strain rates, as their mechanical and fracture properties can vary considerably with increasing strain rate.

#### 6.2 RECOMMENDATIONS

Based on experience during the experimental studies described in this work, some recommendations regarding future work efforts that may employ the shock tube and TSHB are provided in this section.

##### 6.2.1 SHOCK TUBE

The shock tube apparatus is seen to work exceedingly well in all cases observed thus far. However, there are some details of the apparatus which the author feels could be improved for the sake of convenience.

Each use of the shock tube requires the replacement of the Mylar diaphragm, which necessitates the disassembly of the juncture between the driver and driven sections as depicted in chapter 2. As it sits, this requires that the operator loosen and remove a total of 6 large nuts and bolts as shown in Figure 6.1. Although this may not sound entirely unreasonable, in practice this task becomes quite tedious and is a distraction when conducting intensive research. To facilitate easier access to the diaphragm, an alternative type of fastener should be considered. One possible option would be the use of a cam clamp. This is a type of quick release fastener that is capable of applying considerable clamping forces (1000 lbf or more). The cam clamp is advantageous as it requires only  $\frac{1}{4}$  turn to engage or disengage, and can be operated manually without the use of tools. To incorporate such a fastener, the author has conceived a design that utilizes cam levers in lieu of nuts. This design also incorporates slots cut into the flanges to facilitate a quick and easy removal of the bolt and cam lever as a unit, thus granting timely access to the Mylar diaphragm with minimal effort. Further calculations will be necessary to specify the size and number of cam clamps that would be necessary for this application.

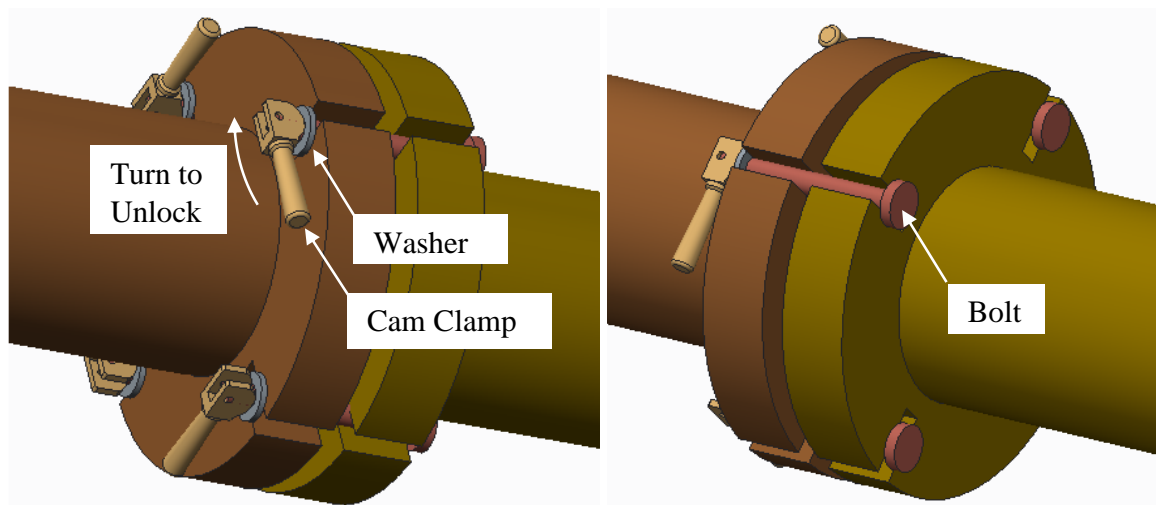


Figure 6.1 Suggested design for use of quick release fasteners to secure driver and driven sections.

Finally, it has been observed by the author that the current regulator used to dispense pressurized helium into the driver section of the tube may not be correctly sized. When diaphragms consisting of several plies of Mylar are used, the regulator does not facilitate a sufficient range of adjustment to allow for the higher pressures needed to burst these multi-layer diaphragms. It is suggested that a regulator capable of producing higher pressures at the outlet be sourced and utilized in place of the current device.

#### 6.2.2 TORSIONAL SPLIT HOPKINSON BAR

The TSHB has also exhibited exemplary performance in experimental use. However, in the author's experience there are some details of regarding use of the apparatus that could be improved upon.

One of the most challenging aspects of TSHB testing is specimen attachment. The means of attachment must provide a robust mechanical coupling with a minimal discontinuity in impedance. The most effective and reliable method is the use of an epoxy, as was the case in the TSHB study already presented here. This method is reliable and relatively easy, but the use of epoxy carries with it an inherent limitation on the torque that can be transmitted through the coupling, as the shear strength of the epoxy is small in comparison to most engineering material. This issue can be mitigated by increasing the contact area between the specimen and bar, however the specimen type utilized in the present study offers only a finite surface area. This presents a problem when testing materials that have high flow stresses, and/or specimens having a larger mean diameter in the gage section. Larger mean gage diameters in the specimen are desirable, as they facilitate higher strain rates in the specimen. One final issue with the use of epoxy in conjunction with conventional specimen geometry is the difficulty one encounters when

attempting to mount the specimen such that it is concentric with the incident and transmitter bar.

To address these issues, the author would suggest a modified specimen geometry that facilitates a larger interfacial area with the bars and also allows for a larger diameter gage section. The larger interfacial area would provide a more robust coupling, allowing greater torques to be transmitted to the specimen. The proposed specimen geometry is depicted in Figure 6.2. Although slightly more difficult to manufacture than the conventional tubular specimen, this design may offer the capability to test stronger materials at greater strain rates.

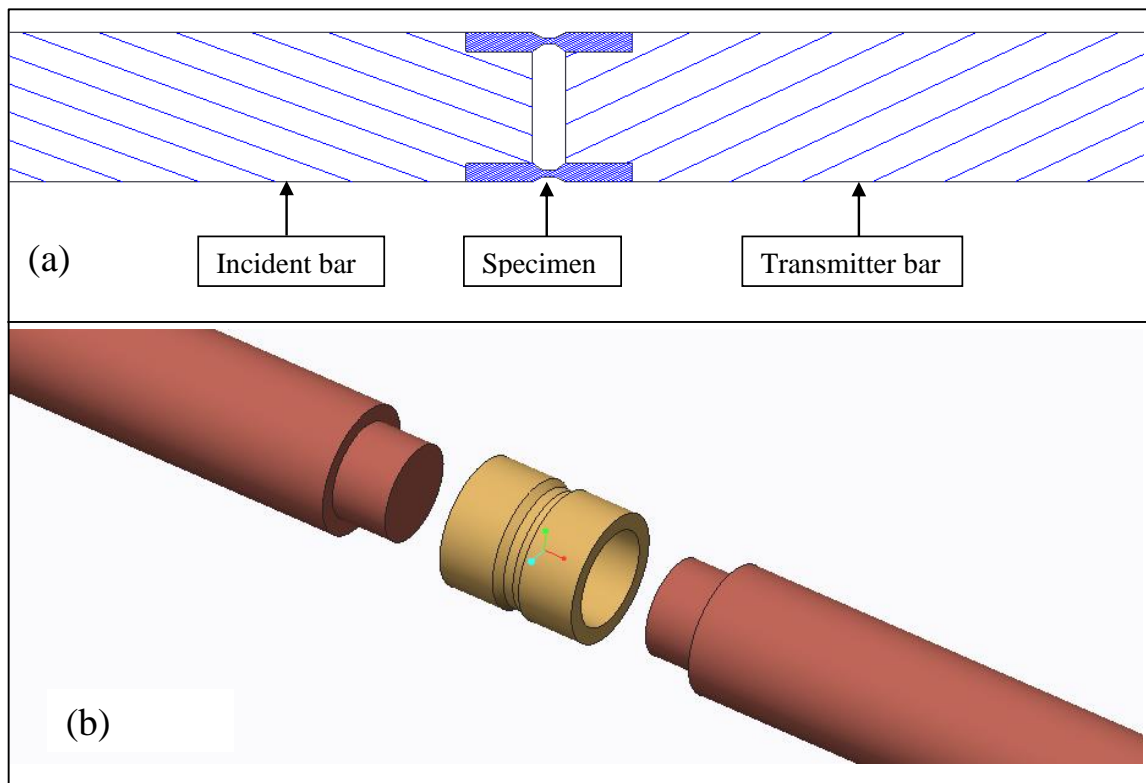


Figure 6.2 Cross section (a) and 3D model of suggested specimen interface with bars.

One final issue encountered by the author is the presence of some bending in the strain pulses produced by the TSHB. It is believed that this is the result of an oversight

during the development of the clamping jaw, wherein a slot was made in place of a hole. The result is an undesired degree of freedom had by the clamping jaws, and the absence of the force couple at the pins that is necessary to counteract the moment applied by the rotary actuator. As static equilibrium must still be achieved, the force couple must then be exerted on the clamping jaws by the linear actuators. By inspection, an elementary static analysis would indicate this is a circumstance that is far from ideal. This issue is depicted schematically in Figure 6.3.

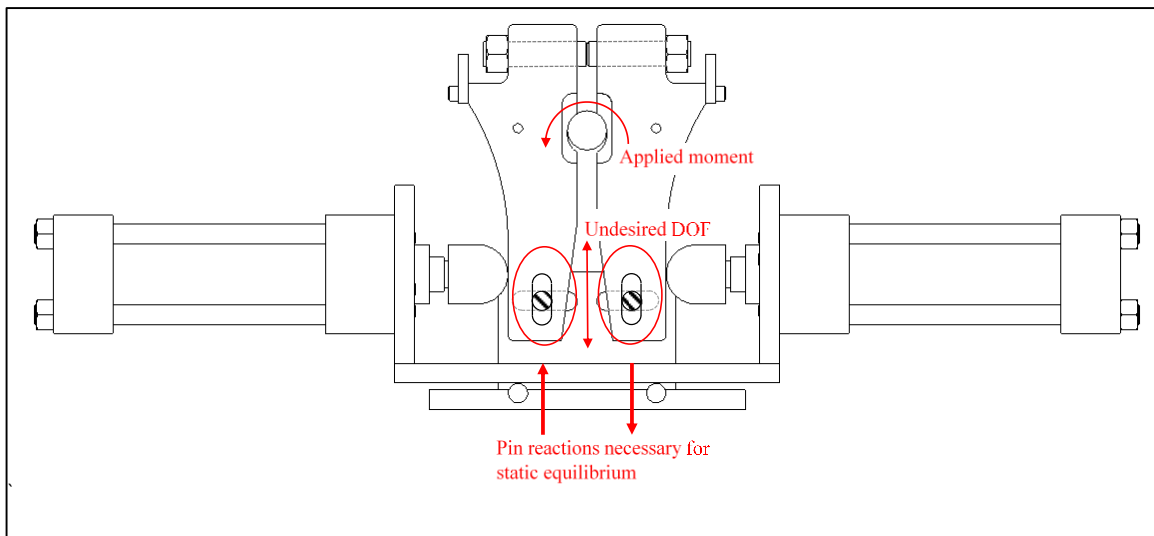


Figure 6.3 Diagram of excessive DOF in clamping mechanism.

To remedy this issue, it is the suggestion of the author that an insert with a threaded hole, which accommodates a stud, be fashioned to fit into the slot on each clamping jaw. This solution is depicted in Figure 6.4. This would save the effort of remanufacturing the clamping jaws while still effectively providing the reaction forces necessary to return the clamping jaws to a state of static equilibrium under load.

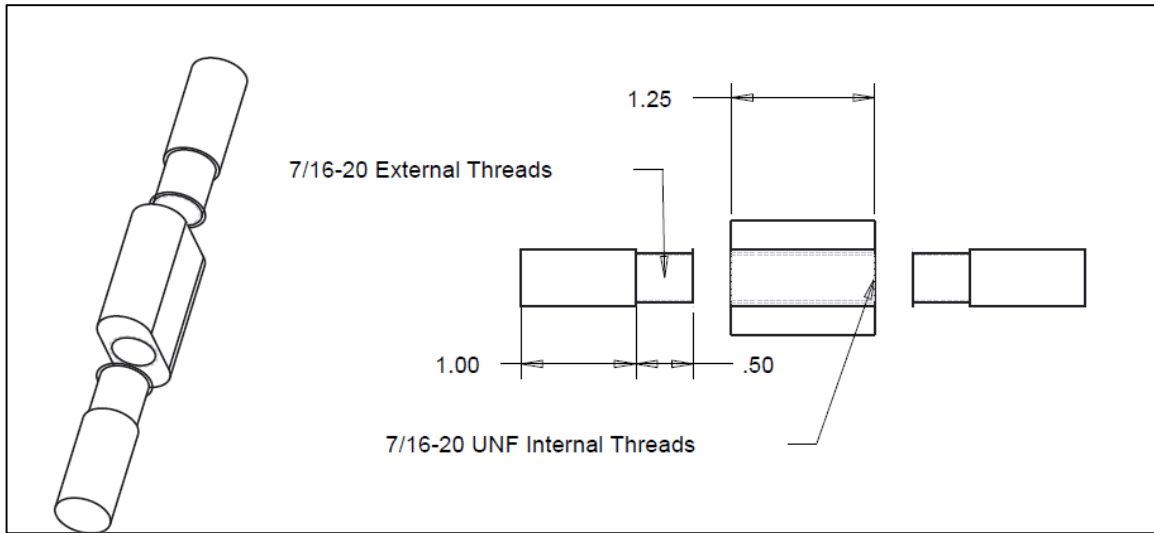


Figure 6.4 Suggested insert and studs to remedy static equilibrium issue in clamp.



## BIBLIOGRAPHY

Anderson TL (2005) Fracture mechanics – Fundamentals and applications, 3rd ed. Taylor & Francis, Florida, pp 360-369.

Armstrong RW, Walley SM. High strain rate properties of metals and alloys, *Int Mater Rev* 2008; 53: 105-128.

Baker WW, Yew CH. Strain Rate Effects in the Propagation of Torsional Plastic Waves, *J Appl Mech* 1966; 33: 917–23.

Barker DB, Sanford RJ, Chona R. Determining K and related stress-field parameters from displacement fields. *Exp Mech* 1985; 25: 399-407.

Berger JR, Dally JW. An overdeterministic approach for measuring  $K_I$  using strain gages. *Exp Mech* 1988; 28: 142-45.

Cernak I, Wang Z, Jiang J, Bian X, Savic J. Ultrastructural and functional characteristics of blast injury-induced neurotrauma. *J Trauma* 2001; 50: 695-706.

Chu TC, Ranson WF, Sutton MA, Peters WH. Application of digital image correlation technique to experimental mechanics. *Exp Mech* 1985; 25: 232-45.

Compston P, Jar PYB, Davies P. Matrix effect on the static and dynamic interlaminar fracture toughness of glass-fiber marine composites. *Compos Part B-Eng* 1998; 29B: 505-16.

Courtney E, Courtney A, Courtney M. Shock tube design for high intensity blast waves for laboratory testing of armor and combat materiel. *Defense Tech* 2014; 10: 245-50.

Cranz C, Schardin H. Kinematographie auf ruhendem Film und mit extrem hoher Bildfrequenz. *Z Phys* 1929; 56: 147–83.

Duffy J, Campbell JD, Hawley RH. On the Use of a torsional split Hopkinson bar to study rate effects in 1100-O aluminum. *J Appl Mech* 1971; 38: 83–91.

Dyer SR, Lassila LVJ, Jokinen M, Vallittu PK. Effect of fiber position and orientation on fracture load of fiber-reinforced composite. *Dent Mater* 2004; 20: 947-55.

Fernandez-Canteli A, Arguelles A, Vina J, Ramulu M, Kobayashi AS. Dynamic fracture toughness measurements in composites by instrumented Charpy testing: influence of aging. *Compos Sci Technol* 2002; 62: 1315-25.

Fomin, NA. 110 years of experiments on shock tubes. *J Eng Thermophys* 2010; 83: 1118-35.

Gama BA, Lopatnikov SL, Gillespie JW. Hopkinson bar experimental technique: a critical review. *Appl Mech Rev* 2004; 57: 223-50.

Gilat A. Torsional Kolsky Bar Testing. In: Kuhn H, Medlin D, editors. *ASM Handbook Volume 8: Mechanical Testing and Evaluation*, Ohio: ASM; 2000, p. 505-15.

Hartley KA, Duffy J, Hawley RH. The torsional Kolsky (Split-Hopkinson) bar. In: Kuhn H, Medlin D, editors. *ASM Handbook Volume 8: Mechanical Testing*, Ohio: ASM; 1980, p. 278-82.

Heimbs S, Heller S, Middendorf P, Hahnel F, Weisse J. Low velocity impact on CRFP plates with compressive preload: test and modeling. *Int J Impact Eng* 2009; 36: 1182-93.

Helm JD, McNeill SR, Sutton MA. Improved three-dimensional image correlation for surface displacement measurement. *Opt Eng* 1996; 35: 1911-1920.

Henshall, BD. On some aspects of the use of shock tubes in aerodynamic research. UK: H.M. Stationery Office, 1957.

Holder, DW. A note on shock tubes. Ministry of supply- aeronautical research council 1953; 110: 1-18 (technical note).

Hopkinson B. A method of measuring the pressure produced in the detonation of high explosives or by the impact of bullets. *Philos Trans R Soc London A* 1914; 213: 437–56.

Hopkinson J. Further experiments on the rupture of iron wire. In: Hopkinson B (Editor), *Original Papers-by the late John Hopkison*, Scientific Papers, Cambridge Univ Press, 1901.

Jin, H. Lu, W.Y. Hong, S. Connelly, K. Fracture behavior of polyurethane foams, *Society for Experimental Mechanics*, Springfield MA, 2007.

Justusson B, Pankow M, Heinrich C, Rudolph M, Waas AM. Use of a shock tube to determine the bi-axial yield of an aluminum alloy under high strain rates. *Int J Impact Eng* 2013; 58: 55-65.

Kabir, M.D. Saha, M.C. Jeelani, S. Tensile and fracture behavior of polymer foams, *Materials Science and Engineering A* 429, 225–235, 2006.

Khanna SK, Shukla A. Development of stress field equations and determination of stress intensity factor during dynamic fracture of orthotropic composite materials. *Eng Fract Mech* 1994; 47: 345-59.

Khanna SK, Shukla A. On the use of strain gages in dynamic fracture mechanics. *Eng Fract Mech* 1995; 51: 933-48.

Kidane A. On the Failure and Fracture of Polymer Foam Containing Discontinuities. *ISRN Mater Sci* 2013; 2013: 1-9.

Kidane, A. Ravichandran, G. Failure and Fracture Behavior of Brittle Polymer Foam, *Experimental and Applied Mechanics, Conference Proceedings of the Society for Experimental Mechanics Series, Volume 6*, 91-98, 2011.

Kidane, A. On the failure and fracture of polymer foam containing discontinuities, *ISRN Materials Science*, 2013, 1-9, 408596, 2013.

Kidane, A. Shukla A. Quasi-Static and Dynamic Fracture Initiation Toughness of Ti/TiB Layered Functionally Graded Material under Thermo-Mechanical Loading. *Eng Fract Mech* 2010; 77: 479-91.

Kim K, Ye L. Effects of thickness and environmental temperature on fracture behavior of polyetherimide (PEI). *J Mater Sci* 2004; 39: 1267-76.

Kokaly MT, Lee J, Kobayashi AS. Moire interferometry for dynamic fracture study. *Opt Lasers Eng* 2003; 40: 231-247.

Kolsky H. An investigation of the mechanical properties of materials at very high rates of loading. *Proc Phys Soc London B* 1949; 62: 676–700.

Koohbor B, Mallon S, Kidane A, Sutton MA. A DIC-based study of in-plane mechanical response and fracture of orthotropic carbon fiber reinforced composite. *Compos Part B* 2014; 66: 388–99

Lambros J, Rosakis AJ. Dynamic crack initiation and growth in thick unidirectional graphite/epoxy plates. *Compos Sci Technol* 1997; 57: 55-65.

LeBlanc J, Shukla A, Rousseau C, Bogdanovich A Shock loading of three dimensional woven composite materials. *Compos Struct* 2007; 79: 344–55.

Lee D, Tippur H, Bogert P. Quasi-static and dynamic fracture of graphite/epoxy composites: An optical study of loading-rate effects. *Compos Part B-Eng* 2010; 41B: 462-74.

Lee D, Tippur H, Kirugulige M Experimental study of dynamic crack growth in unidirectional graphite/epoxy composites using digital image correlation method and high-speed photography. *J Compos Mater* 2009; 43: 2081-2108.

Luo PF, Chao YJ, Sutton MA, Peters WH Accurate measurement of three-dimensional deformations in deformable and rigid bodies using computer vision. *Exp Mech* 1993;33: 123-133.

Marsavina, L. Linul, E. Voiconi, T. Sadowski, T. A comparison between dynamic and static fracture toughness of polyurethane foams. *Polymer Testing* 2013; 32: 73-680.

McNeil SR, Peters WH, Sutton MA. Estimation of stress intensity factor by digital image correlation. *Eng Fract Mech* 1987; 28: 101-12.

Meyers M. Dynamic behavior of materials 1<sup>st</sup> ed. Wiley-interscience, New York, 1994. 1-4.

Naik NK, Asmelash A, Kavala VR, Veerraju C. Interlaminar shear properties of polymer matrix composites: strain rate effect. *Mech Mater* 2007; 39: 1043-52.

Nian, W. Subramaniam, K. Andreopoulos, Y. Dynamic compaction of foam under blast loading considering fluid-structure interaction effects, *International J Impact Eng* 2007; 50: 29-39.

Payman, W. Shepherd, WCF. Explosion waves and shock waves. Part VI: The disturbance produced by bursting diaphragms with compressed air., *Proc R Soc A* 1946; 186: 243–321.

Pollock P, Yu L, Sutton MA, Guo S, Majumdar P, Gresil M. Full field measurements for determining orthotropic elastic parameters of woven glass-epoxy composites using off-axis tensile specimens. *Exp Tech* 2012;

Reneer DV, Hisel RD, Hoffman JM, Kryscio RJ, Lusk BT, Geddes JW. A Multi-Mode Shock Tube for Investigation of Blast-Induced Traumatic Brain Injury. *J Neurotraum* 2011; 28: 95-104.

Schardin, H. Bemerkungen zum Druckausgleichsvorgang in einer Rohrleitung. *Phys Zeits* 1932; 4: 33 60.

Shivakumar Gouda PS, Kudar SK, Prabhuswamy S, Jawali D. Fracture toughness of glass-carbon (0/90)s fiber reinforced polymer composite – an experimental and numerical study. *J Min Mater Char Eng* 2011; 10: 671-82.

Shukla A, Agarwal BD, Bhushan B. Determination of stress intensity factor in orthotropic composite materials using strain gages. *Eng Fract Mech* 1989; 32: 469-77.

Sun CT, Han C. A method for testing interlaminar dynamic fracture toughness of polymeric composites. *Compos Part B-Eng* 2004; 35B: 647-55.

Sutton MA, Cheng CS, Zavattieri P, Yan J, Deng X. Three-dimensional digital image correlation to quantify deformation and crack-opening displacement in ductile aluminum under mixed-mode I/III loading. *Opt Eng* 2006; 46: 1-17.

Sutton MA, Mingqi C, Peters WH, Chao YJ, McNeill SR. Application of an optimized digital correlation method to planar deformation analysis. *Image Vision Comput* 1986; 4: 143-50.

Vieille P. Etude sur les roles des discontinuites dans les phenomenes de propagation. *Memoire des Poudres et Saltpetres* 1900; 10: 117–260.

Vieille P. Sur les discontinuites produites par la de'tente brusque de gas comprimes. *Comptes Rendus de l'Academie des Sciences de Paris*, 1899; 129: 1228–30.

Weerasooriya, T. The MTL torsional split-Hopkinson bar. MTL-TR-90-27, U.S. Army Materials Technology Laboratory, Watertown, MA, 1990.

Wosu SN, Hui D, Dutta PK. Dynamic mixed-mode I/II delamination fracture and energy release rate of unidirectional graphite/epoxy composites. *Eng Fract Mech* 2005; 72: 1531-58.

Yanase K, Ju JW. Toughening behavior of unidirectional fiber reinforced composites containing a crack-like flaw: Matrix crack without fiber break. *Int J Damage Mech* 2013; 22: 336-55.

Yates JR, Zanganeh M, Tai YH. Quantifying crack tip displacement fields with DIC. *Eng Fract Mech* 2010; 77: 2063-76.

Yoneyama S, Morimoto Y, Takashi M. Automatic evaluation of mixed-mode stress intensity factors utilizing digital image correlation. *Strain* 2006; 42: 21-9.